



**UNIVERSIDAD DE INVESTIGACIÓN DE  
TECNOLOGÍA EXPERIMENTAL YACHAY**

**Escuela de Ciencias Físicas y Nanotecnología**

**Structural, morphological, and optical characterization of rare  
earth-doped Hydroxyapatite.**

Trabajo de integración curricular presentado como requisito para la  
obtención  
del título de Físico.

**Autor:**

**Vega Zerpa María Fernanda**

**Tutor:**

**Ph.D. González Gema**

## AUTORÍA

Yo, Vega Zerpa María Fernanda, con cédula de identidad 1759966177, declaro que las ideas, juicios, valoraciones, interpretaciones, consultas bibliográficas, definiciones y conceptualizaciones expuestas en el presente trabajo; así cómo, los procedimientos y herramientas utilizadas en la investigación, son de absoluta responsabilidad de el/la autora (a) del trabajo de integración curricular. Así mismo, me acojo a los reglamentos internos de la Universidad de Investigación de Tecnología Experimental Yachay.

Urcuquí, mayo, 2023.

A handwritten signature in blue ink, consisting of stylized initials and a long horizontal stroke extending to the right.

---

María Fernanda Vega Zerpa

CI: 1759966177

## AUTORIZACIÓN DE PUBLICACIÓN

Yo, Vega Zerpa María Fernanda, con cédula de identidad 1759966177, cedo a la Universidad de Investigación de Tecnología Experimental Yachay, los derechos de publicación de la presente obra, sin que deba haber un reconocimiento económico por este concepto. Declaro además que el texto del presente trabajo de titulación no podrá ser cedido a ninguna empresa editorial para su publicación u otros fines, sin contar previamente con la autorización escrita de la Universidad.

Asimismo, autorizo a la Universidad que realice la digitalización y publicación de este trabajo de integración curricular en el repositorio virtual, de conformidad a lo dispuesto en el Art. 144 de la Ley Orgánica de Educación Superior

Urququí, mayo, 2023.

A handwritten signature in blue ink, appearing to be 'M. F. Vega Zerpa', written over a faint circular stamp.

---

María Fernanda Vega Zerpa

CI: 1759966177

## Agradecimientos

Más que una tesis es el fin de un largo camino que he recorrido por ocho años, después de dos universidades y dos países, tengo que agradecerle a demasiadas personas que hicieron esto posible. Mi sueño de convertirme en científica jamás hubiera sido posible si no fuera por todas las personas que me acompañaron durante este camino. Yo solita no hubiera podido, así que es un logro en conjunto, en equipo.

Primero quiero agradecer enormemente a mi familia, gracias a mis padres Sonia y Gerardo por todo el apoyo que me han dado durante mis estudios. Gracias por todas las palabras de aliento que me dieron para que no me rindiera cada vez que quise tirar la toalla. Gracias por confiar en mí y creer en mis sueños.

Gracias a mis abuelos Ovidio y Adelina, por acompañarme en este proceso. Gracias a mi abuela, quien me ayudó con los trámites en Venezuela y, movió cielo y tierra para que pudiera continuar mis estudios en Ecuador. Sin ti, esto no sería posible.

Gracias a mis amigos, la familia que uno escoge. Gracias a mis mejores amigas de bachillerato que me han visto crecer en la vida y en este mundo de la ciencia. Sobre todo gracias a Mila por siempre estar. Gracias a mis amigos de la ULA y Yachay. Con amigos la vida es mas bonita, y ustedes hicieron mi carrera de pregrado mas bonita.

Gracias a mis ilustres universidades, que me formaron y educaron, La Universidad de Los Andes, en Mérida, Venezuela, y la Universidad Yachay Tech, en Urcuquí, Ecuador. Gracias por darme las bases y los conocimientos para hacer ciencias. Siempre llevaré con orgullo y en el corazón el nombre de estas dos universidades, y si la vida me lo permite las representaré por todo lo alto.

Gracias a mis profesores, los padres que te adoptan en la universidad. Gracias al profesor Marcos, por motivarme a estudiar física y enseñarme lo maravilloso que es trabajar desde la ciencia para ayudar a la sociedad. Gracias a mi querido profesor Mario, el profesor que me ha acompañado desde Venezuela hasta Ecuador, que dicha y suerte fue coincidir con usted en dos universidades.

Gracias a mis tutoras de tesis, dos mujeres admirables, que me inspiran a ser una gran científica y persona, dos mujeres que siento como mis madres científicas, Gema y Sarah. Gracias al profesor Luis quién me permitió trabajar y me orientó en el laboratorio de óptica de la PUCE. Siendo esta el área en que me quiero especializar, esta oportunidad ha sido todo un sueño para mí.

Por último, pero no menos importante, gracias a mi querido Andrés. Gracias por acompañarme estos últimos años de carrera. Gracias por todo el apoyo y cariño.

Llegar acá, en un camino que muchas veces me pareció eterno e imposible, llegar acá, tan lejos, fue gracias a todos los que me acompañaron.

*"Si caminas solo irás más rápido, si caminas acompañado llegarás más lejos"*

## Resumen

En los últimos años ha aumentado el interés por el estudio de los materiales luminiscentes para aplicaciones médicas. Sin embargo, estos materiales deben ser no tóxicos para su aplicación. En este sentido, se propone el estudio de la Hidroxiapatita dopada con Europio. La hidroxiapatita,  $\text{Ca}_{10}(\text{PO}_4)_6(\text{OH})_2$ , es un biomineral que se encuentra en nuestros huesos y, presenta propiedades biocompatibles y bioactivas que inducen la osteointegración. Además, la Hidroxiapatita presenta propiedades estructurales que le permiten aceptar más de la mitad de los elementos de la tabla periódica sin romper su simetría cristalina. Considerando esto, se sugiere la incorporación de elementos de tierras raras (europio) en su estructura para incrementar la luminiscencia de la misma.

En el presente trabajo, se propone el dopamiento sustitucional de la hidroxiapatita con europio y, el estudio del efecto de la concentración de europio y el tratamiento térmico sobre las propiedades luminiscentes del material. La caracterización estructural se estudiará mediante microscopía electrónica de barrido (SEM), difracción de rayos X (XRD), espectroscopia infrarroja por transformada de Fourier (FTIR) y espectroscopia Raman. La caracterización óptica se medirá con espectroscopia de luminiscencia. Finalmente, la hidroxiapatita dopada con europio da lugar a un material multifuncional con amplio uso en diversas áreas de la medicina, gracias a sus dos propiedades principales, la biocompatibilidad y la luminiscencia.

**Palabras Clave:** Hidroxiapatita, luminiscencia, nanopartículas, tierras raras, europio.

## Abstract

In recent years, there has been increasing interest in the study of luminescent materials for medical applications. However, these materials must be non-toxic for their application. In this sense, the study of Europium-doped hydroxyapatite is proposed. Hydroxyapatite,  $\text{Ca}_{10}(\text{PO}_4)_6(\text{OH})_2$ , is a biomineral found in our bones and, exhibits biocompatible and bioactive properties that induce osseointegration. In addition, hydroxyapatite presents structural properties that allow it to accept more than half of the elements of the periodic table without breaking its crystalline symmetry. Considering this, the incorporation of rare earth elements (europium) in its structure is suggested to increase its luminescence.

In the present work, it is proposed the substitutional doping of hydroxyapatite with europium and, the study of the effect of europium concentration and heat treatment on the luminescent properties of the material. The structural characterization will be studied by scanning electron microscopy (SEM), X-ray diffraction (XRD), Fourier transform infrared spectroscopy (FTIR) and Raman spectroscopy. Optical characterization will be measured with luminescence spectroscopy. Finally, europium-doped hydroxyapatite results in a multifunctional material with wide use in various areas of medicine, thanks to its two main properties, biocompatibility and luminescence.

**Keywords:** Hydroxyapatite, luminescence, nanoparticles, rare earths, europium.

# Contents

<b>List of Figures</b>	<b>viii</b>
<b>List of Tables</b>	<b>xi</b>
<b>List of Papers</b>	<b>xiv</b>
<b>1 Introduction</b>	<b>1</b>
1.1 General and Specific Objectives . . . . .	1
<b>2 Theoretical Background</b>	<b>3</b>
2.1 Nanomedicine . . . . .	3
2.2 Hydroxyapatite . . . . .	4
2.3 Europium . . . . .	6
2.4 Synthesis methods . . . . .	7
2.4.1 Substitution doping and interstitial doping . . . . .	10
2.4.2 Hydroxyapatite substitutional doping . . . . .	11
2.4.3 Hydroxyapatite substitutional doping with Europium . . . . .	12
2.5 Theory of Luminescence . . . . .	13
2.5.1 Luminescence . . . . .	16
2.5.2 General Characteristics of Luminescence . . . . .	18
2.5.3 Thermoluminisencia . . . . .	21
2.5.4 Effect of temperature on luminescence . . . . .	23
2.5.5 Luminescence materials . . . . .	24
2.5.6 Hydroxyapatite Luminescence Properties . . . . .	25
2.5.7 Europium Luminescence Properties . . . . .	25
2.5.8 Factors influencing luminescence . . . . .	27
2.6 State of the art . . . . .	28
2.6.1 Hydroxyapatite doped Europio systems . . . . .	28
2.7 Experimental Characterization Techniques . . . . .	29

2.7.1	X-ray diffraction . . . . .	29
2.7.2	Fourier-transform infrared spectroscopy . . . . .	32
2.7.3	Scanning Electron Microscopy . . . . .	34
2.7.4	Raman Spectroscopy . . . . .	36
<b>3</b>	<b>Methodology</b>	<b>41</b>
3.0.1	Chemicals . . . . .	41
3.0.2	Synthesis . . . . .	41
3.0.3	Characterization Equipment . . . . .	43
<b>4</b>	<b>Results &amp; Discussion</b>	<b>47</b>
4.1	Morphological and Structural Characterization . . . . .	47
4.1.1	Fourier-transform infrared spectroscopy . . . . .	47
4.1.2	Scanning Electron Microscopy and EDX microanalysis . . . . .	55
4.1.3	X-ray Diffraction . . . . .	57
4.1.4	Raman Spectroscopy . . . . .	60
4.1.5	Luminescence Spectroscopy . . . . .	68
<b>5</b>	<b>Conclusions &amp; Outlook</b>	<b>77</b>
	<b>Bibliography</b>	<b>81</b>

# List of Figures

2.1	Crystal structure of Hydroxyapatite. <sup>1</sup>	5
2.2	A schematic of substitutional and interstitial doping for a host metal lattice (green). (a) Substitutional doping by foreign atoms (blue). (b) Interstitial doping by foreign atoms (brown). <sup>2</sup>	10
2.3	Schematic showing the structure of the three different forms of anatase with possible nitrogen positions. <sup>3</sup>	11
2.4	Schematic view projected in the [001] direction of the hydroxyapatite structure. <sup>4</sup>	12
2.5	Bioluminescent bays in Puerto Rico <sup>5</sup>	13
2.6	Fireflies. <sup>6</sup>	14
2.7	Fluorite Mineral. <sup>7</sup>	14
2.8	Jablonski diagram illustrating the fundamental processes of fluorescence and phosphorescence. <sup>8</sup>	15
2.9	Valence and Conduction band <sup>9</sup>	16
2.10	Classification of luminescence according to duration time <sup>10</sup>	17
2.11	Diagram of energy levels of the luminescent ion A. The * indicates the excited state, R the radiative return, and NR the non-radiative return to the ground state <sup>11</sup>	19
2.12	Photophysical processes in molecular systems explained by Jablonski diagram <sup>12</sup>	19
2.13	Electron band structure of a semiconductor mineral, showing the processes of excitation (energy absorption), non-radiative energy transfer, and luminescence generation <sup>13</sup>	20
2.14	BraËunlich (1979) diagram of the filling functions for a uniform distribution of traps before and after perturbation by an external stimulus and during thermally stimulated relaxation. <sup>14</sup>	22
2.15	Localized and delocalized states in semiconductors <sup>15</sup>	23
2.16	TL spectra of albite, a sodium feldspar <sup>10</sup>	24
2.17	Energy levels scheme of Eu <sup>3+</sup> <sup>16</sup>	26
2.18	Geometric derivation of Bragg's law: constructive interference occurs when the lattice delay between waves scattered from adjacent lattice planes, given by $a_1 + a_2$ , is an integer multiple of the wavelength $\lambda$ . <sup>17</sup>	30
2.19	Schematic diagram of a diffractometer system <sup>18</sup>	31
2.20	The XRD patterns of HAp and Eu:Hap synthesized with $0 \leq x \leq 0.2$ <sup>19</sup>	32
2.21	Schematic diagram of Michelson interferometer. <sup>20</sup>	33

2.22	Transmittance infrared spectra of HA:Eu samples synthesized with Eu/(Ca+Eu) = 1%, 2%, 10% and 20% <sup>19</sup> . . . . .	34
2.23	Illustration of several signals generated by the electron beam–specimen interaction in the scanning electron microscope and the regions from which the signals can be detected. <sup>21</sup> . . . . .	36
2.24	Scanning Electron Microscope Diagram. <sup>22</sup> . . . . .	37
2.25	Idealised model of Rayleigh scattering and Stokes and anti-Stokes Raman scattering. <sup>23</sup> . . . . .	38
2.26	Eu-doped Hydroxyapatite Raman spectra (A) co-precipitation, (B) hydrothermal method. <sup>24</sup> . . . . .	39
3.1	a) Synthesis of europium-doped hydroxyapatite. b) Hydroxyapatite synthesis for different europium concentrations, P=20%-Eu, P <sub>1</sub> =15%-Eu and P <sub>2</sub> =10%-Eu. c) Resulting solution mounted in a reactor at 125°C for 24 hours to produce hydroxyapatite. . . . .	42
3.2	HA:xEu tablets for x=0%, 5%, 10%, 15%, and 20%, calcined at 800 °C under a UV lamp (365 nm). . . . .	43
3.3	An X-ray diffractometer Rigaku, MiniFlex. . . . .	44
3.4	Fourier-transform infrared spectrometer Agilent Cary 630 FTIR. . . . .	44
3.5	Phenom ProX Desktop Scanning Electron Microscope. . . . .	45
3.6	LabRAM HR Evolution Raman microscopes from HORIBA France SAS. . . . .	45
3.7	Optical path produced to study the photoluminescence of the samples with a 405 nm incident laser, for this purpose photoluminescence spectroscopy was employed using an emission monochromator (MicroHR, Horiba) coupled to a solid state detector (Si/InGaAs, Horiba). . . . .	46
4.1	FTIR spectrum for Ha:xEu at ambient temperature, for x=0%, 5%, 10%, 15%, and 20% . . . . .	48
4.2	FTIR spectrum for Ha:xEu at 200 °C, for x=0%, 5%, 10%, 15%, and 20% . . . . .	49
4.3	FTIR spectrum for Ha:xEu at 450 °C, for x=0%, 5%, 10%, 15%, and 20% . . . . .	51
4.4	FTIR spectrum for Ha:xEu at 600 °C, for x=0%, 5%, 10%, 15%, and 20% . . . . .	52
4.5	FTIR spectrum for Ha:xEu at 800 °C, for x=0%, 5%, 10%, 15%, and 20%. . . . .	54
4.6	SEM micrographs. a) BSE image of HA:5%Eu, b) BSE images of HA:20%Eu. . . . .	56
4.7	SEM micrographs. a) EDX spectrum of HA:5%Eu, b) EDX spectrum of HA:20%Eu, c) Atomic percentage of HA:5%Eu, d) Atomic percentage of HA:20%Eu. . . . .	56
4.8	XRD Spectrum for Ha:xEu at ambient temperature, for x= 5%, 10%, 15%, and 20%. . . . .	57
4.9	XRD Spectrum for Ha:xEu at 200 °C, for x= 5%, 10%, 15% and 20%. . . . .	58
4.10	XRD Spectrum for Ha:xEu at 450 °C, for x= 5%, 10%, 15% and 20%. . . . .	59
4.11	XRD Spectrum for Ha:xEu at 600 °C, for x= 5%, 10%, 15% and 20%. . . . .	60
4.12	XRD Spectrum for Ha:xEu at 800 °C, for x= 5%, 10%, 15% and 20%. . . . .	61
4.13	Raman spectrum for Ha:xEu at ambient temperature, for x= 5%, 10%, 15%, and 20%. . . . .	63
4.14	Raman spectrum for Ha:xEu at 200 °C, for x= 5%, 10%, 15% and 20%. . . . .	64
4.15	Raman spectrum for Ha:xEu at 450 °C, for x= 5%, 10%, 15% and 20%. . . . .	65
4.16	Raman spectrum for Ha:xEu at 600 °C, for x= 5%, 10%, 15% and 20%. . . . .	66
4.17	Raman spectrum for Ha:xEu at 800 °C, for x= 5%, 10%, 15% and 20%. . . . .	67
4.18	Photoluminescence spectra for Ha:xEu at room temperature, for x= 5%, 10%, 15%, and 20%. . . . .	69

4.19	Photoluminescence spectrum for Ha:xEu at 200 °C, for x= 5%, 10%, 15%, and 20%. . . . .	70
4.20	Photoluminescence spectrum for Ha:xEu at 450 °C, for x= 5%, 10%, 15%, and 20%. . . . .	72
4.21	Photoluminescence spectrum for Ha:xEu at 600 °C, for x= 5%, 10%, 15%, and 20%. . . . .	73
4.22	Photoluminescence spectrum for Ha:xEu at 800 °C, for x= 5%, 10%, 15%, and 20%. . . . .	75



# List of Tables

2.1	HA's lattice parameters of various Apatite Samples. <sup>25</sup> . . . . .	5
2.2	Classification of luminescence depending on the source of excitation <sup>26</sup> . . . . .	18
3.1	Reagent quantities used for the hydrothermal synthesis of HA:xEu for x=0%, 5%, 10%, 15%, and 20%. . . . .	43
4.1	Measured absorption features in the FTIR spectra and relative assignments for HA:xEu at Ambient Temperature, for x= 0%, 5%, 10%, 15%, and 20%. . . . .	48
4.2	Measured absorption features in the FTIR spectra and relative assignments for HA:xEu at 200 °C, for x=0%, 5%, 10%, 15%, and 20% . . . . .	50
4.3	Measured absorption features in the FTIR spectra and relative assignments for HA:xEu at 450 °C, for x=0%, 5%, 10%, 15%, and 20%. . . . .	51
4.4	Measured absorption features in the FTIR spectra and relative assignments for HA:xEu at 600 °C, for x=0%, 5%, 10%, 15%, and 20%. . . . .	53
4.5	Measured absorption features in the FTIR spectra and relative assignments for HA:xEu at 800 °C, for x=0%, 5%, 10%, 15%, and 20%. . . . .	54
4.6	Phase analysis using experimentally obtained powder diffraction data compared to the Open Crystallography Database (COD) for HA:xEu with x=0%, 5%, 10%, 15%, and 20%, for all temperatures. <sup>27, 28, 29, 30, 31, 32, 33, 34</sup> . . . . .	62
4.7	Assignment of Raman peaks of HA:xEu at Ambient Temperature, for x= 5%, 10%, 15%, and 20%. . . . .	64
4.8	Assignment of Raman peaks of HA:xEu at 200 °C, for x= 5%, 10%, 15%, and 20%. . . . .	65
4.9	Assignment of Raman peaks of HA:xEu at 450 °C, for x= 5%, 10%, 15%, and 20%. . . . .	66
4.10	Assignment of Raman peaks of HA:xEu at 600 °C, for x= 5%, 10%, 15%, and 20%. . . . .	67
4.11	Assignment of Raman peaks of HA:xEu at 800 °C, for x= 5%, 10%, 15%, and 20%. . . . .	68
4.12	Photoluminescence peak intensities for specific wavelengths of HA:xEu at ambient temperature, for x= 5%, 10%, 15%, and 20%. . . . .	68
4.13	Photoluminescence peak intensities for specific wavelengths of HA:xEu at 200 °C, for x= 5%, 10%, 15%, and 20%. . . . .	71

4.14	Photoluminescence peak intensities for specific wavelengths of HA:xEu at 450 °C, for x= 5%, 10%, 15%, and 20%. . . . .	72
4.15	Photoluminescence peak intensities for specific wavelengths of HA:xEu at 600 °C, for x= 5%, 10%, 15%, and 20%. . . . .	74
4.16	Photoluminescence peak intensities for specific wavelengths of HA:xEu at 800 °C, for x= 5%, 10%, 15%, and 20%. . . . .	75

# Chapter 1

## Introduction

Hydroxyapatite is a biomineral nanostructure found in human hard tissues<sup>35</sup>, which exhibits excellent physicochemical and mechanical properties such as biocompatibility, bioaffinity, bioactivity, osteoconduction, osseointegration, osteoinduction, osteoinduction<sup>36</sup>, non-toxicity, non-inflammation<sup>35</sup>, high-temperature processability, low dielectric breakdown strength<sup>37</sup>, luminescence, fluorescence, magnetism<sup>38</sup>, and among others. To improve the luminescent properties of hydroxyapatite, it is proposed to substitute calcium atoms with europium. This is because europium has a simple electronic energy level scheme, hypersensitive transitions, and an ionic radius similar to that of calcium, being the apatite lattice a good host for europium doping. Moreover, this doping presents low toxicity<sup>39,40</sup> and a stable luminescence in time<sup>41</sup>. Some of the applications and investigations found with europium doped hydroxyapatite include potentially biocompatible fluorescent labeling material<sup>42</sup>, drug release and targeting<sup>19</sup>, disease therapy<sup>43</sup>, antimicrobial activity testing<sup>41</sup>, bioimaging, magnetic resonance imaging, bimodal imaging, cellular imaging<sup>38</sup> and many more found so far. This nanomaterial strongly impacts nanomedicine since the combination of biocompatibility and light emission is of great interest in this area<sup>24</sup>. The substitution of the calcium atoms in the hydroxyapatite structure with europium represents a greater increase in the luminescent properties of the nanomaterial than that achieved by doping, thus proposing a significant improvement in the nanomaterial for future applications in nanomedicine.

### 1.1 General and Specific Objectives

Study the structure and optical properties of hydroxyapatite substitution doping with europium.

- Synthesize hydroxyapatite by hydrothermal method.
- Substitute calcium atoms in the hydroxyapatite structure with europium.
- Characterize the samples by X-Ray Diffraction, Fourier-transform infrared spectroscopy, Raman spectroscopy, and Scanning Electron Microscopy.
- Study the luminescence properties of europium-substituted hydroxyapatite structure.

- Analyze the effect of the thermal treatment on the luminescent properties of europium-substituted hydroxyapatite.

## Chapter 2

# Theoretical Background

### 2.1 Nanomedicine

From the need to address many diseases that have their origin in alterations of biological processes at the molecular or nano-scale level, nanomedicine was born. Nanomedicine is a field of nanotechnology that uses the physical properties and characteristics of nanomaterials for the diagnosis and treatment of diseases at the molecular level<sup>44</sup>. Nanotechnology and nanoscience application to the prevention and treatment of human disease has grown significantly since its conception in the 1990s<sup>45</sup>. Nanotechnology is defined as the "intentional design, characterization, production, and applications of materials, structures, devices, and systems by controlling their size and shape in the nanoscale range (from 1 to 100 nm)". Accordingly, because nanomaterials have similar scales to molecules and biological systems, these are potentially useful for medical applications<sup>44</sup>.

As a consequence of the excellent properties of nanoparticles (NPs), high stability, high payload, multifunctionality, design flexibility, and delivery efficiency to target tissues, NPs have been used in nanomedicine in some applications, such as multimodal imaging, drug delivery, and targeted therapy for human diseases<sup>46</sup>. Nanomaterials are commonly composed of metal atoms, non-metal atoms, or a mixture of metal and non-metal atoms, often called metal, organic or semiconducting particles, respectively. Nanomaterial surfaces are frequently coated with polymers or biorecognition molecules to improve biological molecules' biocompatibility and selective targeting<sup>44</sup>. Finally, it is essential to emphasize the great interest that there is in nanomedicine for nanomaterials that present biocompatibility and light emission at the same time since these properties play an important role in applications such as potential biocompatible fluorescent labeling material<sup>42</sup>, drug release and targeting<sup>19</sup>, disease therapy<sup>43</sup>, antimicrobial activity testing<sup>41</sup>, bioimaging, magnetic resonance imaging, bimodal imaging, cellular imaging<sup>38</sup> and many more.

## 2.2 Hydroxyapatite

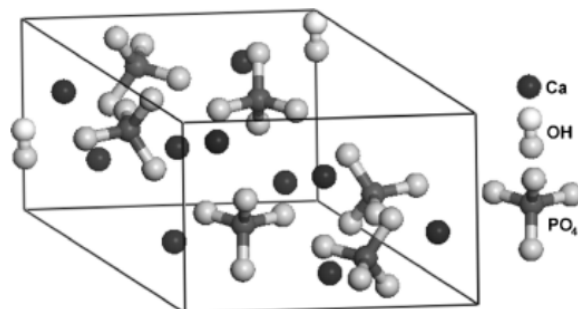
Nowadays, advances in science have made it possible to generate applications in biomaterials and optics from nanostructures. Such is the case of hydroxyapatite (HA), a biomineral nanostructure found in human hard tissues<sup>35</sup>. Living tissue, such as Bone, is composed of 20-30 wt% in the organic phase, 60-70 wt% inorganic phase, and approximately 5 wt% of water. The organic phase is composed of collagen and other compounds in small concentrations and gives elasticity, flexibility, and resistance to the bone. The inorganic phase is composed of hydroxyapatite and ions of magnesium, fluoride, and sodium in small concentrations and gives hardness and stiffness to the bone<sup>37</sup>. Hydroxyapatite has a wide variety of applications thanks to its excellent properties, such as biocompatibility, bioactivity, osteoconductivity, non-toxicity, and non-inflammatory nature<sup>35</sup>.

Hydroxyapatite containing only calcium and phosphate ions has so far reported no adverse local or systemic toxicity. This is the main reason for its favorable biological properties such as biocompatibility, bioaffinity, bioactivity, osteoconduction, osseointegration, and osteoinduction (under certain conditions)<sup>36</sup>. In addition, Hydroxyapatite presents physicochemical properties such as the high adsorb capability for biomacromolecules and high dielectric properties. Nevertheless, the mechanical properties of HA present brittleness, low elasticity, high-temperature processability, and low dielectric breakdown strength<sup>37</sup>. For that reason, HA presents lower fracture toughness<sup>47</sup>.

Due to the wide variety of physicochemical properties of hydroxyapatite, there are a large number of applications. The use of hydroxyapatite in the bone environment has been studied for more than 20 years, presenting a well-established osteoconductive behavior<sup>48</sup>. For that reason, hydroxyapatite is used in prosthetic applications, such as Bone tissue engineering, restoration of periodontal defects, edentulous ridge augmentation, orthopedic and dental implant coating, endodontic treatment like pulp-capping, repair of mechanical, bifurcation perforations and apical barrier formation, fillers for reinforcing restorative glass ionomer cement (GIC) and restorative composite resin, etc.<sup>35</sup>

HA nanoparticles (NPs) as host materials can be subsequently functionalized with various dopants and substrates. HA NPs with luminescence dopants can be suitable for biomedical applications, such as cell imaging, making it possible to non-invasively and quantitatively visualize the molecular processes occurring at the cellular and sub-cellular levels. HA-based nanoprobe can be divided into three classes according to their functional properties: Luminescent HA NPs, such as fluorescent NPs used in bioimaging; Magnetic HA NPs, used in magnetic resonance imaging (MRI); and Luminomagnetic HA NPs, used in bimodal imaging, drug delivery, and cellular imaging (including targeted imaging) applications of HA-based nanoprobe<sup>38</sup>.

Hydroxyapatite is composed of calcium and phosphorus in a ratio (Ca/P) of 1.67; its stoichiometric formula is  $Ca_{10}(PO_4)_6(OH)_2$ <sup>35</sup>. A network of phosphate groups gives the structure and stability of HA. As shown in Figure 1, the crystal structure of Hydroxyapatite is formed by two types of anions and one type of cation. The anions are phosphate ( $PO_4^{3-}$ ) and monovalent hydroxyl ( $OH^-$ ), and the cations are calcium ( $Ca^{2+}$ )<sup>1</sup>.

Figure 2.1: Crystal structure of Hydroxyapatite.<sup>1</sup>

Hydroxyapatite has a hexagonal crystal structure (Figure 2.1) with rotation by a 6-fold axis and the translation  $3/6$  perpendicular to a mirror in the  $c$ -axis. In addition, it possesses an  $a$ -axis with angles of  $120^\circ$  to each other. Thus being its space group  $P6_3/m$ <sup>1</sup>. The network parameters vary according to the synthesis path and the initial source, so according to the materials and synthesis of HA, the lattice parameters obtained are as follows:

Materials	a (Å)	c (Å)	Synthesis
Precipitated HA (PHA)	9.419	6.890	Wet Chemical Method
Coralline HA (CHA)	9.420	6.905	Prepared from natural coral exoskeleton
Bovine HA (BHA)	9.426	6.894	Prepared from xenogeneic bone
HA	9.418	6.884	Standard measurement from JCPDS

Table 2.1: HA's lattice parameters of various Apatite Samples.<sup>25</sup>

Taking the average of the above values in the table 2.1, the lattice constants of the HA are  $a = 9.420 \text{ \AA}$  and  $c = 6.893 \text{ \AA}$ .

Natural and synthetic sources can produce HA, and depending on the source synthetic or biological HA can be obtained. Synthetic HA and natural bone do not have the same mineral traces due to synthetic HA having a stoichiometric arrangement of its components. On the other hand, bio-HA from natural sources such as coral and bovine bone are more similar to human bone tissues. As a consequence of the different sources, there are different production methods for both HA types<sup>37</sup>, such as:

- Synthetic HA: Different parameters, such as properties and characteristics, are essential to the synthesis methodology of HA. Characteristics such as particle size, shape, orientation and distribution, phase purity agglomeration, stoichiometry, uniformity, degree of crystallinity, and surface area<sup>47,36</sup>. In addition, the quality

of the HA is crucial because it determines the material's physical and mechanical properties and bioactivity<sup>47</sup>. Therefore, various methodologies are used to prepare HA with different morphologies:

Sol-gel, co-precipitation, wet-chemical synthesis, hydrothermal synthesis, mechano-chemical synthesis, mechanical alloying, ball milling, radio frequency induction plasma, Vibro-milling of bones, liquid-solid synthesis, electrocrystallization, solvothermal, hydrolysis of calcium orthophosphates, laser-induced fragmentation of HA micro-particles in water, the electrospinning technique and radiofrequency magnetron sputtering<sup>36</sup>.

- Natural HA: In this case, to obtain natural HA is important to remove the organic material due to avoid infections, disease transfer, and immunological defensive reactions. For this reason, calcination, chemical, and thermal treatments are used<sup>37</sup>.

## 2.3 Europium

Europium is a metal element that belongs to rare earth. This element is present in Earth's crust and has its 50th place in abundance. In addition, this lanthanide can be found in minerals such as monazite, xenotime, and bastnasite in two stable isotopic forms, Eu 153 (52%) and Eu 151 (48%). Moreover, starting nuclear fission of uranium and plutonium, it is possible to obtain other isotopic forms of europium such as Eu 150, Eu 152, Eu 154, and Eu 155<sup>49</sup>. This lanthanide with the atomic number 63, europium, is considered one of the most interesting due to its compounds having a lot of significant properties and applications, in particular in the +3 oxidation state<sup>50</sup>. The study of Europium started in 1885 when Sir William Crookes found an unusual red line in the emission spectrum with a wavelength of 609 nm in a samarium sample. Then, Paul-Émile LeCoq between 1892 and 1893, certified this red line and found a new wavelength of 535 nm (green band). Finally, in 1896, a new lanthanide element between samarium and gadolinium was detected by the french chemist, specialist in spectroscopy studies, Eugène-Anatole Demarçay<sup>51</sup>. In 1907, Demarçay obtained europium with a high purity grade<sup>49</sup>.

In recent years, europium has been studied due to its excellent photoluminescence, electroluminescence, and triboluminescence properties. These properties are caused by a huge facility that has the europium to oxidase to the states II and III in normal atmospheric conditions, the emission of light in these two oxidate states is one the purest to obtain blue for  $\text{Eu}^{2+}$  and red for  $\text{Eu}^{3+}$ . This is the reason why this metal is considered chemically unstable and is normally used in its most stable oxidation states ( $\text{Eu}^{2+}$  and  $\text{Eu}^{3+}$ )<sup>49</sup>. As a consequence of the unstable properties of the Eu, this is the earth rare and less common to use. Still, there are several applications in different fields, such as optical fibers, chromium detection in the environment, photo storage, absorption of neutrons from fission in nuclear reactors, inorganic and laser diodes, detection of toxic chemicals, as markers in medicine, organic light-emitting diodes, p-type semiconductors, clusters metallic, poly-metallic complexes, luminescent additive, light-emitting diodes (LED's), etc.<sup>49</sup>

## 2.4 Synthesis methods

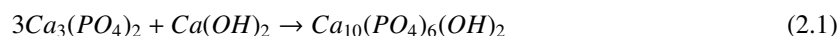
As mentioned before, there are many different methods to obtain HA, but some of the most common methods for the synthesis of Hydroxyapatite are,

- **Precipitation method**

Chemical precipitation is the conversion process of a solution into a solid by converting the substance into an insoluble form or by making the solution supersaturated. It implies the addition of chemical reagents and the separation of the precipitates from the solution.<sup>52</sup>

This method of synthesis is one of the most common due to this method can produce nano HA particles with water as the only sub-product. However, this method presents complications in obtaining stoichiometric HA since it needs high pH and high sintering temperature to produce the ideal crystalline HA. In addition, the HA produced presents high reaction conditions of pH, stirring rate, drying temperature, etc.<sup>47</sup>

For the production of HA by precipitation, the method can be used Ammonium hydroxide, di-ammonium hydrogen phosphate, and calcium nitrate but orthophosphoric acid and calcium hydroxide diluted to pH 9 are normally used<sup>47</sup>, illustrated by the following equation 2.1,



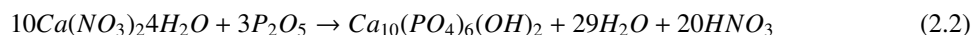
The procedure of this method consists of drop by drop under continuous agitation, with temperatures varying between 25°C and 90°C. To obtain higher crystallinity, it is necessary to have a high reaction temperature<sup>47</sup>.

- **Sol-gel Synthesis**

This method is derived from two words: sol and gel. The term sol refers to the stable suspension of colloidal solid particles in a liquid, where only Van Der Waal forces exist. On the other hand, the term gel describes that the concentration of the solid is higher than that of the liquid. It refers to a semi-rigid mass in which the particles or ions remaining after evaporation begins to form a continuous network. In most gel systems, covalent interactions exist. Finally, the combination of both network functions gives rise to the sol-gel method. In this method, two main reactions are present, which are hydrolysis and condensation.<sup>52</sup>

This synthesis method produces Nano-HA particles with a homogeneous molecular mixture and high control over phase purity<sup>47</sup> because the starting reagents contain minimal impurities<sup>53</sup>. In addition, this process requires a low temperature. At the same time, Sol-gel synthesis needs expensive chemicals and presents the challenge of hydrolyzing phosphate<sup>47</sup>. Proper choice of precursors is important, as HA synthesis by this method can require high temperatures ( 1000°C) if not properly chosen. This makes the sol-gel technique

difficult to apply in obtaining some types of coatings. The sol is prepared by refluxing solutions of  $P_2O_5$  and  $Ca(NO_3)_2 \cdot 4H_2O$  in ethanol<sup>53</sup> (equation 2.2),

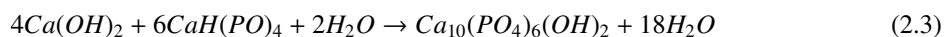


The sol-gel method allows the precursors to pre-react due to the reactivity of the phosphorus species in ethanol solution. The drying temperature is about 150°C, and the heat treatments are carried out in an air atmosphere at 500°C. Moreover, the presence of nitrate groups can ensure the almost complete decomposition of the organic residues of the precursor at 500°C by oxidation. Finally, the decomposition also contributes to the formation of the carbonate-hydroxyapatite phase.<sup>53</sup>

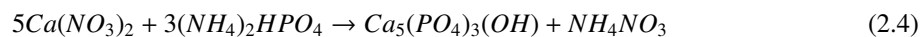
- **Hydrothermal method**

The hydrothermal method is a process that allows the dilution of components that are not usually soluble under normal conditions, producing nanoparticles under the influence of high temperatures and pressures. In addition, it allows controlling the physical and chemical properties of the resulting nanoparticles. These properties depend on the pH, temperature, and pressure of the medium, producing nanoparticles of high yield and purity. It also permits the creation of high-quality crystals and controls their growth.<sup>52</sup>

The major advantage of the hydrothermal process is that it has the presence of an aqueous phase in the system, with water being an active participant in the reaction by accelerating the rate of dissolution, diffusion, adsorption, reaction, and crystallization (nucleation and growth)<sup>53</sup>. The hydrothermal method produces nano-HA with high crystallinity and homogeneity. However, this process can produce agglomeration of HA powders and needs high pressures. To produce HA particles, calcium and phosphate solutions are usually used at very high temperatures and pressures in hydrothermal reactions (equation 2.3). Therefore, to obtain HA crystals (usual agglomerates), it is necessary for the reaction to have been between 60°-205°C for 24 hours<sup>47</sup>.



On the other hand, hydrothermal synthesis is useful for obtaining HA coatings. The reactants for HA formation can be  $Ca(NO_3)_2$  and  $(NH_4)_2HPO_4$  (equation 2.4). In this method, temperatures of 350-400°C are used for 4-10 hours in the presence of water at pH 7.3, and the use of an autoclave is necessary since the filling volume of the autoclave controls the pressure.<sup>53</sup>



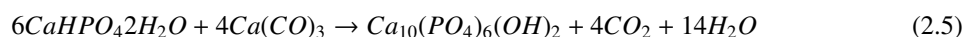
As can be seen, this method has several alternatives of reactants to obtain HA. In addition to the two alternatives mentioned above, other reactions are followed to obtain HA by the hydrothermal method; these are based on  $CaCO_3$  and other phosphates such as  $CaHPO_4$  and  $(NH_4)_2HPO_4$ . As an alternative to these reagents,  $(CH_3COO)_2Ca$  and  $K_2HPO_4$  (in aqueous medium) or  $Ca(OH)_2$  and  $Ca(H_2PO_4)_2-H_2O$  (in alcoholic medium) can be used.<sup>53</sup>

- **Solid-State method**

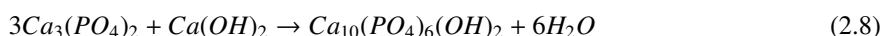
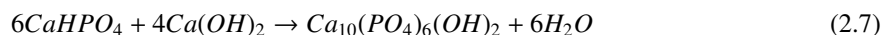
The solid-state reaction route consists of chemical decomposition reactions, where a mixture of solid reactants is heated to produce a new solid composition and gases. Usually, this method is used for the production of complex oxides from simple oxides, carbonates, nitrates, hydroxides, oxalates, alkoxides, and other metal salts. The procedure typically involves several different steps of annealing with multiple intermediate milling steps to increase the homogeneity of the mixture and decrease the particle size of the powder.<sup>54</sup>

Solid-state reactions require high temperatures for two reasons: first, due to the high activation energy needed, and second, to prepare the reagents in fine powder form so that there is intimate contact between them. For the synthesis of HA, powders containing  $Ca^{2+}$  and  $PO_4^{3-}$  ions are used, which will be converted into dense polycrystalline bodies by heat treatment.<sup>53</sup>

The initial reagents for the synthesis of the HA stoichiometric are  $CaCO_3$  and  $CaHPO_4 \cdot 2H_2O$  or its anhydrous form  $CaHPO_4$  according to the following reactions<sup>53</sup>:



Other authors propose other syntheses consisting in the use of  $Ca(OH)_2$  instead of  $CaCO_3$ , as in the following reactions<sup>53</sup>:



In this method, Beta tricalcium phosphate ( $\beta$ -TPC) and  $Ca(OH)_2$  powders are usually combined in ratios (3:0-3.4). The dry powders are mixed in water, and the mixture is wet-milled, melted into bodies, dried, and sintered (equation 2.9).



In addition, the mechanochemical method is also considered a solid-state reaction for nano-HA production. The route of synthesis implies dry powders of calcium hydroxide ( $Ca(OH)_2$ ) and di-ammonium hydrogen phosphate ( $(NH_4)_2HPO_4$ ) mixed, which are subsequently milled dry at several rotational speeds and ball-to-powder ratios.<sup>47</sup>

### 2.4.1 Substitution doping and interstitial doping

An important interest in materials that have different properties and can be used in multiple applications is growing. To modify the properties of materials, a process called doping is used. Doping consists of introducing atomic impurities into a host material. These impurities can alter the material or introduce electronic, magnetic, luminescent, and catalytic properties, for example, in semiconductors.<sup>55</sup>

This doping can be classified into substitutional doping and interstitial doping. According to Chen et al., substitutional doping involves replacing the host metal atoms with foreign ones (Fig. 2.2a). However, when the foreign atoms, usually light elements, occupy interstitial sites, it is known as interstitial doping (Fig. 2.2b).<sup>2</sup>

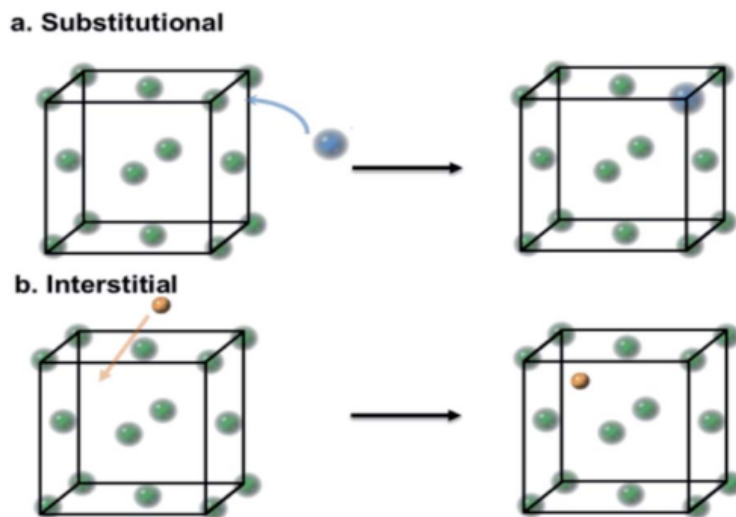


Figure 2.2: A schematic of substitutional and interstitial doping for a host metal lattice (green). (a) Substitutional doping by foreign atoms (blue). (b) Interstitial doping by foreign atoms (brown).<sup>2</sup>

In the same way, Dunnill and Parkin propose that incorporating nitrogen into the  $TiO_2$  structure can occur in a

substitutional and interstitial manner. Furthermore, they report that the name of the doping refers to the location of the nitrogen, which is critical for photocatalytic efficiency. Substitutional doping involves the substitution of oxygen, i.e., the formation of  $\text{TiO}_{2-x}\text{N}_x$ , while interstitial doping involves the addition of nitrogen to the  $\text{TiO}_2$  lattice and the formation of  $\text{TiO}_2\text{N}_x$ , as shown in figure (2.3).<sup>3</sup> Finally, considering these differences, this work proposes substitutional doping of europium in hydroxyapatite.

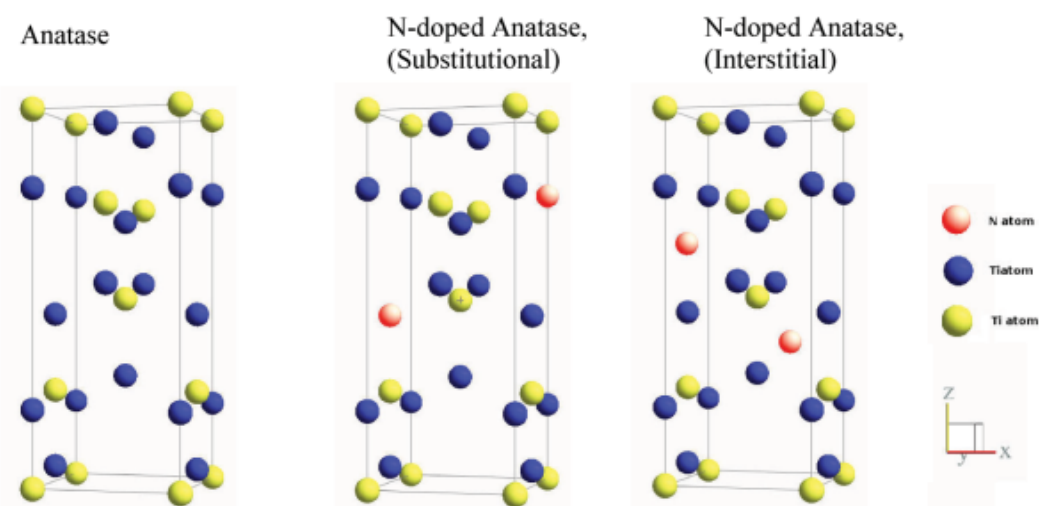


Figure 2.3: Schematic showing the structure of the three different forms of anatase with possible nitrogen positions.<sup>3</sup>

## 2.4.2 Hydroxyapatite substitutional doping

As mentioned above, hydroxyapatite has many interesting properties. However, the functionality of hydroxyapatite can be improved and enhanced if it is doped. The doping of hydroxyapatite is due to the substitution of some of its anions and/or cations by new ions. HA has two types of calcium cations, Ca (I), which are found forming a ring located at the edges of the hexagonal unit cell, and Ca (II), which form equilateral triangles with the column of hydroxyl ions<sup>56</sup> (Figure 2.4).

If some ions are substituted, the hydroxyapatite resulting will present modifications in the lattice parameters and its crystallinity. Thanks to the similarity of charge and size, some ions of the hydroxyapatite can be substituted, for example, hydroxyl ions can be replaced by chloride and fluoride ions, and various ions can replace calcium cations, some of them can be Magnesium ( $\text{Mg}^{2+}$ ), Manganese ( $\text{Mn}^{2+}$ ), Zinc ( $\text{Zn}^{2+}$ )<sup>56</sup>, Europium ( $\text{Eu}^{2+}$  and  $\text{Eu}^{3+}$ ), and many more.

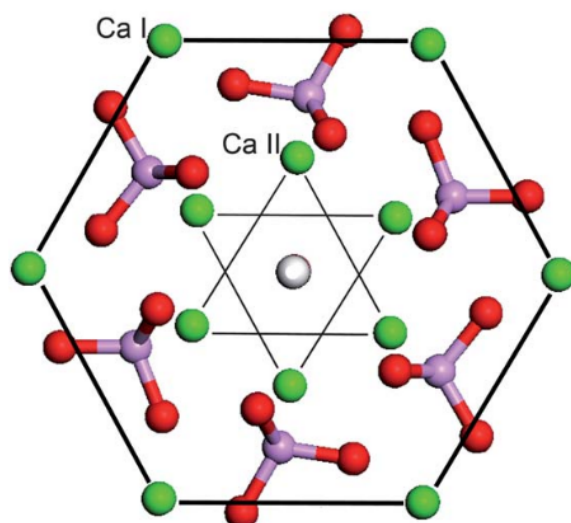


Figure 2.4: Schematic view projected in the [001] direction of the hydroxyapatite structure.<sup>4</sup>

### 2.4.3 Hydroxyapatite substitutional doping with Europium

Nanoparticles in medical applications require a specific size, shape, composition, surface chemistry, and other physicochemical properties. This is because particle geometry influences cell-material interactions, affecting cellular uptake and function. For imaging of tissues or intracellular structures, the use of optical bio labels is suggested. These optical bio labels can be made of various luminescent nanomaterials, such as quantum dots, nanostructures functionalized with organic dyes, and rare-earth-based phosphors<sup>39</sup>. This emerging class of fluorescent label materials is known for its narrow emission bandwidths, high photochemical stability, and long fluorescence lifetimes<sup>42</sup>.

Rare-earth-based nanophosphors have significant advantages over other luminescent materials due to their lower toxicity, photostability, high thermal and chemical stability, high luminescence quantum yield, and sharp emission bands. Typically, these nanophosphors consist of a host matrix, such as fluorides, phosphates, and vanadates, doped with luminescent lanthanide cations. Among the phosphates, calcium hydroxyapatite is particularly interesting for its excellent biological properties<sup>39</sup>. Among the excellent biological properties of lanthanide-doped apatite, nanoparticles are their good biocompatibility and extensive substitutions of cations such as Pr, Tb, and Eu<sup>42</sup>.

Fluorescent labeling is important since nondestructive observations can be made "in vivo" and "in vitro" by substituting calcium ions in the hydroxyapatite crystal lattice with luminescent rare-earth ions. The luminescence intensity of rare-earth ion-doped hydroxyapatite depends on the concentration of rare-earth ions and the crystallinity degree and crystalline structure of the host material. Hydroxyapatite hexagonal permits substituting many rare-earth ions without modification of the crystalline structure. Currently, rare earth ion-doped hydroxyapatite nanoparticles

are under very intensive study as cell labeling materials because of their strong luminescence in the visible light spectrum<sup>41</sup>.

Considering that  $\text{Eu}^{2+}$  is chemically unstable because it is extremely easy to oxidize to  $\text{Eu}^{3+}$  under normal atmospheric conditions, it is usual to work with its most stable oxidation state, i.e.  $\text{Eu}^{3+}$ .<sup>49</sup> Doping hydroxyapatite with trivalent europium ions ( $\text{Eu}^{3+}$ ) has great advantages in that valence state europium has a simple electronic energy level scheme and hypersensitive transitions. On the one hand, such doping has low toxicity and stable luminescence over time. In addition, at low amounts of europium, the bioactivity behavior has no detrimental effects, thus being an excellent candidate for biological probes. On the other hand,  $\text{Ca}^{2+}$  and  $\text{Eu}^{3+}$  have a similar ionic radius, being the apatite lattice a good host for  $\text{Eu}^{3+}$  doping.<sup>41</sup>

## 2.5 Theory of Luminescence

Throughout history, it has been possible to study and reproduce many physical phenomena found in nature. Such is the case of the phenomenon of cold light, which is a natural emission of light at room temperature, known as luminescence.<sup>26</sup> This phenomenon is present in some animals, such as in the lantern fish, jellyfish, marine worms, sea anemones, and fireflies; in the atmosphere, as in the northern and southern auroras; on the beach, due to the effect of batteries (figure 2.5); reactions catalyzed by enzymes; objects of daily use, such as quinine; among others<sup>26, 10</sup>.



Figure 2.5: Bioluminescent bays in Puerto Rico<sup>5</sup>

Shih Ching made the first description of luminescence found to date in 1300 B.C., in his book of Odes, he describes the luminescent processes of fireflies (figure 2.6) and worms<sup>10</sup>. In 384-322 B.C. Aristotle wrote in *De Coloribus* "...some things do not burn by their nature, nor have a fire of any kind, yet they seem to produce light", referring to the light emitted by decomposing fish<sup>57</sup>. This type of luminescence is known as bioluminescence, which

is the emission of visible light in organisms as a result of natural chemical reactions.<sup>58</sup>

The first reference to luminescence as a physical phenomenon was made in 1280 by St. Albert the Great, describing the light emitted by a heated diamond. By the 17th century, it was known that luminescence was reactivated by exposure to light, and it was considered that heat stimulated its emission but was not the cause. With the discovery of X-rays in the 19th century, it was observed that their incidence regenerated the fluorescence of certain minerals, such as fluorites<sup>10</sup> (figure 2.7).



Figure 2.6: Fireflies.<sup>6</sup>



Figure 2.7: Fluorite Mineral.<sup>7</sup>

In 1888, the concept of luminescent substance was described as one that becomes luminous by the action of an external agent without temperature change<sup>10</sup>, the term luminescence being introduced by the chemist Eilhard Wiedemann to encompass the phenomena of fluorescence and phosphorescence<sup>57</sup>. In 1904, Marice Curie mentioned

in her doctoral thesis, "certain bodies, such as fluorite, become luminous when heated: they are thermoluminescent. Their luminosity disappears after a time, but their emission capacity, erased by heat, is renewed by a spark and also by the action of radiation". In 1930, Jablonski defined the current scheme of the luminescent process as a function of energy levels (figure 2.8), which can be represented in band diagrams.<sup>10</sup>

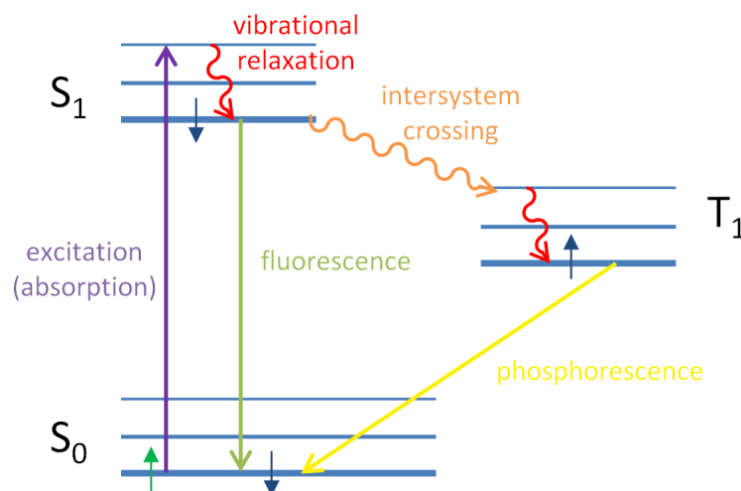


Figure 2.8: Jablonski diagram illustrating the fundamental processes of fluorescence and phosphorescence.<sup>8</sup>

Thanks to the advent of classical mechanics and the classic works of Randall and Willkins in 1945, and Garlick and Gibson in 1948, the theoretical foundation of luminescence was obtained. In 1953, Daniels et al. proposed using thermally stimulated luminescence (LET or TL) in the dosimetry of natural or synthetic materials. This model proposes that solids are made up of atoms arranged in lattices, and electrons are subjected to different potentials. In addition, using the solution of the Schrödinger equation, it is possible to describe the motion of the electrons, which determine a series of intervals or bands of energies based on the Jablonski model.<sup>10</sup>

Among the energy, bands are the valence band and the conduction band (figure 2.9). The valence band is the fundamental level of the atoms; that is, the valence electrons are in the last layer of the atom, which is partially or completely filled. The conduction band is occupied by free electrons unbound to the atom that can move in an excited state, and these electrons are responsible for conducting the electric current. The distance between the two bands is specific for each material and is called the band gap.<sup>10</sup>

In an ideal crystal, the electrons cannot pass this band gap. However, vacancies, impurities, and dislocations, among other defects, produce the appearance of possible energy values for electrons within the forbidden band. Consequently, the excited electrons can jump to the conduction band from the valence band, crossing the band gap and leaving a vacancy in the valence band. Subsequently, the system tends to return to its fundamental state,

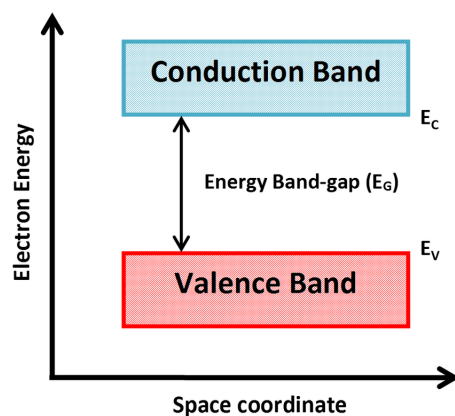


Figure 2.9: Valence and Conduction band<sup>9</sup>

and at that moment, a release of energy occurs, which can be radioactive, with photon emission, or non-radioactive<sup>10</sup>.

### 2.5.1 Luminescence

Luminescence is a natural phenomenon where light emission is practically at room temperature. This phenomenon is also called cold light<sup>26</sup>. The phenomenon is so striking that it even impressed scientists such as Descartes and Bacon or literary writers such as Shakespeare<sup>59</sup>. The physical process of this phenomenon consists of the emission of light by an appropriate material that absorbs energy from a source. This source can be UV, IR, X-rays, chemical reactions, a corpuscular beam (electrons<sup>26</sup>, protons, neutrons, alpha or beta particles), temperature, pressure, electricity<sup>10</sup>, by friction<sup>59</sup>, etc. The absorbed energy takes the atoms of the material to an unstable excited state, and looking for stability; the electrons return to their ground state. During this transition from the excited state to the ground state, the absorbed energy is released in the form of light<sup>26</sup> (figure 2.8). Consequently, this cold emission implicates, first, the excitation of the electronic system to a higher energy state of solid material, second, the photon emission or simply the emission of light<sup>11</sup>. Depending on the time it takes for light to be produced after radiation absorption, luminescence is sub-classified into fluorescence and phosphorescence (figure 2.10).

If the phenomenon is practically immediate, that is, the electron passes from the excited state to the fundamental state instantaneously, this phenomenon is known as Fluorescence, from the Latin "fluo", which means to flow. The luminescence in this phenomenon has a lifetime of about  $10^{-8}$  seconds once the excitation source is removed<sup>26</sup>. This phenomenon is so instantaneous that fluorescence emission is observed simultaneously with the absorption of the radiation and stops immediately when the radiation ceases. Additionally, this process is independent of the temperature.<sup>11</sup> On the other hand, if the phenomenon occurs over a longer time, it is known as phosphorescence, from the Greek "phos" which means light, and "phoros" which means carry. In phosphorescence, electrons pass

very slowly from a metastable state M to the ground state<sup>59</sup>; the luminescence in this phenomenon is maintained for a time longer than  $10^{-8}$  seconds even lasting for hours after removal of the excitation source<sup>26</sup>.

Therefore, phosphorescence is subdivided into two types: short period  $\tau_c < 10^{-4}$ s (Also known as short-lived phosphorescences<sup>60</sup>) and the long period where  $\tau_c > 10^{-4}$ s is called Thermoluminescence (TL). In TL, the emission depends on minutes  $< \tau_c < 4.6 \times 10^9$  years falls into the long period. In phosphorescence, the temperature depends on the process<sup>11</sup> (figure 2.8). On the other hand, this phenomenon in which a material emits light for long periods, even hours, after being excited, can be referred to in different ways such as persistent phosphorescence, long-lasting phosphorescence (LLP), long afterglow, simply phosphorescence<sup>61</sup>, or ultralong phosphorescence<sup>62</sup>.

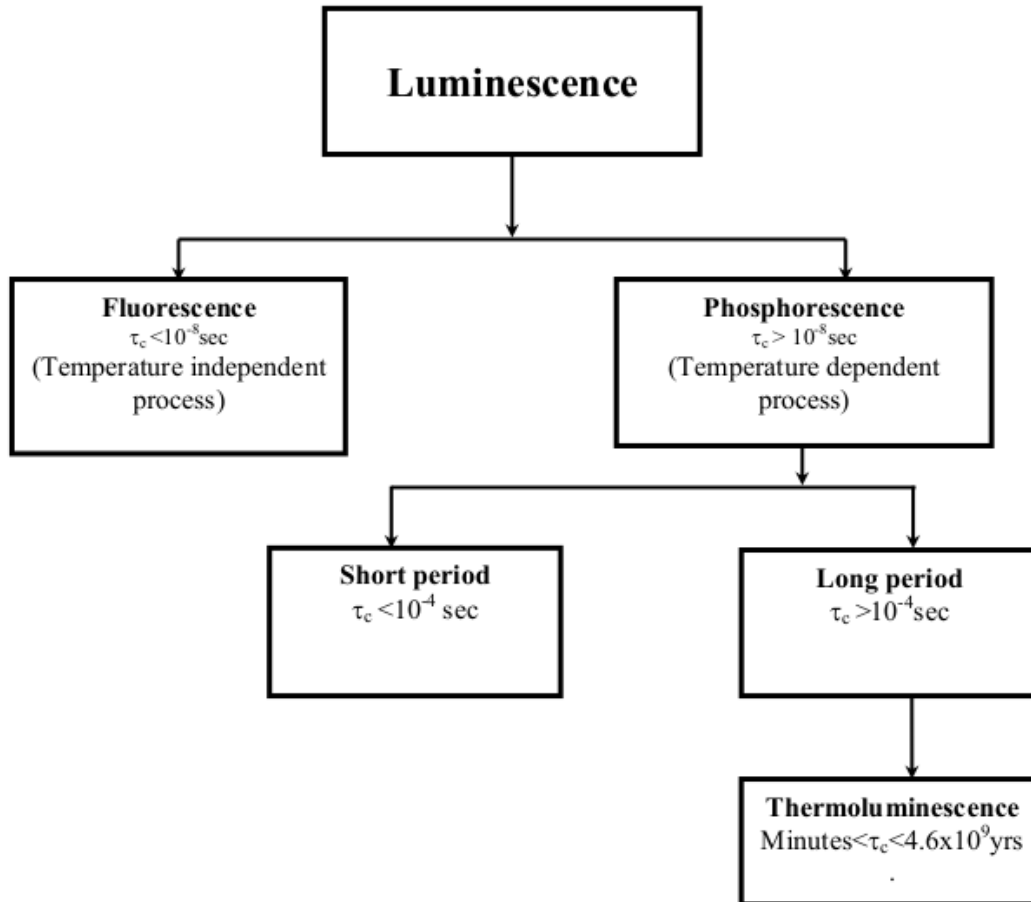


Figure 2.10: Classification of luminescence according to duration time<sup>10</sup>

Phenomenologically fluorescence is the luminescence observed during excitation, whereas the term phospho-

rescence is reserved for the emission that persists even after the excitation radiation source has been removed<sup>63</sup>. In other words, phosphorescence is characterized by the time delay between radiation absorption and the time to reach the maximum intensity ( $\tau_{\max}$ ). In addition, depending on the energy source or the trigger of luminescence, there are several types of luminescence, each of which has its importance and advantage in the fields of science and technology<sup>11</sup>, as shown in Table 2.2.

Luminescence types	Source of excitation	Examples
Bioluminescence and chemiluminescence	Chemical and biochemical reactions	Fireflies, fish, luminol, etc
Photoluminescence	Photons (UV, Visible and IR)	Fluorescent lamps
Electroluminescence	Electric current	LED and electroluminescent screens
Cathodoluminescence	Accelerated Electrons	Displays and Oscilloscopes
Thermoluminescence	Heat	Thermoluminescent dosimeters
Triboluminescence	Friction (mechanical energy)	Tape stripping

Table 2.2: Classification of luminescence depending on the source of excitation<sup>26</sup>.

### 2.5.2 General Characteristics of Luminescence

In the luminescence process, there are two types of returns to the basic state: radioactive and non-radioactive (Figure 2.11). The first, radiative decay, allows the luminescence process to occur<sup>11</sup>. In this process, the molecule discards its excitation energy as a photon<sup>64</sup>. The second, non-radiative decay, does not participate in the luminescence process<sup>11</sup>. In this process, the excess excitation energy is converted into thermal motion of the surroundings (heat) through vibrations, rotations, and translations of the surrounding molecules<sup>64</sup>. Lastly, an efficient luminescent material is one in which radiative transitions dominate over non-radiative transitions<sup>11</sup>.

Furthermore, due to the strong temperature dependence of phosphorescence, metastable states created by defect centers, activators, impurities, electron traps, or holes present in the lattice can delay the luminescent emission causing this effect since thermal activation of the metastable activator or trap is a prerequisite for emission<sup>11</sup>.

#### Production and Decay Process of Excited States

To understand the phenomenon of luminescence, it is necessary to comprehend the processes of production and decay of the excited energy states. This can be explained using the Jablonski diagram since it describes most of the relaxation mechanisms of molecules in the excited state (Figure 2.12). Here are some statements to explain the Jablonski diagram<sup>11</sup>:

- The ground state  $S_0$  and the lower states, singlet  $S_1$  and triplet  $T_1$  are formed by multiple vibrational states due to the presence of vibrational motions of the atoms forming a molecule.

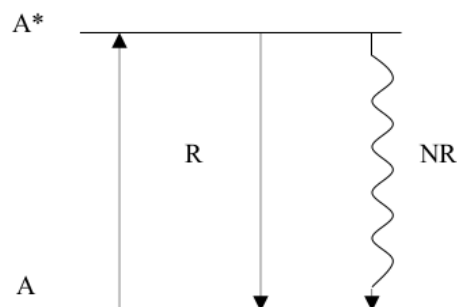


Figure 2.11: Diagram of energy levels of the luminescent ion A. The \* indicates the excited state, R the radiative return, and NR the non-radiative return to the ground state<sup>11</sup>.

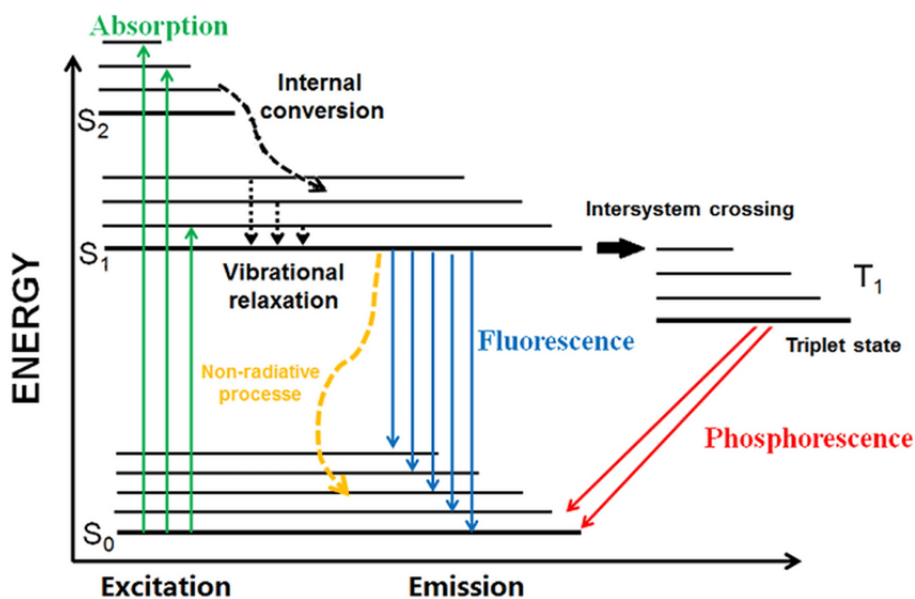


Figure 2.12: Photophysical processes in molecular systems explained by Jablonski diagram<sup>12</sup>.

- By introducing an energy higher than the HOMO – LUMO (highest occupied molecular orbital minus the lowest unoccupied molecular orbital) energy difference into a molecule, a higher vibronic state is produced within the  $S_1$  or higher singlet excited states  $S_2$  and  $S_3$ . Then, the higher vibronic states of  $S_1$  vibrationally relax to the lowest state of  $S_1$  on a picosecond time scale.
- Through non-radiative internal conversion (IC) processes, the higher energy singlet states, such as  $S_2$  and  $S_3$ , relax to the  $S_1$  state.

- Triplet states are generally generated through inter-system crossing (ISC) processes of  $S_1 \rightarrow T_1$ .
- Radiative transitions occur as the electronic transition from the lowest excited states of  $S_1$  or  $T_1$  to the fundamental state  $S_0$ . The radiative transition from  $S_1$  to  $S_0$  is categorized as a spin-allowed transition; therefore, the transition time scale is a few nanoseconds.
- Moreover, the transition time scale from  $T_1$  to  $S_0$  is much longer, varying between microseconds and milliseconds since the process is spin forbidden. In this way, an emission spectrum appears as the mirror image of the molecule's absorption spectrum.

### Luminescence in the Band Scheme

Mineral atoms are closely packed together and strongly interact with each other. Therefore, with small dimensions of the forbidden band, the transfer of electrons from the impurity or the main substance to the conduction band can occur. In this transfer, the electrons leave a free hole in the valence band and move into the conduction band. Depending on the nature of the mineral, certain defects can capture a free electron, causing an electron center, or a free hole causing a hole center. Then, as a result of recombination with the opposite charge carrier, these centers disappear. Finally, this recombination produces energy that serves as a source of excitation for the luminescence center, and it is caused by the emission of photons<sup>13</sup>. Thus, the source of luminescence can vary depending on the process:

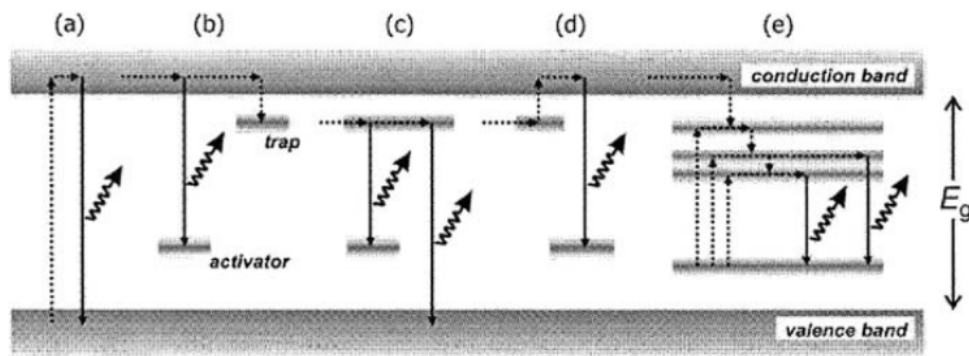


Figure 2.13: Electron band structure of a semiconductor mineral, showing the processes of excitation (energy absorption), non-radiative energy transfer, and luminescence generation<sup>13</sup>.

- "Intrinsic" luminescence in which an electron is excited from the valence band to the conduction band. Then, when the electron returns to the valence band generates a photon. The energy of this photon is equal to the energy difference between the bands (Fig. 2.13a).
- Luminescence by an excited electron that passes from the conduction band to the forbidden band without returning to the valence band. Since it falls into an activator, with the following luminescence, or a trap,

with the following electron capture. Defects cause traps and activator energy levels in the crystal lattice (Fig. 2.13b).

- Generation of luminescence through electrons passing from a trap to an activator (tunneling) or from a trap to a valence band gap (Fig. 2.13c).
- Stimulated release of an electron that first passes from a trap to the conduction band and then passes from the conduction band to an activator emitting a photon. This process is called thermoluminescence (electron release stimulated by heating) and optically stimulated luminescence (electron release stimulated by light) (Fig. 2.13d).
- "Extrinsic" luminescence, in which after being excited, the electrons of the defective ions recombine with the ground state emitting a photon (Fig. 2.13e).

### 2.5.3 Thermoluminiscencia

Thermoluminescence (TL) is a phenomenon in which an insulating or semiconducting solid emits light when it is heated by absorbing radiation energy. In contrast to incandescence, in Thermoluminescence, it is possible to produce visible light at temperatures below red since heat is not the main source of energy but the initiator of the reaction. The ability to emit spontaneous light without reaching a certain degree of heating is due to a process called ionization by irradiation<sup>10</sup>.

The TL phenomenon begins with energy absorption by an insulating or semiconducting material from an ionizing source. The absorption excites the free electrons and holes, which causes these electronic species to be trapped in defects within the material, called trapping states. Once the excitation is removed, the sample is heated so that the thermal energy causes the liberation of charge carriers of one sign (e.g., electrons) that can recombine with charge carriers of the opposite sign. If the recombination is radiative, luminescence (TL) is emitted<sup>14</sup>.

TL involves the perturbation of the system from a state of thermodynamic equilibrium, through the absorption of external energy (ionizing radiation), to a metastable state. The system then relaxes back to its equilibrium state, followed by luminescence emission. In other words, luminescence occurs during transitions of the released charges back to the ground state<sup>14</sup>.

The thermally stimulated process (TPS) may be described in terms of the system's free energy and the equilibrium Fermi level perturbation in the studied material. At thermodynamic equilibrium (0K), it can be expected by Fermi-Dirac statistics that all states above the Fermi  $E_F$  level are empty while all states below  $E_F$  are full. Figure 2.14 depicts an energy band diagram, where  $E_c$  represents the lower part of the conduction band,  $E_v$  the upper part of the valence band, and the distribution of energy states (traps) in the band gap<sup>14</sup>.

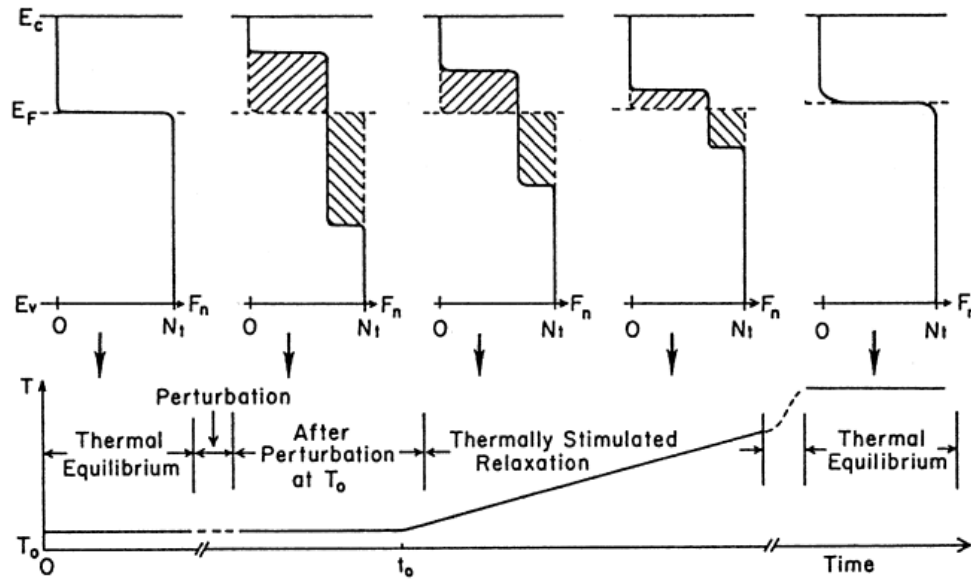


Figure 2.14: BraËunlich (1979) diagram of the filling functions for a uniform distribution of traps before and after perturbation by an external stimulus and during thermally stimulated relaxation.<sup>14</sup>

Figure 2.14 represents the degree of filling of the  $F_n(E)$  energy states in a uniform trap distribution during a thermally stimulated relaxation experiment. The first diagram represents the Fermi-Dirac filling function at 0K. Then, the filling function after an ionizing perturbation is observed. The bar with lines above the  $E_F$  represents a distribution of trapped electrons in states located within the band gap. In turn, the bar with lines below the  $E_F$  represents a distribution of trapped holes. Thus, two quasi-Fermi levels can be defined, one for the electrons  $E_{Fn}$  and one for the holes  $E_{Fp}$ <sup>14</sup>.

These two quasi-Fermi levels are useful for describing the non-equilibrium state following the perturbation in terms of equilibrium statistics, assuming that the populations of trapped electrons and holes are in thermal equilibrium over the available energy levels. Finally, during heating, i.e., during the thermally excited relaxation, the filling function  $F_n(E)$  gradually returns to its state before the perturbation, although now at a higher temperature<sup>14</sup>.

To develop this picture into a simple description of TL, we note several additional definitions and assumptions<sup>14</sup>:

- All transitions into or out of the localized states involve the passage of the charge (electrons or holes) through the delocalized bands (figure 2.15).
- The "recombination center" is defined as one in which the probability of recombination with an opposite sign charge carrier is greater than that of thermal excitation of the trapped carrier. Therefore, one can define a

demarcation level as the energy level at which these two probabilities are equal. Thus, we have a demarcation level for electrons  $E_{Dn}$  and one for holes  $E_{Dp}$ .

- Transitions of electrons from the conduction band ( $E \geq E_c$ ) into electron traps of energy  $E$ , for which  $E_c > E > E_{Dn}$ , are non-radiative, emitting phonons. Similarly, hole transitions from  $E \leq E_v$  to hole traps at  $E_{Dp} > E > E_v$  are also non-radiative.
- Transitions of free electrons from  $E \geq E_c$  to trapped hole recombination sites at  $E_F > E > E_{Dp}$ , or free holes from  $E \leq E_v$  to trapped electron recombination centers at  $E_{Dn} > E > E_F$  are radiative, emitting photons.

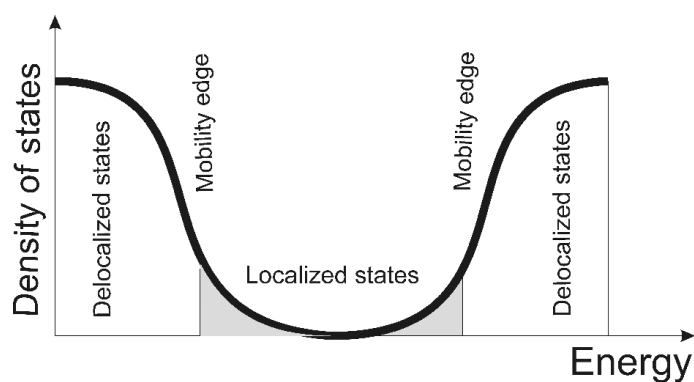


Figure 2.15: Localized and delocalized states in semiconductors<sup>15</sup>.

### 2.5.4 Effect of temperature on luminescence

In the phenomenon of ionization by irradiation, temperature has a fundamental role in luminescence. This is because as the temperature of the solid increases, the charges trapped in the traps are excited and pass to the conduction band. The first charges to pass are those trapped in the bands closest to the conduction band; then, as the temperature increases, the charges trapped in the deeper bands become excited and pass to the conduction band<sup>10</sup>.

On the other hand, radiation increases the number of electrons delocalized in the conduction band, resulting in the probability of their being trapped in the traps. Therefore, the higher the intensity or duration of the radiation, the higher the trap density. Therefore, in thermoluminescence, it is assumed that the recombination phenomenon is produced directly by thermal stimulation, i.e., the TL intensity is proportional to the concentration of trapped electrons leaving the traps<sup>10</sup>.

The TL spectrum of any thermoluminescent material provides information about its structure, as seen in figure 2.16. The position of the temperature maxima is related to the trapping parameters, which are the trap depth ( $E$ ) and the frequency factor ( $s$ ). The intensity of the light is the number of radioactive recombinations produced by a number

n of electrons during a time  $t$ . Finally, the information about the origin of the bands is given by the wavelength, for example, for wavelengths between 450-500nm, they are possibly for structural defects, and for wavelengths above 500nm, they are for point defects<sup>10</sup>.

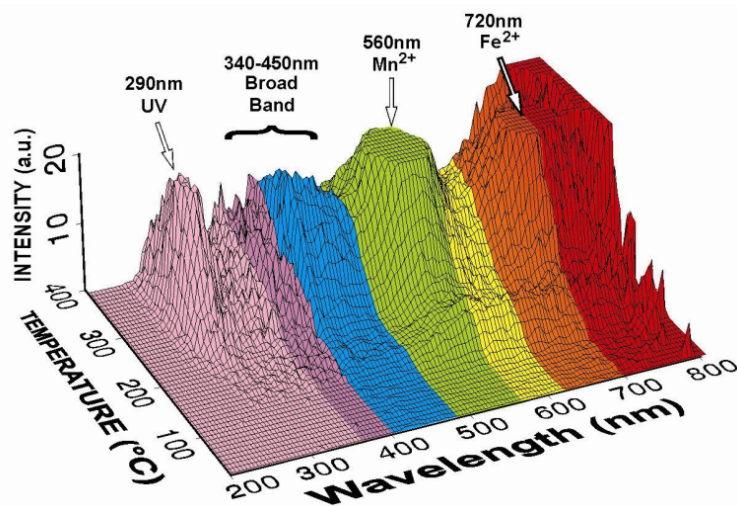


Figure 2.16: TL spectra of albite, a sodium feldspar<sup>10</sup>.

### 2.5.5 Luminescence materials

Any mineral that has the ability to convert certain types of energy into electromagnetic radiation beyond thermal radiation is considered a luminescent mineral. This electromagnetic radiation is usually in the visible range, although it can also be in the ultraviolet (UV) or infrared (IR) range. There are several techniques to excite the luminescence of minerals, including UV and visible radiation (photoluminescence), a beam of energetic electrons (cathodoluminescence), X-rays (luminescence excited by X-rays), etc. In addition, a special case is thermoluminescence; it consists of the stimulation by heating of the luminescence, previously excited in a different form<sup>13</sup>.

Luminescent minerals are composed of a host lattice and a luminescent center, usually called activators. Determining the nature of the activating center is usually not easy. However, spectroscopic studies provide several important parameters to help identify the luminescence center. For many luminescence centers, the intensity is a function of a specific orientation relative to the crystallographic directions of the mineral. Even when a center consists of an atom or ion, this luminescence anisotropy may be produced by a compensating impurity or intrinsic defect. However, it is important to note that not all minerals are luminescent since, as a consequence of a non-radiative return to the ground state, the energy of the excited state is used to excite the vibrations of the host lattice, i.e., energy is released in the form of heat<sup>13</sup>.

Several properties and characteristics of the luminescence of different minerals have been related to the crystalline-chemical and structural state of the species. However, it is also expected to associate the luminescence behavior with the different conditions of formation and alteration of the mineral<sup>13</sup>. Optically active centers generate optical transitions by introducing a series of energy levels into the gap band of the material. These centers can be impurities introduced to the crystal lattice at the time of growth, such as rare earth ions and transition metals, or lattice defects, color centers, which provide a variety of optical properties<sup>65</sup>.

### 2.5.6 Hydroxyapatite Luminescence Properties

Hydroxyapatite is a host material. This compound is doped (impurities) to modify its physical and chemical properties since it is usually inert, i.e., it is not excited by incident photons and does not emit photons. The dopant in the host material is often named "optically active ion" because the ions are responsible for the luminescent properties of the host-dopant system<sup>66</sup>.

Many investigations have reported that the luminescent properties of hydroxyapatite are due to impurities. The defective structure of hydroxyapatite and many of the special properties of this material are attributed to OH groups<sup>67</sup>. Additionally, the effect of thermal treatments on the optical properties of HA nanoparticles is reported and is attributed to order-disorder changes induced by impurities, OH vacancies, and the presence of  $\text{CO}_3^{2-}$  ions that decompose at high temperatures<sup>68</sup>. Furthermore,  $\text{CO}_2^-$  radicals in the interstitials of the hydroxyapatite lattice are proposed to be responsible for the blue self-activated luminescence with a peak of approximately 428 nm at room temperature<sup>69</sup>. Finally, another investigation evaluated the effect of surface hydrogenation treatments and microwave irradiation on the photoluminescence properties of Ha, attributing the photoluminescence response to the increase in defect concentration<sup>70</sup>. Consequently, considering hydroxyapatite as a host material, doping with europium is proposed to enhance the intensification of its luminescent properties.

### 2.5.7 Europium Luminescence Properties

Rare earth or lanthanides are found in the "f" group of the periodic table. The lanthanides consist of elements ranging from lanthanum to lutetium, as well as scandium and yttrium<sup>66</sup>. A characteristic property of these elements is that most absorb wavelengths in the ultra-violet or visible region of the spectrum, generating transitions in the 4f orbitals<sup>71</sup>. These transitions are incredibly independent of the medium because the external  $5s^2 5p^6$  shells well protect the  $4f^n$  electrons, and the influence of the crystal field is weak<sup>16,66</sup>.

Due to the  $4f^{n*} \rightarrow 4f^n$  transitions of the valence electrons, most trivalent rare earth ions have luminescent emission in the visible spectrum or near-infrared region.  $\text{Eu}^{3+}$  has an intense red luminescent emission due to the  $^5\text{D}_0 \rightarrow ^7\text{F}_J$ , ( $J=0,1,2,3,4,5,6$ ) levels of the  $4f^6$  configuration. Since the  $^5\text{D}_0$  level has no splitting due to the influence of the

crystalline field ( $J=0$ ), the splitting of the emission transition leads to the splitting of the crystalline field of the  ${}^7F_J$  levels<sup>16,66</sup>. Moreover, as the transitions occur between states of the same parity, the lifetime of the excited state is long<sup>16</sup>.

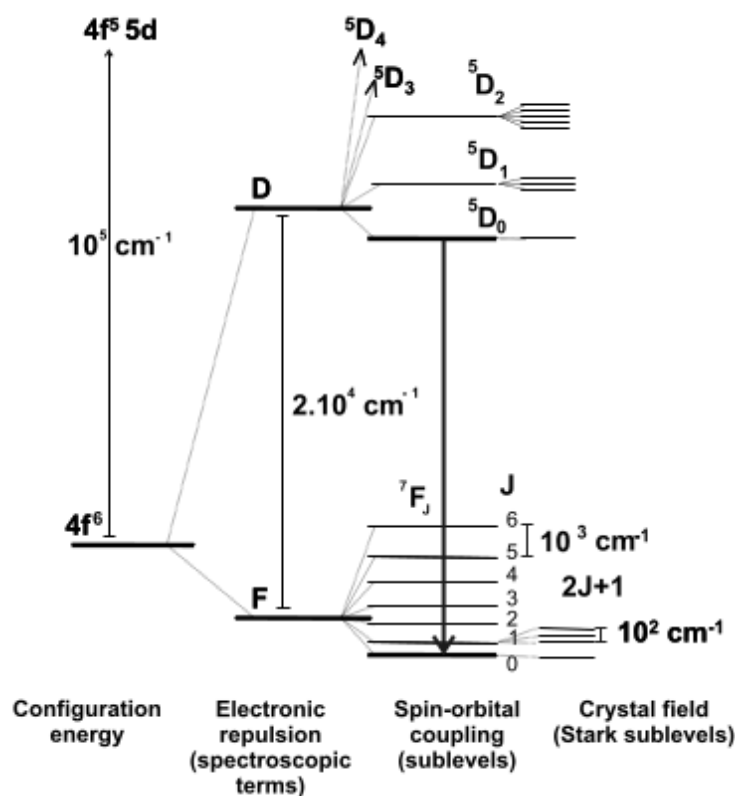


Figure 2.17: Energy levels scheme of  $\text{Eu}^{3+}$ <sup>16</sup>

On the other hand, these transitions have other essential characteristics. As shown in Figure (2.17), the ions have electronic transitions between energy sublevels of the  $4f^n$  configuration; this is because, in trivalent ions, the electrons of the 5d, 6s, and some of the 4f levels are removed<sup>66</sup>. These energetic sublevels are called Stark sub-levels and are produced by the crystal field<sup>16</sup>, by the Stark effect.  $\text{Eu}^{3+}$  is known for its intense luminescence and its characteristic Stark structure<sup>72</sup>.

In addition, most luminescent systems have only one excited state that emits photons. It is usually the lowest energy state; such is the case of  $\text{Eu}^{3+}$ , whose only emitting state is  ${}^5D_0$ . This results from a very fast non-radiative relaxation between higher energy levels since the minimum phonon vibration energy have a considerable value. Therefore, few phonons are required to pass from one energy level to the next lower level<sup>66</sup>. The most studied rare earth ions ( $\text{Ln}^{3+}$ ) in the generation of visible light by down conversion are  $\text{Eu}^{3+}$ ,  $\text{Tm}^{3+}$ ,  $\text{Tb}^{3+}$ ,  $\text{Sm}^{3+}$ ,  $\text{Dy}^{3+}$ ,  $\text{Ce}^{3+}$ ,  $\text{Pr}^{3+}$ , and  $\text{Er}^{3+}$ . This

means that the emitted photon has lower energy than the excitation photon<sup>66</sup>.

### 2.5.8 Factors influencing luminescence

Fluorescence is a radiative process during which excess energy is emitted as photons. However, external conversion or dynamic quenching is a non-radiative process that competes with fluorescence to release this energy. Dynamic quenching consists of the release of energy by interaction with other molecules in the system<sup>73</sup>. For this reason, several factors affect luminescence: molecular structure, chemical environment, solvent, pH of the solution, temperature<sup>74</sup>, quantum yield<sup>75</sup>, and others.

**Quantum yield effect:** describes the ratio of the number of molecules emitting fluorescence to the total number of excited molecules, also known as the quantum fluorescence efficiency<sup>75</sup>.

**Effect of molecular structure:** understanding that the more radiation a molecule absorbs, the more intense it will be its luminescence, and that is the reason why molecules with conjugated double bonds, especially those with high resonance energy, such as aromatic hydrocarbons, usually show a high fluorescence<sup>74</sup>. The quantum efficiency increases with the number of rings, and with their degree of conjugation, the luminescence is more intense in compounds with aromatic functional groups<sup>75</sup>. Especially those with a multicyclic structure, rigid and flat. The rigidity of the molecular structure is a crucial factor in fluorescence since low rigidity allows the absorbed energy to be released by non-radiative mechanisms<sup>74</sup>.

**Effect of pH:** The fluorescence of a compound with acidic or basic groups is usually pH-dependent. The wavelength and emission are different for the ionized and non-ionized forms of the compound. A more significant number of resonant forms gives excellent stability to the first excited state, allowing a higher probability of fluorescence<sup>74</sup>.

**Effect of solvent:** The probability of external conversion, a non-radiative process, enhances with increasing collisions between molecules. Increased collisions may result from a decrease in the viscosity of the solvent.<sup>74, 75</sup>

**Effect of dissolved oxygen:** the paramagnetic properties of molecular oxygen favor intersystem crossing and the conversion of excited molecules to the triplet state, producing a damping of fluorescence.<sup>74, 75</sup>

**Effect of temperature:** as with the solvent, the increase in temperature can decrease the fluorescence intensity since it increases the collisions between molecules and the probability of deactivation by non-radiative phenomena (external conversion)<sup>73, 74, 75</sup>.

**Effect of concentration:** it would be expected that increasing the optically active ions in the host matrix would increase the luminescence intensity simultaneously. Nevertheless, this is true for a specific critical value in the

concentration of the luminescent centers. Above this critical value, the luminescence begins to decrease. This phenomenon is known as inhibitory concentration, which reduces the distance between neighboring luminescent centers by increasing the concentration, facilitating the transfer of energy between them<sup>66</sup>.

This transfer of energy between neighboring luminescent centers can produce self-quenching and self-absorption. Self-absorption results from collisions between molecules that release energy by non-radiative processes. Self-absorption occurs when the radiation emitted by one molecule is reabsorbed by other molecules that are also fluorescent<sup>74</sup>. This concentration of ions or defects (luminescent centers) acts as energy wells called traps or annihilators<sup>66</sup>. In addition, it is essential to mention that there is the possibility that high concentrations produce new types of luminescent centers, such as clusters formed by the union of individual centers. Consequently, this new type of center has a different energy level scheme than isolated optically active ions. They give rise to new absorption and emission bands<sup>66</sup>.

## 2.6 State of the art

### 2.6.1 Hydroxyapatite doped Europio systems

Hydroxyapatite doped with europium has excellent physicochemical properties, which highlights the luminescence. Due to these properties, there is an enormous variety of applications and research that have been carried out in recent years, such as

In nanomedicine, the doping of hydroxyapatite with europium is of great interest as biocompatibility and light emission are required. Xuan et al. state in their research that the synthesis of Eu-doped Ha by the hydrothermal method shows an increase of the photoluminescence intensity in the sample due to the characteristic  $\text{Eu}^{3+}$  emission<sup>24</sup>. Also, the cell labeling method using biocompatible inorganic nanoparticles investigated by Han et al. presents a potential biocompatible fluorescent labeling material. These nanoparticles were synthesized under the precipitation method and used to label Bel-7402 human liver cancer cells as a fluorescent probe. The researchers observed strong green fluorescence with blue light excitation and strong red fluorescence with green light excitation. This luminescence was temporally stable and could be excited by wavelengths in the visible region<sup>42</sup>.

Furthermore, Ciobanu et al. studied the luminescent properties of Hydroxyapatite Nanocrystalline Powders doped with europium at an atomic ratio of (Eu: HAp,  $\text{Ca}_{10-x}\text{Eu}_x(\text{PO}_4)_6(\text{OH})_2$ ) with  $0 \leq x \leq 0.2$ , obtained by the co-precipitation method at low temperatures. The researchers found that as the atomic ratio of  $\text{Eu}/(\text{Ca}+\text{Eu})$  increased, the photoluminescence intensity of the samples increased. Demonstrating that this luminescent property is a potential application for drug release and targeting<sup>19</sup>. Other authors propose europium-doped hydroxyapatite (Eu: HAp) via a simple one-step route using a cationic surfactant as a template for a potential application in drug delivery and disease therapy based on its bioactive, luminescent, and mesoporous properties. This research was conducted by Yang et al., who obtained multifunctional hydroxyapatite used as a drug carrier to investigate drug

storage/release properties using ibuprofen (IBU) as a model drug. This material can be easily tracked and monitored in the drug release process by the change of PL emission intensity because it exhibits high red luminescence and PL intensity that increases with the accumulated amount of released IBU<sup>43</sup>.

It is also possible to test for the antimicrobial activity of pathogenic bacteria and fungi using these nanoparticles. Iconaru et al., demonstrated that the concentration of europium in Eu: HAp nanoparticles significantly influence antimicrobial activity. They used Fourier transformed infrared spectroscopy (FT-IR) to test the antimicrobial activity of Eu: HAp ( $0 \leq x_{Eu} \leq 0.2$ ) nanoparticles on bacterial pathogens and fungus such as *E. coli* ATCC 25922 (Gram-negative), *Pseudomonas aeruginosa* (Gram-negative), *Staphylococcus aureus* 0364 (Gram-positive), *Enterococcus faecalis* ATCC 29212 (Gram-positive), and *Candida albicans* ATCC 10231 (fungus). They further propose that the luminescent property of Eu<sup>3+</sup>-doped hydroxyapatite could interest academic and industrial researchers in biomaterials, potential orthopedic medical materials, and drug carriers<sup>41</sup>.

On the other hand, these nanoparticles can be used in other areas of science, since they present a wide variety of physicochemical properties, such as, for example, the excellent capacity of adsorbing heavy element ions in aqueous conditions. Constantin et al. synthesized nanocrystalline hydroxyapatite doped with europium powders with controlled parameters and excellent stoichiometry as a possible new material to remove heavy metals and other toxic elements from contaminated soil and water conducted<sup>76</sup>. Finally, these are some examples of the many applications of europium-doped hydroxyapatite nanoparticles, mainly having a strong impact on nanomedicine.

## 2.7 Experimental Characterization Techniques

### 2.7.1 X-ray diffraction

High-tech X-ray diffraction is a non-destructive technique that allows the analysis of a diverse range of materials, such as liquids, metals, minerals, polymers, catalysts, plastics, pharmaceuticals, thin-film coatings, ceramics, solar cells, and semiconductors. Analysis of XRD can easily detect the presence of defects in a particular crystal, its level of tensile strength, its texture, its size and degree of crystallinity, and practically every other variation related to the basic structure of the sample<sup>18</sup>.

The phenomenon of X-radiation was discovered by Wilhelm Conrad Roentgen more than a century ago. This discovery proved that X-rays have wavelengths in the Angstroms range, which have sufficient energy to penetrate a solid and scan its internal structure<sup>77</sup>. Additionally, in 1912, it was discovered by Max von Laue and company that crystalline substances act as three-dimensional diffraction gratings for X-ray wavelengths similar to the spacing of planes in a crystal lattice<sup>18</sup>. On the other hand, it is considered that the interaction of waves with periodic structures produces diffraction effects if the wavelength and periodicity of the crystals are of similar magnitude. Consequently, the "quality" of the diffraction effects in XRD is highly dependent on the strict and unchanged periodicity of the

atoms<sup>17</sup>.

Since the atoms have diameters of the order of Ångströms ( $1 \text{ \AA} = 10^{-10} \text{ m}$ ), i.e., the unit cells have dimensions of several Å, and the X-rays have wavelengths of the order of  $10^{-10} \text{ m}$ . The electric field of these waves can interact with the charges of all the electrons of an atom, and as a result, the electrons produce an almost spherical wave with a similar wavelength as the incident radiation<sup>17</sup>. It is, therefore that X-ray diffraction is the elastic scattering of X-ray photons by atoms in a periodic lattice. Scattered monochromatic X-rays that are in phase give constructive interference. Figure 2.18 shows how X-ray diffraction through the crystal planes allows the lattice distances to be deduced by Bragg's law<sup>77</sup>.

$$n\lambda = 2d\sin\theta \quad (2.10)$$

where  $n$  is an integer called the order of reflection,  $\lambda$  is the wavelength of x-rays,  $d$  is the characteristic spacing between the crystal planes of a given specimen and  $\theta$  is the angle between the incident beam and the normal to the reflecting lattice plane. It is possible to determine each crystallographic phase's interplanar spacings,  $d$ , by measuring the angles,  $\theta$ , under which the constructively interfering X-rays leave the crystal<sup>77</sup>. On the other hand, this outgoing wave amplitude is related to the number of electrons in the atom and, therefore, to the atomic number. Consequently, light elements with few electrons are "bad" scatterers of X-rays, such as carbon or oxygen, while heavy elements are "good" scatterers, such as lead<sup>17</sup>.

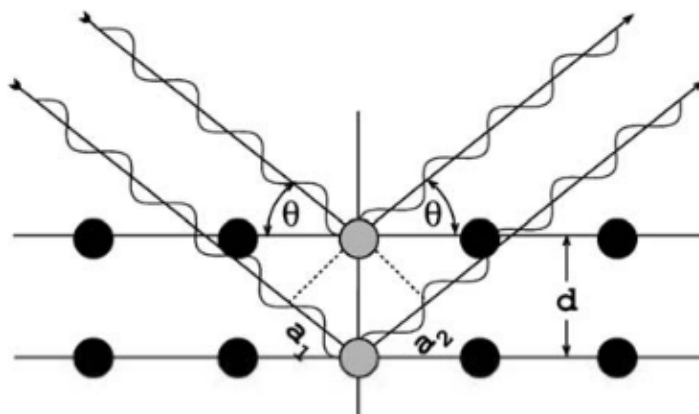


Figure 2.18: Geometric derivation of Bragg's law: constructive interference occurs when the lattice delay between waves scattered from adjacent lattice planes, given by  $a_1 + a_2$ , is an integer multiple of the wavelength  $\lambda$ .<sup>17</sup>.

The X-ray diffractometer has three basic elements: an X-ray tube, a sample holder, and an X-ray detector (Figure 2.19). X-rays are produced in a cathode ray tube by heating a filament to generate electrons, these electrons are then

accelerated and bombarded toward a target material by applying a voltage. The characteristic X-ray spectrum is produced when the incident electrons have sufficient energy to dislodge electrons from the inner shell of the target material. Characteristic X-ray spectra consist of several components, the most usual being  $K_\alpha$  and  $K_\beta$ .<sup>18</sup>

The most commonly used target material for single crystal diffraction is copper, with a radiation  $\text{CuK}_\alpha = 1,5418 \text{ \AA}$ . These X-rays are collimated and directed at the sample. By rotating the sample and the detector, the intensity of the reflected X-rays is recorded. Constructive interference occurs when the geometry of the incident X-rays incident on the sample satisfies Bragg's law, and an intensity peak appears. Finally, this X-ray signal is recorded and processed by a detector, and the signal is converted into a count rate, which is sent to a device such as a printer or a computer monitor. An X-ray diffractometer geometry is given by the sample rotating in the path of the collimated X-ray beam at an angle  $\theta$  while the X-ray detector is fixed on an arm to collect the diffracted X-rays and rotates at an angle of  $2\theta$ . A goniometer is an instrument used to maintain the angle and rotate the sample.<sup>18</sup>

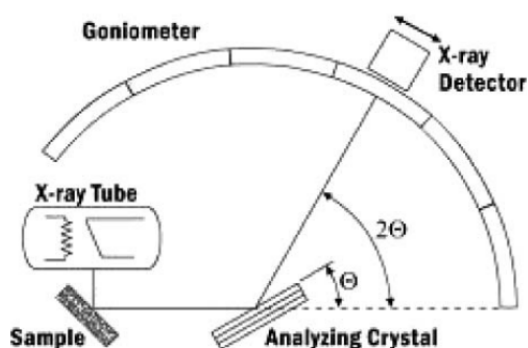


Figure 2.19: Schematic diagram of a diffractometer system<sup>18</sup>.

The expected XRD patterns for the europium-doped hydroxyapatite,  $\text{Ca}_{10-x}\text{Eu}_x(\text{PO}_4)_6(\text{OH})_2$  prepared with different  $x$  values ( $0 \leq x \leq 0.2$ ), are shown in Figure 2.20. It is evident that all the XRD diffractions of each sample can be well indexed as a pure hexagonal phase (space group  $\text{P6}_3/\text{m}$ ). For pure hydroxyapatite samples, diffractions characteristic of hexagonal HA is still evident, and no other europium-related phases can be detected. Samples with  $x = 0.01$  (HAp E1) and  $x = 0.02$  (HAp E2) are almost identical from the XRD point of view with undoped HAp ( $x = 0$ ), showing very small differences in terms of relative peak intensities. Furthermore, for  $x = 0.1$  and  $x = 0.2$ , the relative intensities of the diffractions are observed to decrease with increasing Eu concentration, suggesting that doping inhibits HA crystal growth. In addition, the Eu fluorescence excited by the absorption of  $\text{CuK}_\alpha$  radiation in the Eu L-layer may contribute substantially to this increase in background intensity. (The cross-section of the photoelectric effect is quite large ( $412.5 \text{ cm}^2/\text{g}$ ) because the Eu L-absorption edges,  $E_{\text{EuL2}} = 7.617 \text{ KeV}$  and  $E_{\text{EuL3}} = 6.977 \text{ KeV}$ , approximate the energy of the  $\text{CuK}_\alpha$  radiation used for the analysis ( $E_{\text{CuK}_\alpha} = 8.049 \text{ KeV}$ )).<sup>19</sup>

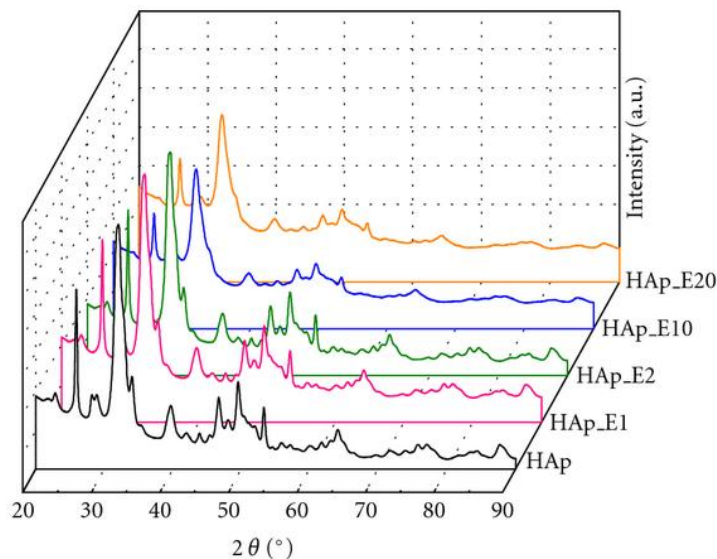


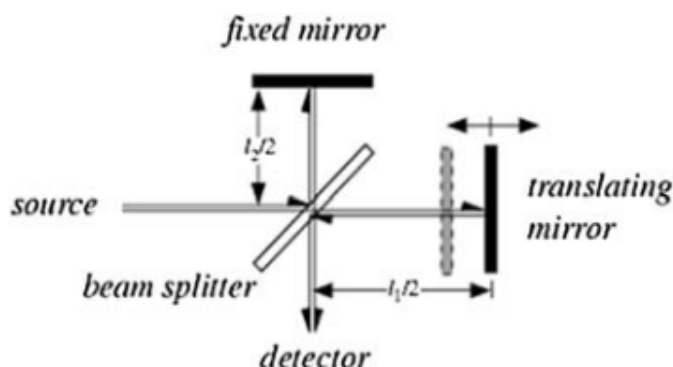
Figure 2.20: The XRD patterns of HAp and Eu:Hap synthesized with  $0 \leq x \leq 0.2$ .<sup>19</sup>

### 2.7.2 Fourier-transform infrared spectroscopy

FTIR spectroscopy has been a standard analytical tool for lignin chemists since the early 1950s. In earlier years, IR spectra were registered by the so-called scattering technique, i.e. with grating or prism-type instruments. Nevertheless, during the last decade, Fourier transform infrared spectrometers (FTIR) have been gaining ground in routine laboratory work<sup>78</sup>. The main difficulty with scattering instruments was the slow scanning process, so FTIR spectrometry was developed as a method to measure all IR frequencies simultaneously, rather than individually. This was achieved with an optical device called an interferometer, which produces a single signal, which has all the IR frequencies "encoded" in it. In addition, since the signal is measured in seconds, the time element per sample is reduced<sup>79</sup>.

In an FT, there are three basic components of the spectrometer: a radiation source, an interferometer, and a detector (Figure 2.21). Most interferometers use a beam splitter, which receives the incoming IR beam and splits it into two optical beams. One of the beams is reflected onto an at-type mirror that is fixed in place. The other beam is reflected onto an at-type mirror with a mechanism that allows this mirror to move a very near distance (usually a few millimeters) from the beam splitter. Since the path traveled by one beam is of fixed length and the other changes continuously as its mirror moves, the signal coming out of the interferometer results from the "interference" of these two beams with each other. This signal is called an interferogram<sup>79</sup>.

IR photons have sufficient energy to vibrate atom groups with respect to the bonds that join them. Just like

Figure 2.21: Schematic diagram of Michelson interferometer.<sup>20</sup>

electronic transitions, vibrational transitions have different energies. For that reason, IR radiation is absorbed by molecules only at specific wavelengths and frequencies. When exposed to IR radiation, chemical bonds vibrate at characteristic frequencies because they absorb radiation at frequencies that correspond to their vibration modes. Consequently, a spectrum representing the absorption frequency of the radiation is generated, which can be used to determine the functional groups and compounds. On the other hand, some impurities produce their characteristic bands in the IR region, which are used to determine impurity concentrations and their binding to the host material. Finally, the frequency spectrum obtained from the interferogram signal cannot be interpreted directly and is "decoded" by a mathematical technique called the Fourier transform (FT)<sup>79</sup>.

FT-IR spectroscopy applies the Fourier transform of an optical interferogram to obtain absorption, reflection, emission, or photoacoustic spectrum. It is a powerful method because of its ability to analyze many frequency components simultaneously in a single operation. FT-IR spectrometer principle is as follows: First, an interferogram is generated, which is a signal generated by the interferometer. This is obtained from recording the signal (intensity) by the infrared detector as a function of the path difference between the two interferometer beams. The interferogram is then Fourier transformed to obtain the spectrum. In this, the intensity, which is a function of the path difference  $x$ , is subjected to an ensemble transform to give the spectrum  $S$ , which depends only on the frequency  $\nu$ <sup>80</sup>. Therefore,

$$S(\nu) = \int_{-\infty}^{+\infty} I(x)e^{+i2\pi\nu x} \cdot dx = \mathbf{F}^{-1}[I(x)] \quad (2.11)$$

in which

$$I(x) = \int_{-\infty}^{+\infty} S(\nu)e^{-i2\pi\nu x} \cdot d\nu = \mathbf{F}[S(\nu)] \quad (2.12)$$

where the first integral is the inverse Fourier transform (equation 2.11) and the second integral is the Fourier transform (equation 2.12). Hence, the integral given by equation (2.11) converts the interferogram  $I(x)$ , which is

a function of the path difference  $x$ , into the spectrum ( $\nu$ ), which in turn is a function of the frequency  $\nu$  (from the spatial domain to the wavenumber domain). This calculation is performed computationally<sup>80</sup>.

FT-IR results of europium-doped Hydroxyapatite similar to Figure 2.22 are expected. All samples have a strong OH vibrational peak ( $632\text{cm}^{-1}$ ). Broad bands in the regions  $1600\text{-}1700\text{cm}^{-1}$  and  $3200\text{-}3600\text{cm}^{-1}$  correspond to the H-O-H bands of lattice water. Strong absorption bands at  $3429\text{cm}^{-1}$  were assigned to OH and H<sub>2</sub>O for all samples. Bands characteristic of phosphate and hydrogen phosphate groups in the apathetic environment:  $565\text{cm}^{-1}$ ,  $632\text{cm}^{-1}$ ,  $603\text{cm}^{-1}$ ,  $962\text{cm}^{-1}$ , and  $1000\text{-}1100\text{cm}^{-1}$  for  $\text{PO}_4^{3-}$  groups and at  $875\text{cm}^{-1}$  for  $\text{HPO}_4^{2-}$  ions. The  $\text{CO}_3^{2-}$  band present in the spectra with  $\text{Eu}/(\text{Ca} + \text{Eu})$  atomic ratio higher than 10% at  $1400\text{cm}^{-1}$  and  $1508\text{cm}^{-1}$ . The intensity of the vibration peak decreases with increasing Eu concentration. Also, a broadening of the vibrational peak with decreasing Eu concentration, suggesting these results that the amount of HA:Eu specific surface area increases with Eu concentration<sup>19</sup>.

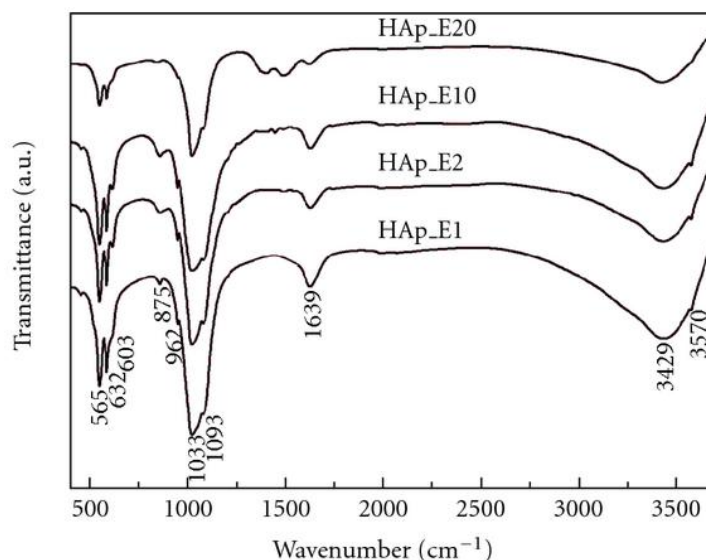


Figure 2.22: Transmittance infrared spectra of HA:Eu samples synthesized with  $\text{Eu}/(\text{Ca} + \text{Eu}) = 1\%$ ,  $2\%$ ,  $10\%$  and  $20\%$ <sup>19</sup>.

### 2.7.3 Scanning Electron Microscopy

Scanning electron microscope (SEM) invented in the 1960s<sup>81</sup> is considered to be one of the most versatile devices for the study of the morphology of micro-structures and the characterization of chemical compositions<sup>82</sup>. The images of an SEM are obtained from the interaction between a high energy electron beam and matter, where in contrast to an optical image, the scanning electron microscope does not form an accurate image of the sample instead, it

reconstructs a virtual image from some signals emitted by the sample. These signals provide information about topography, composition, and crystallographic structure<sup>83</sup>. The interaction of the electron beam with the sample is divided in two ways,

Elastic interactions, where the incident electron loses some energy after interacting with the sample. This is because when an electron passes close to an atom, a series of interactions are produced that deviate from the direction of the electron's movement. This deviation implies a loss of energy. For the electrons to leave the sample, they must have an angle greater than  $90^\circ$ ; considering that the deviation angle varies between  $0^\circ$  to  $180^\circ$  (Book), not all electrons succeed. Elastically scattering electrons are commonly used for SEM imaging and are called Back Scattered Electrons (BSE). This scattering is most common in species with high atomic number<sup>81</sup>.

Inelastic interactions are those that produce instability in the sample by transferring kinetic energy to the atoms. As a result, the electron is trapped in the sample producing a high energy state and a net negative charge. Then, to stabilize the system, it returns to its initial state by re-emitting lower energy electrons to the incident beam electrons, called secondary electrons (SE). In this phenomenon, multiple interactions take place that causes numerous and different levels of excitation in the atom. Thus, besides the primary electrons, it also produces high-energy photons (X-rays) generated in the electronic rearrangements of the layers, photons of energy in the visible zone, infrared photons coming from the transitions between the outermost electronic layers, discharge currents, etc<sup>81</sup>. These signals vary depending on the region of the sample from which the electron escapes<sup>82</sup> (Figure 2.23). Finally, this scattering is more frequent in species with low atomic numbers and provides a lot of information about the sample surface and its elemental composition<sup>81</sup>.

SEM provides diverse and complementary information on all these effects occurring simultaneously, and hence several detectors are used for each of them. However, SE electron emission and X-rays are the most commonly used in scanning electron microscopy<sup>81</sup>.

The configuration of the SEM is given by (Figure 2.24), an electron gun, which produces electrons and accelerates them to an energy level of 0.1-30 keV. Originally this gun is made of tungsten which generates an electron beam that is too large to form a high-resolution image<sup>82</sup>. However, this gun is being replaced by the *LaB6* cathode and the field emitting cold cathode<sup>83</sup>. To reduce the beam amplitude, the beam passes through electromagnetic lenses and apertures to focus and sharpen it. This process demagnetizes the electron source size (  $50\ \mu\text{m}$  for a tungsten filament) to the required final spot size (1-100 nm). Additionally, a high vacuum environment allows the electrons to travel without scattering in the air. Finally, the specimen stage, electron beam scanning coils, signal detection, and processing system provide real-time observation and image recording of the specimen surface<sup>82</sup>.

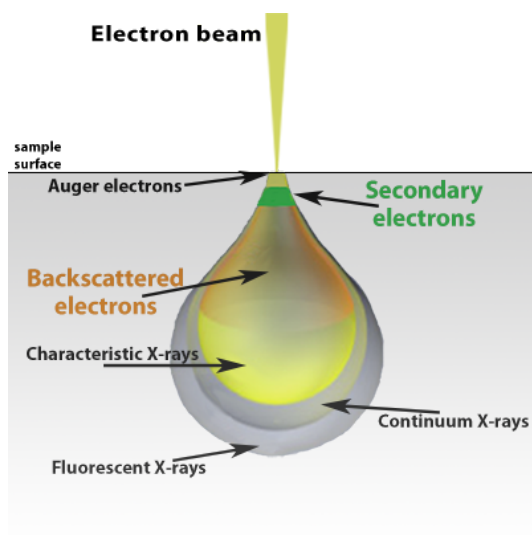
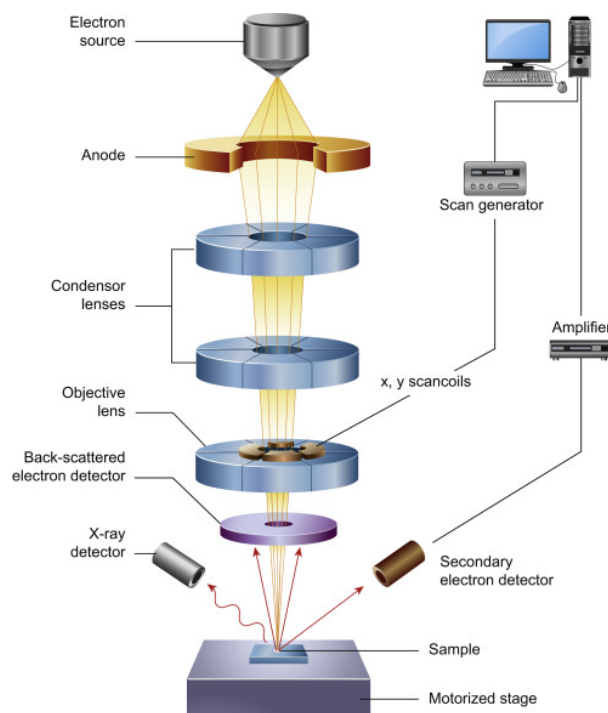


Figure 2.23: Illustration of several signals generated by the electron beam–specimen interaction in the scanning electron microscope and the regions from which the signals can be detected.<sup>21</sup>

### 2.7.4 Raman Spectroscopy

In 1923, the Raman effect was predicted by Smekal but was first observed in 1928, by Sir Chandrasekhra Venkata Raman, for whom it is named<sup>13</sup>. In the first experiments, Sir Raman used sunlight as a source, a telescope as a collector, and his eyes as a detector<sup>84</sup>, and based on the visual observation of color changes in the scattered light. This phenomenon consists in describing the inelastic scattering of light by matter. Considering that a photon of visible light has very low energy to excite an electronic transition<sup>13</sup>, Raman scattering does not require the incident radiation to coincide with the energy difference between the basic and excited states<sup>85</sup>.

The phenomenology of Raman spectroscopy consists of the interaction of the sample with the incidence of a single frequency, which produces radiation scattered by the molecule in a vibrational unit of energy different from the incident beam. In other words, the light interacts with the molecule and distorts (polarizes) the electron cloud around the nuclei to form a short-lived state called a "virtual state". Since this state is not stable, a photon radiates rapidly. Thus, the energy changes detected in vibrational spectroscopy are those necessary to trigger nuclear motion. It is understood that at room temperature most, if not all, molecules are at the lowest energy vibrational level. Furthermore, considering that the virtual states are not real states of the molecule, but arise from the polarization generated by the laser's interaction with the electrons, the energy of these states will be determined by the frequency of the incident beam<sup>85</sup>. In Raman spectroscopy, the incident beam is in the UV-visible ( $\nu_0$ ) region and the scattered light is generally observed in the direction perpendicular to the incident beam<sup>84</sup>. The scattered light consists of two types:

Figure 2.24: Scanning Electron Microscope Diagram.<sup>22</sup>

Rayleigh scattering is an elastic scattering and is dominant, most photons are scattered in this way. In this scattering the interaction between the electron beam and matter only produces a distortion of the electron cloud, as a result of the electrons being comparatively light, the resulting photons are scattered with negligible frequency changes<sup>85</sup>. In other words, this scattering has the same frequency as the incident beam<sup>84</sup>, and since the process does not involve any energy change, the light returns to the same initial energy state<sup>85</sup>.

Raman scattering is inelastic scattering due to the energy of the scattered photon being different from the energy of the incident photon in a vibrational unit. This occurs because nuclear motion is induced during the scattering process, i.e., the incident photon transfers energy to the molecule, or the molecule transfers energy to the scattered photon. It is an extremely weak process; only one out of every  $10^6$ - $10^8$  photons is scattered in this way<sup>85</sup>. The frequency of this scattering is given by  $\nu_0 \pm \nu_m$ , where  $\nu_m$  is a vibrational frequency of a molecule. Measuring the vibrational frequency ( $\nu_m$ ) as a shift of the frequency of the incident beam ( $\nu_0$ ), it can be determined if it is a Stokes ( $\nu_0 - \nu_m$ ) or anti-Stokes ( $\nu_0 + \nu_m$ ) scattering<sup>84</sup> (Figure 2.25).

Stokes scattering is when the molecule absorbs energy from the incident electron, and it passes from a funda-

mental vibrational state ( $E_0$ ) to an excited vibrational state of higher energy ( $E_0 + hv_m$ ). Anti-Stokes scattering occurs when, due to thermal energy, the molecule is in an exciting initial vibrational state ( $E_0 + hv_m$ ), and by the interaction with the incident electron, it passes to a ground state ( $E_0$ ), transferring energy to the scattered photon<sup>85</sup> (Figure 2.25). Finally, the quantum theory of Raman scattering provides that the vibrational energy of a molecule is quantized, and the energy of each of these vibrations is quantized according to the relation<sup>13</sup> (Equation 2.13):

$$E_v = hv(v + 1/2) \quad (2.13)$$

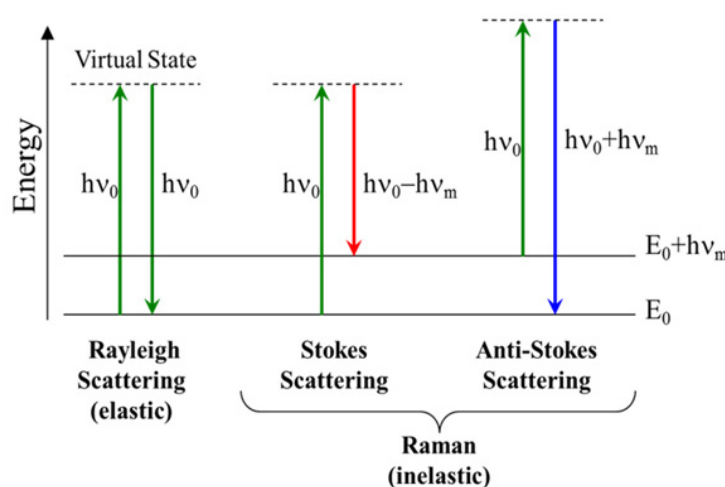


Figure 2.25: Idealised model of Rayleigh scattering and Stokes and anti-Stokes Raman scattering.<sup>23</sup>

Raman Stokes scattering is usually the one that is commonly studied and implied in Raman spectroscopy<sup>13</sup> because although the anti-Stokes and Stokes lines give the same information, the Stokes lines are stronger<sup>84</sup> and an anti-Stokes transition is very unlikely at room temperature<sup>13</sup>. The typical Stokes and anti-Stokes scattering spectrum is separated by the Rayleigh scattering line, which is expected to be off-scale near the point of no energy shift<sup>85</sup>.

The typical Raman patterns of Eu-doped HA for the co-precipitated and hydrothermal methods can be observed in figure 2.26. Since in the present work the method used in the synthesis of europium-doped hydroxyapatite was the hydrothermal method, the results expected to be obtained are strong Raman peak located at about  $\sim 962\text{cm}^{-1}$  and  $\sim 433\text{cm}^{-1}$  associated with the symmetric stretching mode  $\nu_1$  of  $\text{PO}_4^{3-}$  and bending mode  $\nu_2$  of  $\text{PO}_4^{3-}$ , respectively, with an additional peak at  $1054\text{cm}^{-1}$  associated with the antisymmetric stretching mode  $\nu_3$  of  $\text{PO}_4^{3-}$  ion<sup>24</sup>.

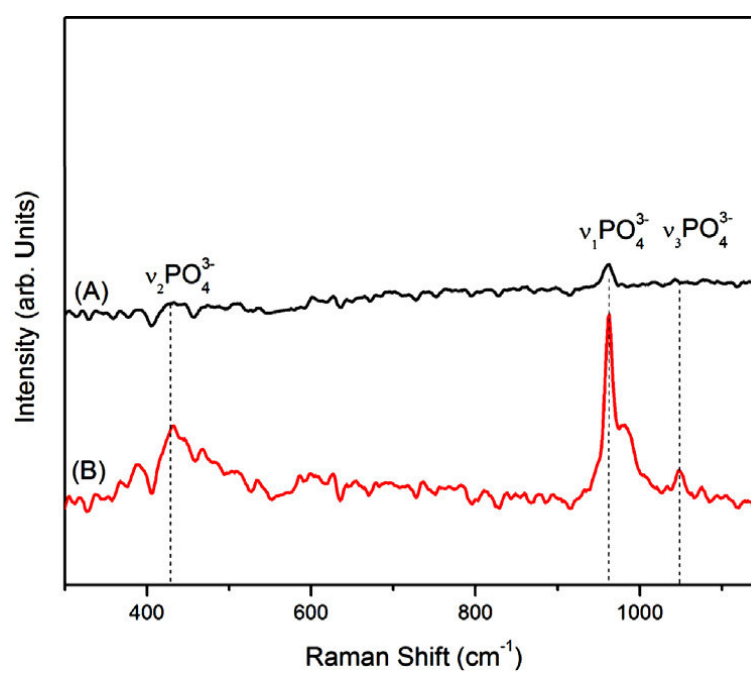


Figure 2.26: Eu-doped Hydroxyapatite Raman spectra (A) co-precipitation, (B) hydrothermal method.<sup>24</sup>



# Chapter 3

## Methodology

### 3.0.1 Chemicals

For the synthesis of hydroxyapatite the main reagents used were calcium chloride ( $\text{CaCl}_2$ ), ammonium dihydrogen phosphate  $(\text{NH}_4)_2\text{H}_2\text{PO}_4$ , hydrochloric acid (HCl) and ammonium hydroxide ( $\text{NH}_4\text{OH}$ ). For the substitution of calcium by europium atoms, Europium (III) nitrate pentahydrate ( $\text{EuN}_3\text{O}_9$ ), 99.9% trace metals basis, which was obtained from Sigma-Aldrich.

### 3.0.2 Synthesis

The hydrothermal method was used for the synthesis of pure hydroxyapatite. For the synthesis, 10 mmol of  $\text{CaCl}_2$ , exactly 1.1193 g, was weighed since the optimal calcium to phosphate ratio used is  $\text{Ca/P} = 1.67$ , 5.998 mmol of  $(\text{NH}_4)_2\text{H}_2\text{PO}_4$ , exactly 0.6724 g, was weighed against maintaining this ratio, both reagents were diluted in 25 mL of distilled water and set aside. Then, the  $(\text{NH}_4)_2\text{H}_2\text{PO}_4$  and distilled water solution was placed on a magnetic stirrer without increasing the temperature, and the  $\text{CaCl}_2$  and distilled water solution was added dropwise using a burette (Figure 3.1 a). Once both solutions were mixed, an initial pH of 5 was obtained, and after adding 5 mL of ammonium hydroxide, a final pH of 10 was obtained. Finally, the resulting solution was mounted in a reactor at  $125^\circ\text{C}$  for 24 hours to produce hydroxyapatite (Figure 3.1 c). Then, the sample obtained was divided into five parts, four parts were calcined at different temperatures,  $200^\circ\text{C}$ ,  $450^\circ\text{C}$ ,  $600^\circ\text{C}$ , and  $800^\circ\text{C}$ , and one part was kept at room temperature, this being the last stage of the synthesis.

Furthermore, the hydrothermal method was used to synthesize hydroxyapatite substitute with europium atoms. To maintain the previously mentioned ratio of calcium and phosphate, but this time adding europium, it is found that  $(\text{Ca}+\text{Eu})/\text{P}=1.67$ . This ratio was maintained for different europium concentrations from 0-20(%). As a result, the new ratio of hydroxyapatite with europium atom substitution is given by,  $\text{Ca}_{10-x}\text{Eu}_x(\text{PO}_4)_6(\text{OH})_2$  were ( $0 \leq x \leq 0.2$ ).  $\text{CaCl}_2$  and  $\text{EuN}_3\text{O}_9$  were weighed and diluted in 25 mL of distilled water; these grams varied depending on the

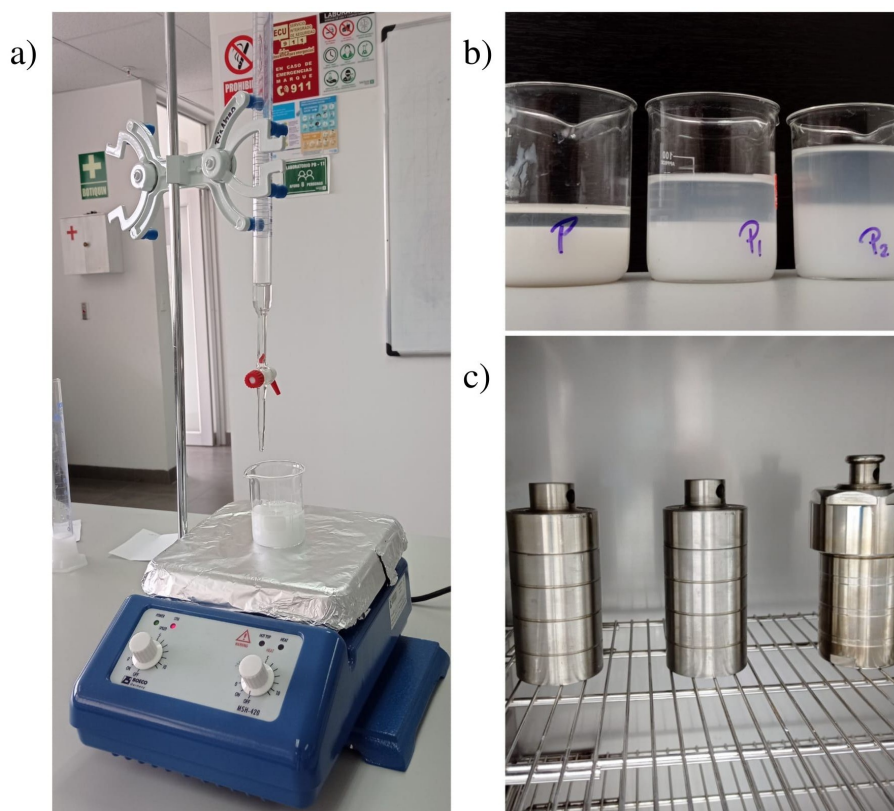


Figure 3.1: a) Synthesis of europium-doped hydroxyapatite. b) Hydroxyapatite synthesis for different europium concentrations, P=20%-Eu, P<sub>1</sub>=15%-Eu and P<sub>2</sub>=10%-Eu. c) Resulting solution mounted in a reactor at 125°C for 24 hours to produce hydroxyapatite.

percentage concentration of europium required, which is shown in table 3.1. Then, the experiment was performed precisely as it was done with pure hydroxyapatite, so 5.998 mmol of  $(\text{NH}_4)_2\text{H}_2\text{PO}_4$  was weighed (Table 3.1). The calcium and europium solution was added dropwise to the phosphate solution, again using the burette and magnetic stirrer (Figure 3.1 a). Once both solutions were mixed, an initial pH of 5 was obtained, and after adding 5 mL of ammonium hydroxide, a final pH of 11 was obtained. To obtain a pH of 10, 17 drops of pure HCl were added. Finally, the resulting solution was mounted in a reactor at 125°C for 24 hours to produce europium-substitute hydroxyapatite (Figure 3.1 b and c). Then, the sample obtained was divided into five parts, four parts were calcined at different temperatures, 200 °C, 450 °C, 600 °C, and 800 °C, and one part was kept at room temperature, this being the last stage of the synthesis. Finally, to facilitate the measurements, tablets were made for each of the concentrations and each of the temperatures (Figure 3.2).

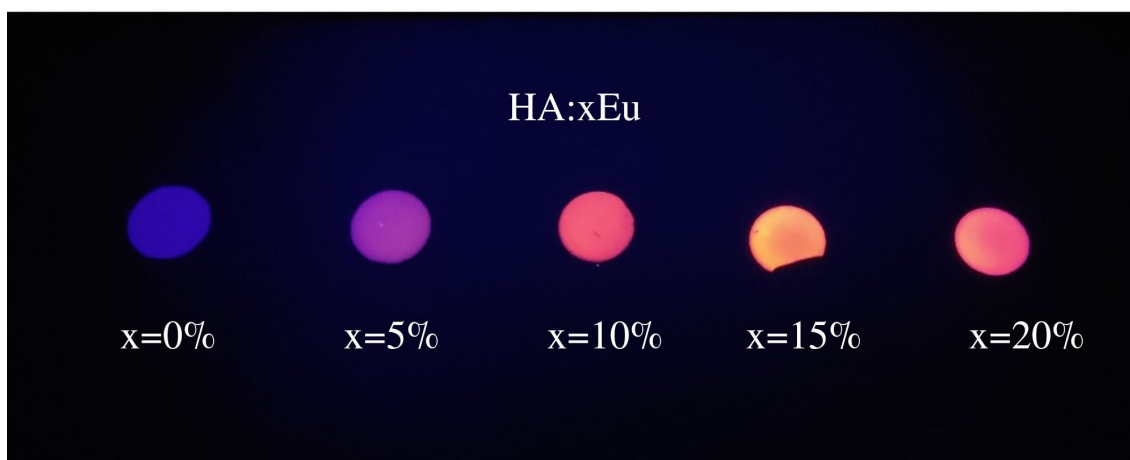


Figure 3.2: HA:xEu tablets for  $x=0\%$ ,  $5\%$ ,  $10\%$ ,  $15\%$ , and  $20\%$ , calcined at  $800\text{ }^{\circ}\text{C}$  under a UV lamp ( $365\text{ nm}$ ).

$x(\%)$	Eu (mmol)	Eu (g)	Ca (mmol)	Ca (g)	P (mmol)	P (g)
0	0	0	10	1.1193	5.998	0.6724
5	0.5	0.2172	9.5	0.8956	5.998	0.6929
10	1	0.4275	9	0.6820	5.998	0.6888
15	1.5	0.6451	8.5	0.4651	5.998	0.6851
20	2	0.8564	8	0.2551	5.998	0.6921

Table 3.1: Reagent quantities used for the hydrothermal synthesis of HA:xEu for  $x=0\%$ ,  $5\%$ ,  $10\%$ ,  $15\%$ , and  $20\%$ .

### 3.0.3 Characterization Equipment

#### X-ray diffraction

An X-ray diffractometer for polycrystalline sample, Rigaku, MiniFlex. This equipment was used for XRD measurements, equipped with a 600W X-ray tube, Bragg-Brentano goniometer with 8-position autosampler, D/teX Ultra detector, SmartLab Studio II software (Figure 3.3). Measurements were performed for HA:xEu with  $x=0\%$ ,  $5\%$ ,  $10\%$ ,  $15\%$ , and  $20\%$ , each concentration at five different temperatures, ambient,  $200\text{ }^{\circ}\text{C}$ ,  $450\text{ }^{\circ}\text{C}$ ,  $600\text{ }^{\circ}\text{C}$ , and  $800\text{ }^{\circ}\text{C}$ .

#### Fourier-transform infrared spectroscopy

To obtain our transmittance versus wavenumber spectrum, it was used the Fourier-transform infrared spectrometer Agilent Cary 630 FTIR (Figure 3.4). Measurements were performed for HA:xEu with  $x=0\%$ ,  $5\%$ ,  $10\%$ ,  $15\%$ , and  $20\%$ , each concentration at five different temperatures, ambient,  $200\text{ }^{\circ}\text{C}$ ,  $450\text{ }^{\circ}\text{C}$ ,  $600\text{ }^{\circ}\text{C}$ , and  $800\text{ }^{\circ}\text{C}$ .



Figure 3.3: An X-ray diffractometer Rigaku, MiniFlex.



Figure 3.4: Fourier-transform infrared spectrometer Agilent Cary 630 FTIR.

### Scanning Electron Microscopy

To obtain the micrographs, it was used the Phenom ProX Desktop Scanning Electron Microscope (Figure 3.5). Measurements were performed for HA:xEu with  $x=0\%$ , 5%, 10%, 15%, and 20%, each concentration at five different

temperatures, ambient, 200 °C, 450 °C, 600 °C, and 800 °C.



Figure 3.5: Phenom ProX Desktop Scanning Electron Microscope.

### Raman Spectroscopy

LabRAM HR Evolution Raman microscope from HORIBA France SAS (Figure 3.6) was used to obtain our Raman spectra. Measurements were performed for HA:xEu with  $x=0\%$ , 5%, 10%, 15%, and 20%, each concentration at five different temperatures, ambient, 200 °C, 450 °C, 600 °C, and 800 °C.

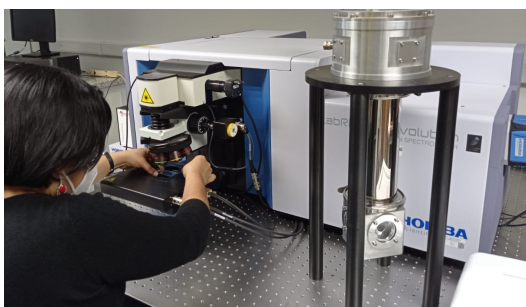


Figure 3.6: LabRAM HR Evolution Raman microscopes from HORIBA France SAS.

### Luminescence Spectroscopy

Photoluminescence measurements were performed using an emission monochromator (MicroHR, Horiba) and, a solid-state detector (Si/InGaAs, Horiba) from the optics laboratory of the Pontificia Universidad Católica del Ecuador, Quito. A pair of lenses aligned with the optical axis of the detection system was used for light collection (Figure 3.7). Photoluminescence spectra were recorded after the excitation of the samples with a 405 nm diode laser. Measurements were performed for HA:xEu with  $x=0\%$ , 5%, 10%, 15%, and 20%, each concentration at five different temperatures, ambient, 200 °C, 450 °C, 600 °C, and 800 °C.

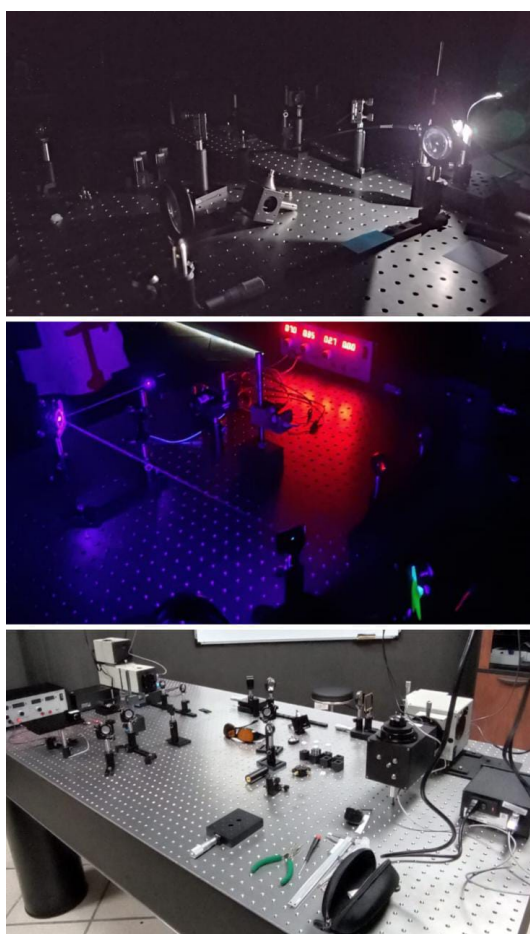


Figure 3.7: Optical path produced to study the photoluminescence of the samples with a 405 nm incident laser, for this purpose photoluminescence spectroscopy was employed using an emission monochromator (MicroHR, Horiba) coupled to a solid state detector (Si/InGaAs, Horiba).

# Chapter 4

## Results & Discussion

### 4.1 Morphological and Structural Characterization

#### 4.1.1 Fourier-transform infrared spectroscopy

Fourier transform infrared (FTIR) spectroscopy was used to analyze the corresponding changes of the functional groups in the structures of Ha:xEu, the spectra were collected in the wavenumber range 400-4000  $\text{cm}^{-1}$  as shown in figures (4.1) for ambient temperature, (4.2) for 200 °C, (4.3) for 450 °C, (4.4) for 600 °C, and (4.5) for 800 °C. The interpretation of the spectra FTIR for x= 0%, 5%, 10%, 15%, and 20%, at ambient temperature, 200 °C, 450 °C, 600 °C, and 800 °C, are explained in the tables (4.1), (4.1), (4.1), (4.1), and (4.1), respectively. These tables shows the formation of hydroxyapatite by the presence of its characteristic bands.

#### FTIR analysis for HA:xEu at ambient temperature

The characteristic bands of hydroxyapatite obtained are the doubly degenerate bending mode of the phosphate group,  $\nu_2(\text{PO}_4)^{3-}$ , assigned to the 474  $\text{cm}^{-1}$  peak. The triple-degenerate bending mode of the O-P-O bond,  $\nu_4(\text{PO}_4)^{3-}$ , is observed at the 560  $\text{cm}^{-1}$  and 607  $\text{cm}^{-1}$  peaks. The symmetric stretching,  $\nu_1(\text{PO}_4)^{3-}$ , attributed to the peak at wavenumber 996  $\text{cm}^{-1}$  for x=20% and, 1023  $\text{cm}^{-1}$  for x=0%, 5%, 10% and 15%. The triple-degenerate antisymmetric stretching mode of the phosphate group,  $\nu_3(\text{PO}_4)^{3-}$ , assigned to the peak at 1089  $\text{cm}^{-1}$ . Furthermore, the presence of the hydrogen phosphate group ( $\text{HPO}_4^{2-}$ ) at 530  $\text{cm}^{-1}$ , 534  $\text{cm}^{-1}$ , 537  $\text{cm}^{-1}$  and 873  $\text{cm}^{-1}$ , and 3570  $\text{cm}^{-1}$  the stretching mode,  $\nu_s(\text{OH})^-$ .

Finally, the presence of  $\text{CO}_2$  is observed at the peak at 1428  $\text{cm}^{-1}$ , and some peaks indicate the presence of adsorbed water, which are 1621  $\text{cm}^{-1}$  ( $\text{H}_2\text{O}$ ) and the broadband between 3000  $\text{cm}^{-1}$  - 3600  $\text{cm}^{-1}$  (H-O-H bond bending,  $\text{delta}(\text{H}_2\text{O})$ ). On the other hand, as the concentration of europium increases, some functional groups

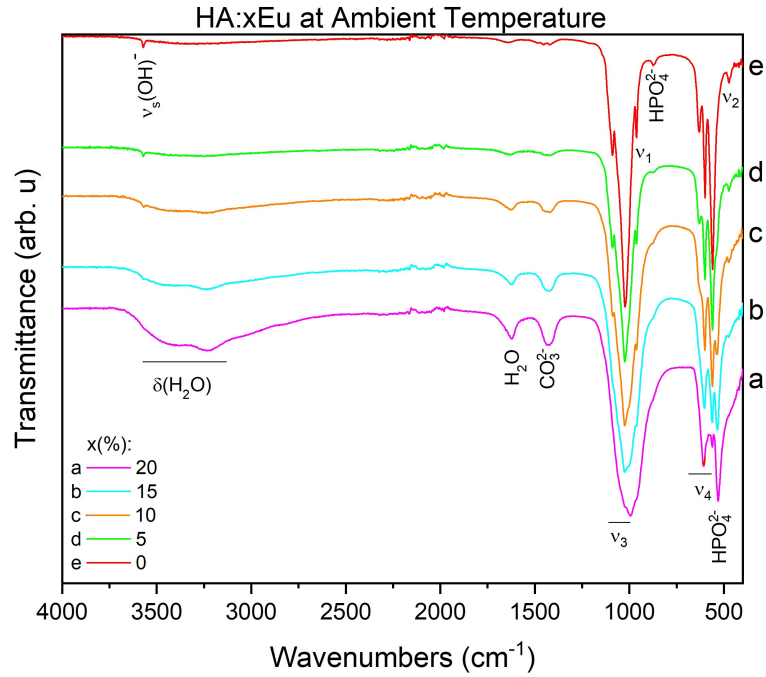


Figure 4.1: FTIR spectrum for HA:xEu at ambient temperature, for x=0%, 5%, 10%, 15%, and 20%

Assignment	Wavenumbers (cm <sup>-1</sup> )					References
	x= 20%	x= 15%	x= 10%	x= 5%	x= 0%	
$\nu_2(\text{PO}_4)^{3-}$	0	474	474	474	474	41, 86, 87
$\text{HPO}_4^{2-}$	530	534	537	0	0	88
$\nu_4(\text{PO}_4)^{3-}$	560	560	560	560	561	41, 86, 88
$\nu_4(\text{PO}_4)^{3-}$	607	600	600	600	600	41, 86, 88
$\text{HPO}_4^{2-}$	0	0	0	873	873	86
$\nu_1(\text{PO}_4)^{3-}$	0	0	959	959	959	41, 86, 87
$\nu_3(\text{PO}_4)^{3-}$	996	1023	1023	1023	1023	41, 86, 87, 88
$\nu_3(\text{PO}_4)^{3-}$	0	0	1089	1089	1089	41, 86, 87, 88
$\text{CO}_3^{2-}$	1428	1428	1428	0	0	89
$\text{H}_2\text{O}$	1621	1621	1621	0	0	89
$\nu_s(\text{OH})^-$	0	0	3570	3570	3570	86, 87, 88
$\delta(\text{H}_2\text{O})$	3000-3600	3000-3600	3000-3600	0	0	86

Table 4.1: Measured absorption features in the FTIR spectra and relative assignments for HA:xEu at Ambient Temperature, for x= 0%, 5%, 10%, 15%, and 20%.

disappear, and others appear. The functional groups  $\nu_2(\text{PO}_4)^{3-}$  at  $474\text{ cm}^{-1}$ ,  $\text{HPO}_4^{2-}$  at  $873\text{ cm}^{-1}$ ,  $\nu_1(\text{PO}_4)^{3-}$  at  $959\text{ cm}^{-1}$  and  $\nu_s(\text{OH})^-$  at  $3570\text{ cm}^{-1}$  disappear, the peaks of  $534\text{ cm}^{-1}$  ( $\text{HPO}_4^{2-}$ ),  $1428\text{ cm}^{-1}$  ( $\text{CO}_2$ ),  $1621\text{ cm}^{-1}$  ( $\text{H}_2\text{O}$ ) and  $300\text{-}3600\text{ cm}^{-1}$  ( $\delta(\text{H}_2\text{O})$ ) appear and the rest persist.

#### FTIR analysis for HA:xEu at 200 °C

The hydroxyapatite characteristic bands obtained are the doubly degenerate bending mode of the phosphate group,  $\nu_2(\text{PO}_4)^{3-}$ , assigned to the  $474\text{ cm}^{-1}$  peak. The triple-degenerate bending mode of the O-P-O bond,  $\nu_4(\text{PO}_4)^{3-}$ , seen in the  $560\text{ cm}^{-1}$ ,  $561\text{ cm}^{-1}$ ,  $599\text{ cm}^{-1}$ ,  $600\text{ cm}^{-1}$  and  $604\text{ cm}^{-1}$  peaks. The symmetric stretching,  $\nu_1(\text{PO}_4)^{3-}$ , attributed to the peak at the wavenumber  $958\text{ cm}^{-1}$  for  $x=15\%$  and  $962\text{ cm}^{-1}$  for  $x=0\%$ ,  $5\%$  and  $10\%$ . The antisymmetric triple-degenerate stretching mode of the phosphate group,  $\nu_3(\text{PO}_4)^{3-}$ , assigned to the wavenumbers between  $(1022\text{-}1025)\text{ cm}^{-1}$  and, also to  $1087\text{ cm}^{-1}$  and  $1089\text{ cm}^{-1}$ . In addition, the presence of the hydrogen phosphate group ( $\text{HPO}_4^{2-}$ ) at  $527\text{ cm}^{-1}$  and  $536\text{ cm}^{-1}$ , and the stretching modes,  $\nu_L(\text{OH})^-$  ( $630\text{ cm}^{-1}$ ) and  $\nu_s(\text{OH})^-$  ( $3570\text{ cm}^{-1}$ ).

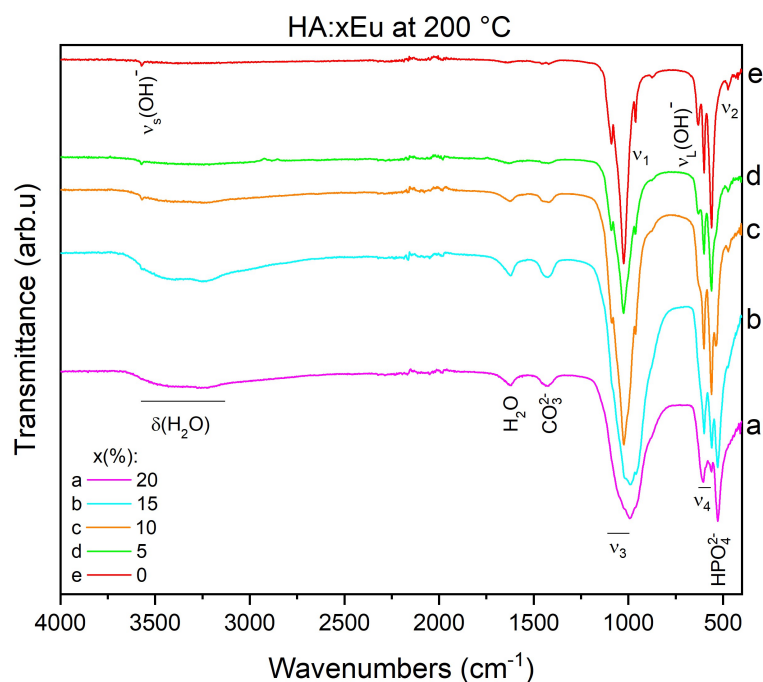


Figure 4.2: FTIR spectrum for Ha:xEu at 200 °C, for  $x=0\%$ ,  $5\%$ ,  $10\%$ ,  $15\%$ , and  $20\%$

Finally, the presence of  $\text{CO}_2$  is observed at  $1428\text{ cm}^{-1}$  peak, and the peak at  $1621\text{ cm}^{-1}$  ( $\text{H}_2\text{O}$ ) indicates the presence of absorbed water. On the other hand, as the concentration of europium increases, some functional groups disappear, and others appear. The functional groups  $\nu_2(\text{PO}_4)^{3-}$  at  $474\text{ cm}^{-1}$ ,  $\nu_L(\text{OH})^-$  at  $630\text{ cm}^{-1}$ ,  $\nu_1(\text{PO}_4)^{3-}$  at

Assignment	Wavenumbers (cm <sup>-1</sup> )					References
	x= 20%	x= 15%	x= 10%	x= 5%	x= 0%	
$\nu_2(\text{PO}_4)^{3-}$	0	0	474	474	474	41, 86, 87
$\text{HPO}_4^{2-}$	527	527	536	0	0	88
$\nu_4(\text{PO}_4)^{3-}$	561	560	561	561	561	41, 86, 88
$\nu_4(\text{PO}_4)^{3-}$	604	599	600	600	600	41, 86, 88
$\nu_L(\text{OH})^-$	0	0	0	630	630	86
$\nu_1(\text{PO}_4)^{3-}$	0	958	962	962	962	41, 86, 87
$\nu_3(\text{PO}_4)^{3-}$	1023	1022	1024	1025	1025	41, 86, 87, 88
$\nu_3(\text{PO}_4)^{3-}$	0	0	1087	1089	1089	41, 86, 87, 88
$\text{CO}_3^{2-}$	1429	1429	1429	0	0	89
$\text{H}_2\text{O}$	1621	1621	1621	0	0	89
$\nu_s(\text{OH})^-$	0	0	3570	3570	3570	86, 87, 88
$\delta(\text{H}_2\text{O})$	3000-3600	3000-3600	3000-3600	0	0	86

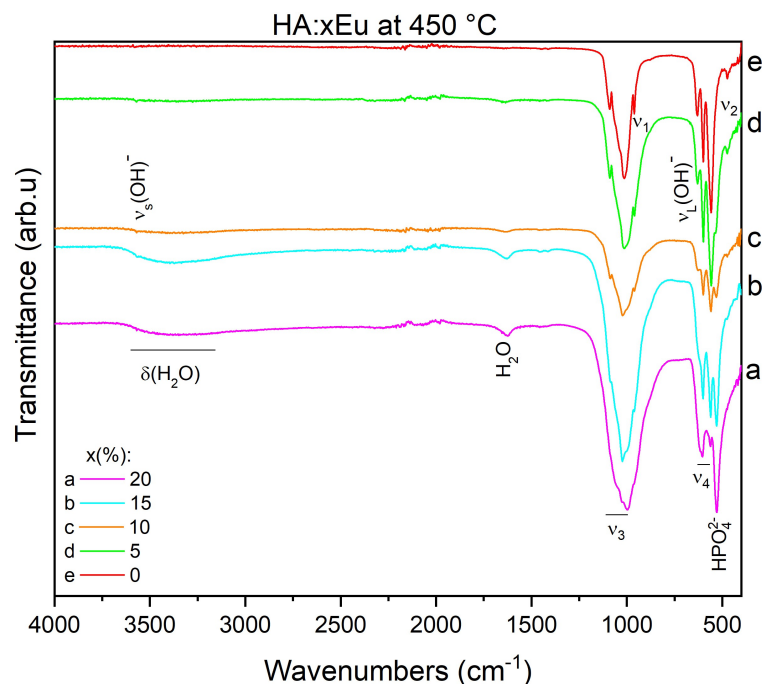
Table 4.2: Measured absorption features in the FTIR spectra and relative assignments for HA:xEu at 200 °C, for x=0%, 5%, 10%, 15%, and 20%

$\sim 962 \text{ cm}^{-1}$  and  $\nu_3(\text{PO}_4)^{3-}$  at  $1087 \text{ cm}^{-1}$  disappear, the peaks at  $\sim 527 \text{ cm}^{-1}$  ( $\text{HPO}_4^{2-}$ ),  $1429 \text{ cm}^{-1}$  ( $\text{CO}_2$ ),  $1621 \text{ cm}^{-1}$  ( $\text{H}_2\text{O}$ ) appear and the others ones persist.

#### FTIR analysis for HA:xEu at 450 °C

The hydroxyapatite characteristic bands obtained are the doubly degenerate bending mode of the phosphate group,  $\nu_2(\text{PO}_4)^{3-}$ , assigned to the  $473 \text{ cm}^{-1}$  peak. The triple-degenerate bending mode of the O-P-O bond,  $\nu_4(\text{PO}_4)^{3-}$ , seen in the  $560 \text{ cm}^{-1}$ ,  $561 \text{ cm}^{-1}$ ,  $598 \text{ cm}^{-1}$ ,  $600 \text{ cm}^{-1}$ ,  $601 \text{ cm}^{-1}$  and  $604 \text{ cm}^{-1}$  peaks. The symmetric stretching,  $\nu_1(\text{PO}_4)^{3-}$ , attributed to the peak at the wavenumber  $998 \text{ cm}^{-1}$  for x=20% and,  $961 \text{ cm}^{-1}$  for x=0%, 5%, 10% and 15%. The antisymmetric triple-degenerate stretching mode of the phosphate group,  $\nu_3(\text{PO}_4)^{3-}$ , assigned to the peaks at the wavenumbers  $1015 \text{ cm}^{-1}$ ,  $1022 \text{ cm}^{-1}$ ,  $1024 \text{ cm}^{-1}$ ,  $1025 \text{ cm}^{-1}$ ,  $1087 \text{ cm}^{-1}$  and  $1090 \text{ cm}^{-1}$ . In addition, the presence of the hydrogen phosphate group ( $\text{HPO}_4^{2-}$ ) at  $528 \text{ cm}^{-1}$ ,  $530 \text{ cm}^{-1}$  and  $532 \text{ cm}^{-1}$ , and the stretching modes,  $\nu_L(\text{OH})^-$  ( $629 \text{ cm}^{-1}$  and  $633 \text{ cm}^{-1}$ ) and  $\nu_s(\text{OH})^-$  ( $3570 \text{ cm}^{-1}$ ).

Finally, some peaks indicate the presence of absorbed water, which are  $1626 \text{ cm}^{-1}$  and  $1630 \text{ cm}^{-1}$  for  $\text{H}_2\text{O}$ , and the broadband between  $3000 \text{ cm}^{-1}$ - $3600 \text{ cm}^{-1}$  (H-O-H bond bending,  $\delta(\text{H}_2\text{O})$ ). On the other hand, as the concentration of europium increases, some peaks disappear, and others appear. The peaks assigned to  $\nu_2(\text{PO}_4)^{3-}$ ,  $\nu_L(\text{OH})^-$  and,  $\nu_3(\text{PO}_4)^{3-}$  at  $1087 \text{ cm}^{-1}$  and  $1090 \text{ cm}^{-1}$  disappear, the peaks assigned to  $\text{HPO}_4^{2-}$ ,  $\text{H}_2\text{O}$  and  $\delta(\text{H}_2\text{O})$  appear, and the others functional groups peaks persist.

Figure 4.3: FTIR spectrum for Ha:xEu at 450 °C, for  $x=0\%$ , 5%, 10%, 15%, and 20%

Assignment	Wavenumbers (cm <sup>-1</sup> )					References
	$x=20\%$	$x=15\%$	$x=10\%$	$x=5\%$	$x=0\%$	
$\nu_2(\text{PO}_4)^{3-}$	0	0	473	473	473	41, 86, 87
$\text{HPO}_4^{2-}$	530	528	532	0	0	88
$\nu_4(\text{PO}_4)^{3-}$	561	561	560	560	560	41, 86, 88
$\nu_4(\text{PO}_4)^{3-}$	604	600	601	598	601	41, 86, 87
$\nu_L(\text{OH})^-$	0	0	629	629	633	86
$\nu_1(\text{PO}_4)^{3-}$	998	961	961	961	961	41, 86, 87
$\nu_3(\text{PO}_4)^{3-}$	1025	1024	1022	1015	1015	41, 86, 87, 88
$\nu_3(\text{PO}_4)^{3-}$	0	1087	1087	1090	1090	41, 86, 87, 88
$\text{H}_2\text{O}$	1626	1630	0	0	0	89
$\nu_s(\text{OH})^-$	0	0	3570	3570	3570	86, 87, 88
$\delta(\text{H}_2\text{O})$	3000-3600	3000-3600	3000-3600	0	0	86

Table 4.3: Measured absorption features in the FTIR spectra and relative assignments for HA:xEu at 450 °C, for  $x=0\%$ , 5%, 10%, 15%, and 20%.

### FTIR analysis for HA:xEu at 600 °C

The hydroxyapatite characteristic bands obtained are the doubly degenerate bending mode of the phosphate group,  $\nu_2(\text{PO}_4)^{3-}$ , assigned to the 472  $\text{cm}^{-1}$  and 477  $\text{cm}^{-1}$  peaks. The triple-degenerate bending mode of the O-P-O bond,  $\nu_4(\text{PO}_4)^{3-}$ , observed in the 558  $\text{cm}^{-1}$ , 560  $\text{cm}^{-1}$ , 564  $\text{cm}^{-1}$ , 600  $\text{cm}^{-1}$  and 602  $\text{cm}^{-1}$  peaks. The symmetric stretching,  $\nu_1(\text{PO}_4)^{3-}$ , assigned to the peak at the wavenumber 962  $\text{cm}^{-1}$  for  $x=0\%$  and, 960  $\text{cm}^{-1}$  for  $x=5\%$  and 10%. The antisymmetric triple-degenerate stretching mode of the phosphate group,  $\nu_3(\text{PO}_4)^{3-}$ , attributed to the peaks at the wavenumbers 1017  $\text{cm}^{-1}$ , 1024  $\text{cm}^{-1}$ , 1087  $\text{cm}^{-1}$  and 1088  $\text{cm}^{-1}$ . In addition, the presence of the hydrogen phosphate group ( $\text{HPO}_4^{2-}$ ) at 522  $\text{cm}^{-1}$ , 524  $\text{cm}^{-1}$  and 522  $\text{cm}^{-1}$ . Finally, at 629  $\text{cm}^{-1}$  and 631  $\text{cm}^{-1}$  these peaks are assigned to stretching mode ( $\nu_L(\text{OH})^-$ ) and, 3571  $\text{cm}^{-1}$  and 3573  $\text{cm}^{-1}$  for  $\nu_s(\text{OH})^-$ .

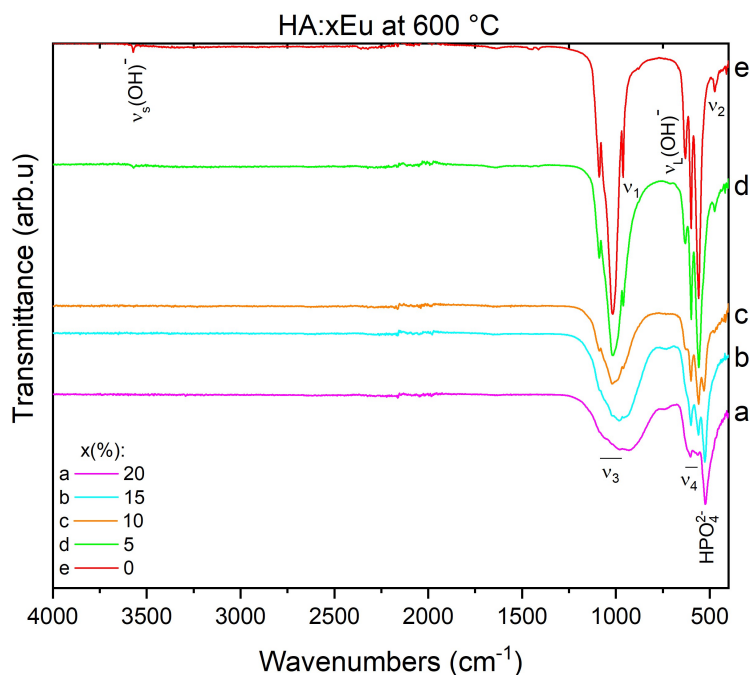


Figure 4.4: FTIR spectrum for Ha:xEu at 600 °C, for  $x=0\%$ , 5%, 10%, 15%, and 20%

On the other hand, as the concentration of europium increases, some peaks disappear, and others appear. The peaks assigned to  $\nu_2(\text{PO}_4)^{3-}$ ,  $\nu_L(\text{OH})^-$ ,  $\nu_1(\text{PO}_4)^{3-}$ ,  $\nu_3(\text{PO}_4)^{3-}$  and  $\nu_s(\text{OH})^-$  disappear, the peaks assigned to  $\text{HPO}_4^{2-}$  appear, and the others peaks of functional groups persist.

Assignment	Wavenumbers (cm <sup>-1</sup> )					References
	x= 20%	x= 15%	x= 10%	x= 5%	x= 0%	
$\nu_2(\text{PO}_4)^{3-}$	0	0	477	472	472	41, 86, 87
$\text{HPO}_4^{2-}$	522	524	530	0	0	88
$\nu_4(\text{PO}_4)^{3-}$	564	560	560	558	560	41, 86, 88
$\nu_4(\text{PO}_4)^{3-}$	602	600	602	600	600	41, 86, 88
$\nu_L(\text{OH})^-$	0	0	629	629	631	86
$\nu_1(\text{PO}_4)^{3-}$	0	0	960	960	962	41, 86, 87
$\nu_3(\text{PO}_4)^{3-}$	0	0	1024	1017	1017	41, 86, 87, 88
$\nu_3(\text{PO}_4)^{3-}$	0	0	1087	1088	1088	41, 86, 87, 88
$\nu_s(\text{OH})^-$	0	0	0	3571	3573	86, 87, 88

Table 4.4: Measured absorption features in the FTIR spectra and relative assignments for HA:xEu at 600 °C, for x=0%, 5%, 10%, 15%, and 20%.

#### FTIR analysis for HA:xEu at 800 °C

The hydroxyapatite characteristic bands obtained are the doubly degenerate bending mode of the phosphate group,  $\nu_2(\text{PO}_4)^{3-}$ , attributed to the 474 cm<sup>-1</sup> peak. The triple-degenerate bending mode of the O-P-O bond,  $\nu_4(\text{PO}_4)^{3-}$ , seen in the peaks between 584 cm<sup>-1</sup> and 621 cm<sup>-1</sup>. The symmetric stretching,  $\nu_1(\text{PO}_4)^{3-}$ , assigned to the peak at the wavenumber 957 cm<sup>-1</sup> for x=15% and 20%, and 961 cm<sup>-1</sup>, 962 cm<sup>-1</sup> and 958 cm<sup>-1</sup> for x=0%, 5% and 10% respectively. The antisymmetric triple-degenerate stretching modes of the phosphate group peaks,  $\nu_3(\text{PO}_4)^{3-}$ , are observed at the wavenumbers range between 990 cm<sup>-1</sup> and 1098 cm<sup>-1</sup>. In addition, the presence of the hydrogen phosphate group ( $\text{HPO}_4^{2-}$ ) between 532 cm<sup>-1</sup> and 560 cm<sup>-1</sup>. Finally, the peak at 1213 cm<sup>-1</sup> is attributed to P=O stretch vibration mode and PO<sub>2</sub> asymmetrical stretch, and the peak at 727 cm<sup>-1</sup> to P-O-P symmetrical stretch mode.

On the other hand, as the concentration of europium increases, some functional groups disappear, and others appear. The peaks assigned to  $\nu_2(\text{PO}_4)^{3-}$ ,  $\nu_4(\text{PO}_4)^{3-}$  at 597 cm<sup>-1</sup> and,  $\nu_3(\text{PO}_4)^{3-}$  at 1088 cm<sup>-1</sup> and 1098 cm<sup>-1</sup> disappear, the peaks assigned to  $\nu_4(\text{PO}_4)^{3-}$ ,  $\nu_s(\text{P-O-P})$  and  $\nu(\text{P=O}) - \nu_{as}(\text{PO}_2)$  appear, and the others ones persist.

#### Analysis and comparison of the FTIR results.

At ambient temperature and for x=10%, it is observed that the peaks of  $\nu_1$ ,  $\nu_2$ , and  $\nu_3$ , although they are still in the same wavenumber characteristic of HA, their transmittance decreases, i.e., smaller peaks are found. In addition, peak appears at ~534 cm<sup>-1</sup> ( $\text{HPO}_4^{2-}$ ), ~1428 cm<sup>-1</sup> (CO<sub>2</sub>), ~1621 cm<sup>-1</sup> (H<sub>2</sub>O) and ~(300-3600) cm<sup>-1</sup> ( $\delta(\text{H}_2\text{O})$ ). Finally, the presence of the characteristic HA peak,  $\nu_s(\text{OH})^-$  at ~3570 cm<sup>-1</sup> is observed until this concentration. These changes are clearly indicative that from 10%, the hydroxyapatite may have changed to another phase.

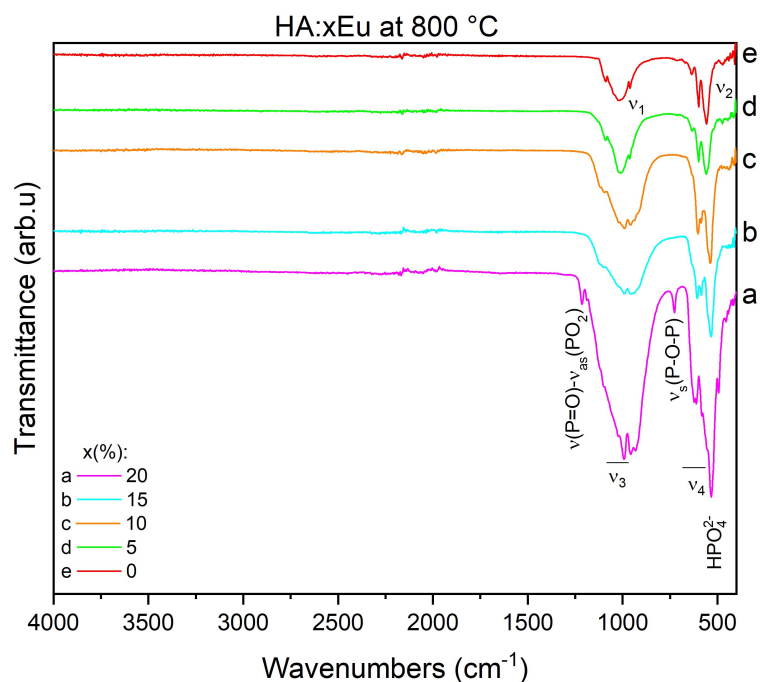


Figure 4.5: FTIR spectrum for Ha:xEu at 800 °C, for  $x=0\%$ ,  $5\%$ ,  $10\%$ ,  $15\%$ , and  $20\%$ .

Assignment	Wavenumbers ( $\text{cm}^{-1}$ )					References
	$x=20\%$	$x=15\%$	$x=10\%$	$x=5\%$	$x=0\%$	
$\nu_2(\text{PO}_4)^{3-}$	0	0	0	474	474	41, 86, 87
$\text{HPO}_4^{2-}$	534	532	537	560	558	88
$\nu_4(\text{PO}_4)^{3-}$	0	0	0	597	597	41, 86, 88
$\nu_4(\text{PO}_4)^{3-}$	584	584	586	0	0	41, 86, 88
$\nu_4(\text{PO}_4)^{3-}$	611-621	604	603	0	0	41, 86, 88
$\nu_5(\text{P-O-P})$	727	0	0	0	0	90
$\nu_1(\text{PO}_4)^{3-}$	957	957	958	962	961	41, 86, 87
$\nu_3(\text{PO}_4)^{3-}$	992	990	990	1013	1025	41, 86, 87, 88
$\nu_3(\text{PO}_4)^{3-}$	0	0	1098	1088	1088	41, 86, 87, 88
$\nu(\text{P=O})-\nu_{as}(\text{PO}_2)$	1213	0	0	0	0	90

Table 4.5: Measured absorption features in the FTIR spectra and relative assignments for HA:xEu at 800 °C, for  $x=0\%$ ,  $5\%$ ,  $10\%$ ,  $15\%$ , and  $20\%$ .

These results in the peaks are maintained for 200 °C. For 450 °C the changes are maintained, with the difference that the peak of  $\text{CO}_2$  no appears anymore, and the peaks  $\text{H}_2\text{O}$  and  $(\delta(\text{H}_2\text{O}))$  are generated from 15%. At 600 °C,

very similar results are obtained as for the previous temperatures, but  $\text{CO}_2$ ,  $\text{H}_2\text{O}$ , ( $\delta(\text{H}_2\text{O})$ ), and  $\nu_s(\text{OH})^-$  peaks disappear almost completely. This change could be caused by drying due to the increase in temperature. For 800 °C the same changes mentioned for 600 °C are preserved but new peaks appear for 20%, such as  $\nu_4(\text{PO}_4)^{3-}$ ,  $\nu_s(\text{P}-\text{O}-\text{P})$ , and  $\nu(\text{P}=\text{O})-\nu_{as}(\text{PO}_2)$ . Finally, considering all these results, a strong indication is observed that from 10% europium concentration, europium-doped hydroxyapatite was transformed into europium-doped calcium phosphate. In addition, the new peaks of 20% at 800 °C suggest the possibility that another phosphate phase was generated.

Considering the FTIR HA:xEu graphs and tables, adsorbed water and carbonate groups are observed for different drying temperatures. This may be because, during hydroxyapatite synthesis, the initiation was in the aqueous phase and at room temperature. Probably, at drying temperatures below 200 °C, the water molecules remained adsorbed by physisorption or chemisorption; moreover, the presence of  $\text{CO}_3^{2-}$  may be the result of a transformation of atmospheric  $\text{CO}_2$  as it was adsorbed by the alkaline solution<sup>89</sup>. For this reason, carbonate ions in synthetic hydroxyapatite are known to be a typical impurity<sup>91,92</sup>. However, the presence of these peaks varies according to the drying temperature. First, it is observed that at room temperature and 200 °C, the graphs show a significant presence of peaks attributed to water and carbonate. Then, as the drying temperature increases, these peaks disappear; from 450 °C, the carbonate disappears, and from 600 °C, the water disappears completely.

#### 4.1.2 Scanning Electron Microscopy and EDX microanalysis

The surface morphology and chemical composition of HA:5%Eu and HA:20%Eu at 800 °C were investigated by SEM (4.6) and EDS techniques (4.7).

In the BSE imaging of Figure (4.6 a and b), it is observed that HA:xEu particles have similar sizes regardless of the europium concentration. The particle size ranges from 50 $\mu\text{m}$ -350 $\mu\text{m}$  for both HA:5%Eu and HA:20%Eu. Furthermore, the micrographs show that both concentrations have a regular morphology. Consequently, the microparticle size and regularity may be because, during the synthesis by the hydrothermal method, the solution was first treated at a pH of 10. Then, this solution was mounted in a reactor at 125 °C for 24h for all concentrations. As a result, it is known that as the pH decreases, more regular but smaller particles are obtained. However, the temperature applied to the reactor was not too high, and thus, excessively fast nucleation did not occur, obtaining regular microparticles.

On the other hand, the HA:5%Eu microparticles present superficial small bright spots that contrast with the opaque surface, and the HA:20%Eu microparticles present a homogeneous colored and slightly brighter surface. The bright spots in the figure (4.6 a) may correspond to the europium, since being images of backscattered electrons and the atomic number of europium being higher than that of the hydroxyapatite components, this would appear brighter. However, according to EDX of both concentrations (Figure 4.7), it is qualitatively observed that there is a higher concentration of europium in HA:20%Eu. Furthermore, quantitatively EDX indicated that the atomic

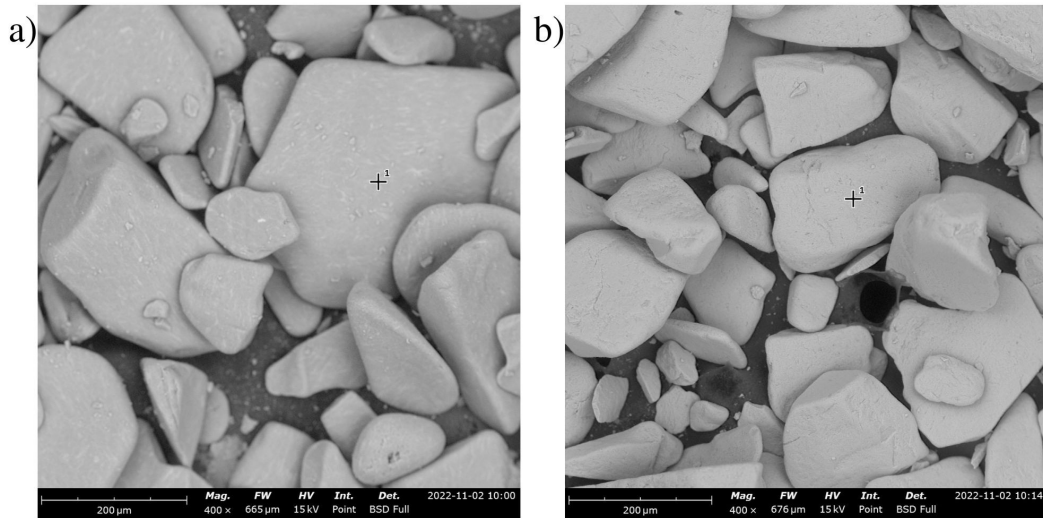


Figure 4.6: SEM micrographs. a) BSE image of HA:5%Eu, b) BSE images of HA:20%Eu.

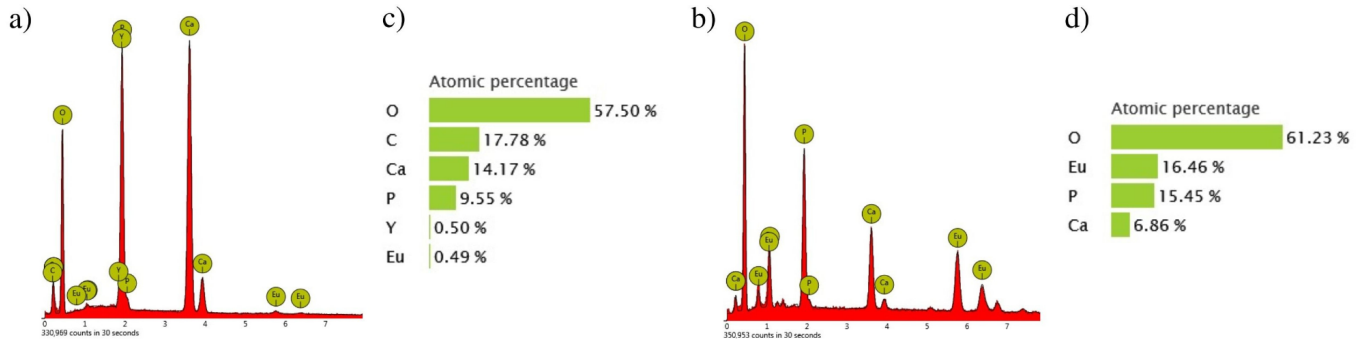


Figure 4.7: SEM micrographs. a) EDX spectrum of HA:5%Eu, b) EDX spectrum of HA:20%Eu, c) Atomic percentage of HA:5%Eu, d) Atomic percentage of HA:20%Eu.

percentage of HA:20%Eu is 16.46% europium, 15.45% phosphorus, and 6.86% calcium. Moreover, the atomic percentage of HA:5%Eu is 14.17% calcium, 9.55% phosphorus, and 0.49% europium.

Finally, comparing the EDX and BSE of HA:20%Eu, the homogeneous brightness and high concentration of europium may indicate the formation of new phases that have integrated Eu in the morphology. Likewise, comparing the EDX and BSE of HA:5%Eu, the bright lines and low concentration of europium may indicate that calcium was not substituted much by europium. Instead, europium mostly remained on the HA surface.

### 4.1.3 X-ray Diffraction

The crystal structure and phases of HA:xEu for  $x=0\%$ ,  $5\%$ ,  $10\%$ ,  $15\%$ , and  $20\%$  were examined using XRD analysis. Figures (4.8), (4.9), (4.10), (4.11), and (4.12) show the diffractogram for HA:xEu at room temperature,  $200\text{ }^\circ\text{C}$ ,  $450\text{ }^\circ\text{C}$ ,  $600\text{ }^\circ\text{C}$ , and  $800\text{ }^\circ\text{C}$ , respectively. Table (4.6) presents the Crystallography Open Database (COD) card, phase, space group, crystal structure, and cell parameters for each HA:xEu concentration and for all the temperatures.

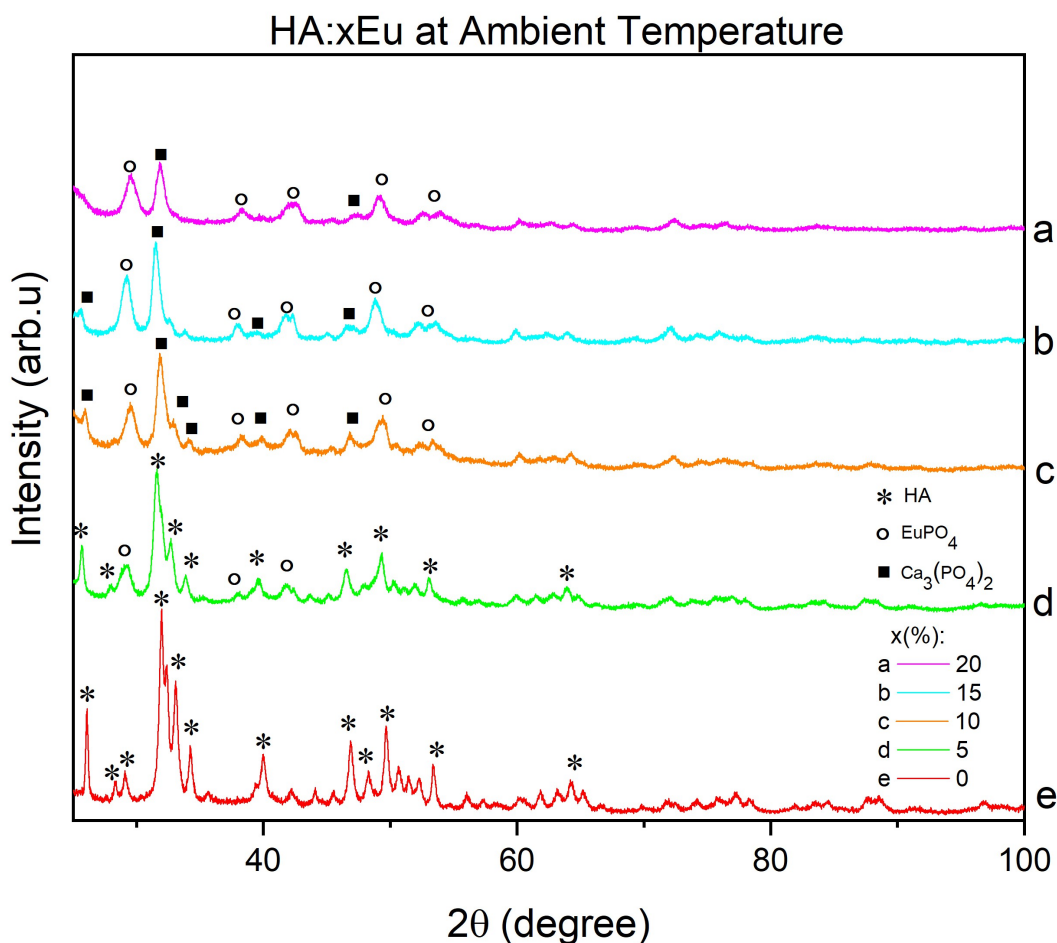


Figure 4.8: XRD Spectrum for Ha:xEu at ambient temperature, for  $x=5\%$ ,  $10\%$ ,  $15\%$ , and  $20\%$ .

HA:xEu diffractograms for all temperatures show the same results. The analysis of the  $x=0\%$  diffractogram shows that the best match is with COD card 9011093, which indicates the presence of the hydroxyapatite phase.

For  $x=5\%$ , the samples showed the best match with COD card 7038854 ( $\text{Ca}_{8.28}\text{La}_{1.72}\text{O}_{26}\text{P}_6$ ). Considering

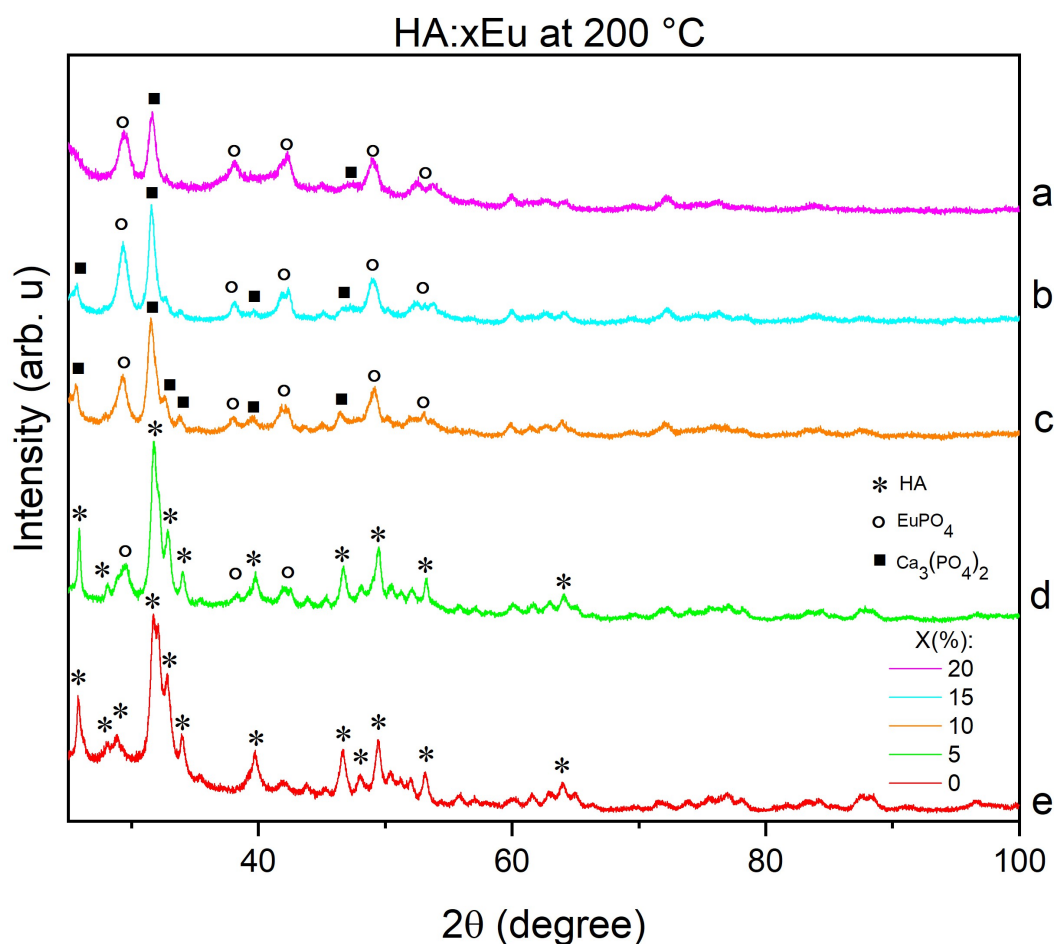


Figure 4.9: XRD Spectrum for Ha:xEu at 200 °C, for x= 5%, 10%, 15% and 20%.

the reagents used in the synthesis and isostructural characteristics, the substitution of lanthanum for europium is proposed since Lanthanides have a similar ionic radius. In addition, due to the ionic radius of hydrogen (Ionic radius = 2.08 Å) and phosphorus (Ionic radius = 2.12 Å) being similar too, is proposed the substitution of phosphorus for hydrogen. The result is a hydroxyapatite doped with europium ( $\text{Ca}_{10-x}\text{Eu}_x(\text{PO}_4)_6(\text{OH})_2$ ). Moreover, another phase with COD card 9001652 is obtained and corresponds to Monazite ( $\text{EuPO}_4$ ), also known as europium phosphate.

For 10%, 15%, and 20%, the best match was obtained with COD cards 9001652 Monazite and 7038853 ( $\text{Ca}_{6.52}\text{La}_{3.48}\text{O}_{26}\text{P}_{4.52}\text{Si}_{1.48}$ ). The substitution of the La atoms by Eu and the Si (Ionic radius = 0.41 Å) atoms by P (Ionic radius = 0.44 Å) was proposed since they have similar ionic radio. As a result, calcium phosphate doped with europium ( $\text{Ca}_3\text{Eu}_x(\text{PO}_4)_2$ ) was obtained.

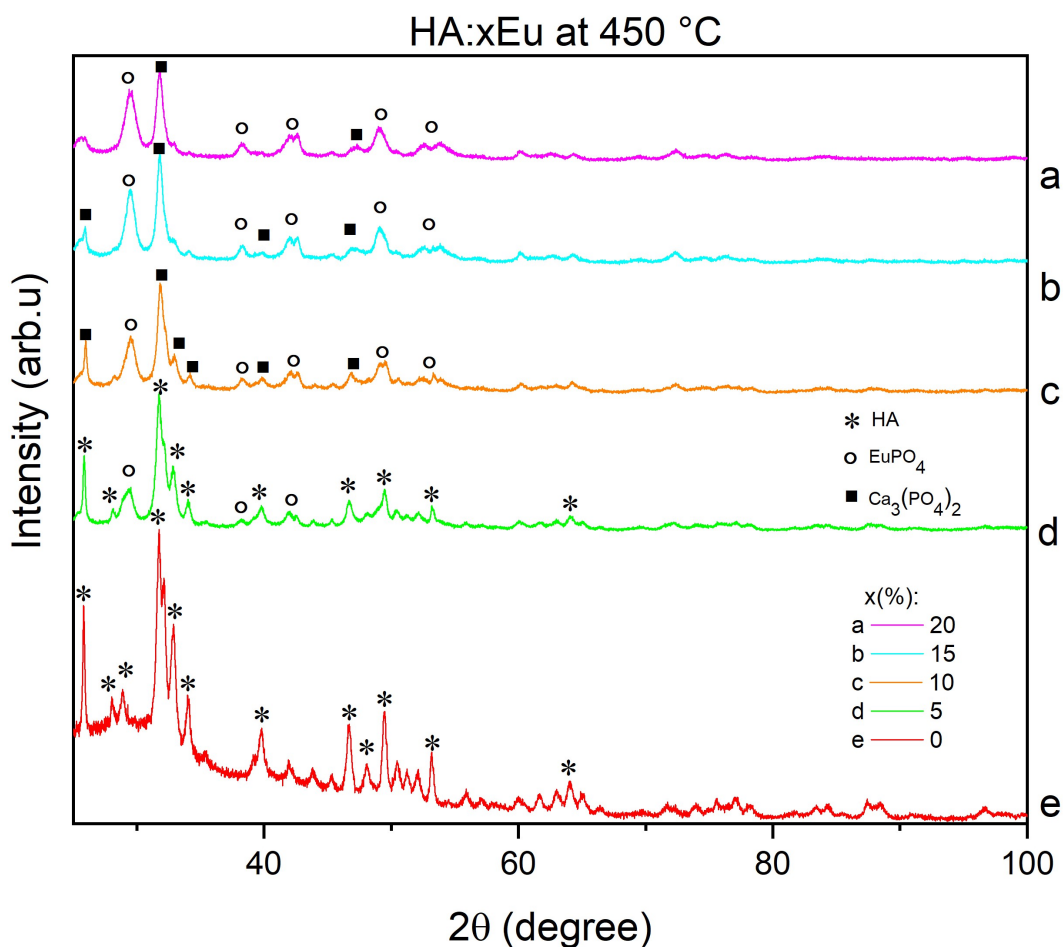


Figure 4.10: XRD Spectrum for Ha:xEu at 450 °C, for  $x=5\%$ ,  $10\%$ ,  $15\%$  and  $20\%$ .

#### Analysis and comparison of the XRD results.

For all temperatures, the XRD results agree with the FTIR results. In FTIR, it was obtained that from 10% europium concentration, a phase change from hydroxyapatite to calcium phosphate occurs. This phase change is verified by obtaining calcium phosphate doped with europium from 10% in XRD results for all the concentrations and all the temperatures.

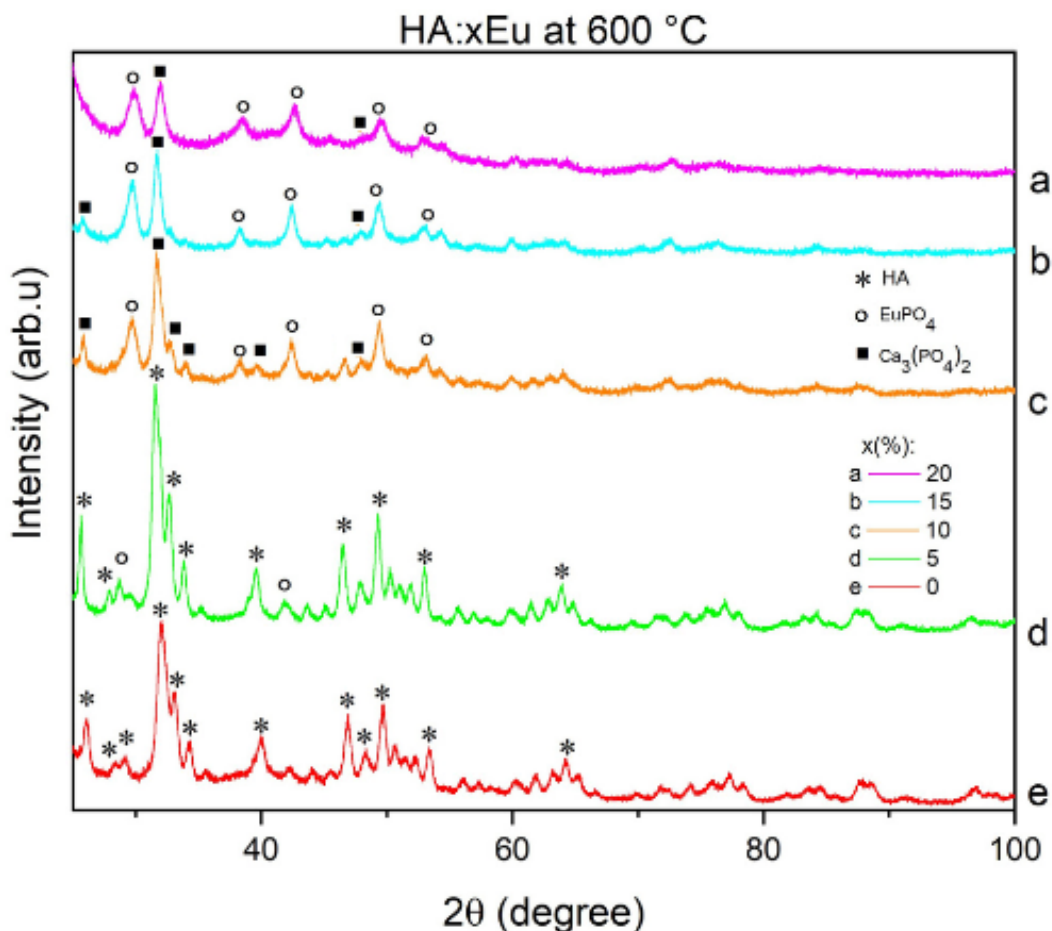


Figure 4.11: XRD Spectrum for Ha:xEu at 600 °C, for  $x = 5\%$ ,  $10\%$ ,  $15\%$  and  $20\%$ .

#### 4.1.4 Raman Spectroscopy

To confirm the vibrational interpretation previously performed with FTIR, Raman spectroscopy was used for the analysis of the chemical structure and crystallinity of the samples. Figure (4.17) shows the Raman spectra collected in the  $0\text{-}3500\text{ cm}^{-1}$  range for HA:xEu at ambient temperature,  $200\text{ °C}$ ,  $450\text{ °C}$ ,  $600\text{ °C}$ , and  $800\text{ °C}$ . Additionally, band positions (wavenumber,  $\text{cm}^{-1}$ ) and band assignments for ambient temperature,  $200\text{ °C}$ ,  $450\text{ °C}$ ,  $600\text{ °C}$ , and  $800\text{ °C}$ , are summarized in tables (4.7), (4.8), (4.9), (4.10), and (4.11) respectively. The presence of characteristic bands related to the vibrational modes of the  $(\text{PO}_4)^{3-}$ -groups can be observed in the spectra and the tables.

At ambient temperature, analyzing figure (4.13) and table 4.7, it is noted that the centered bands  $434\text{ cm}^{-1}$  and  $431\text{ cm}^{-1}$  are assigned to the  $\nu_2$  vibrations for  $x=0\%$  and  $x=5\%$ , respectively. In addition, the  $(\text{PO}_4)^{3-}$  bending

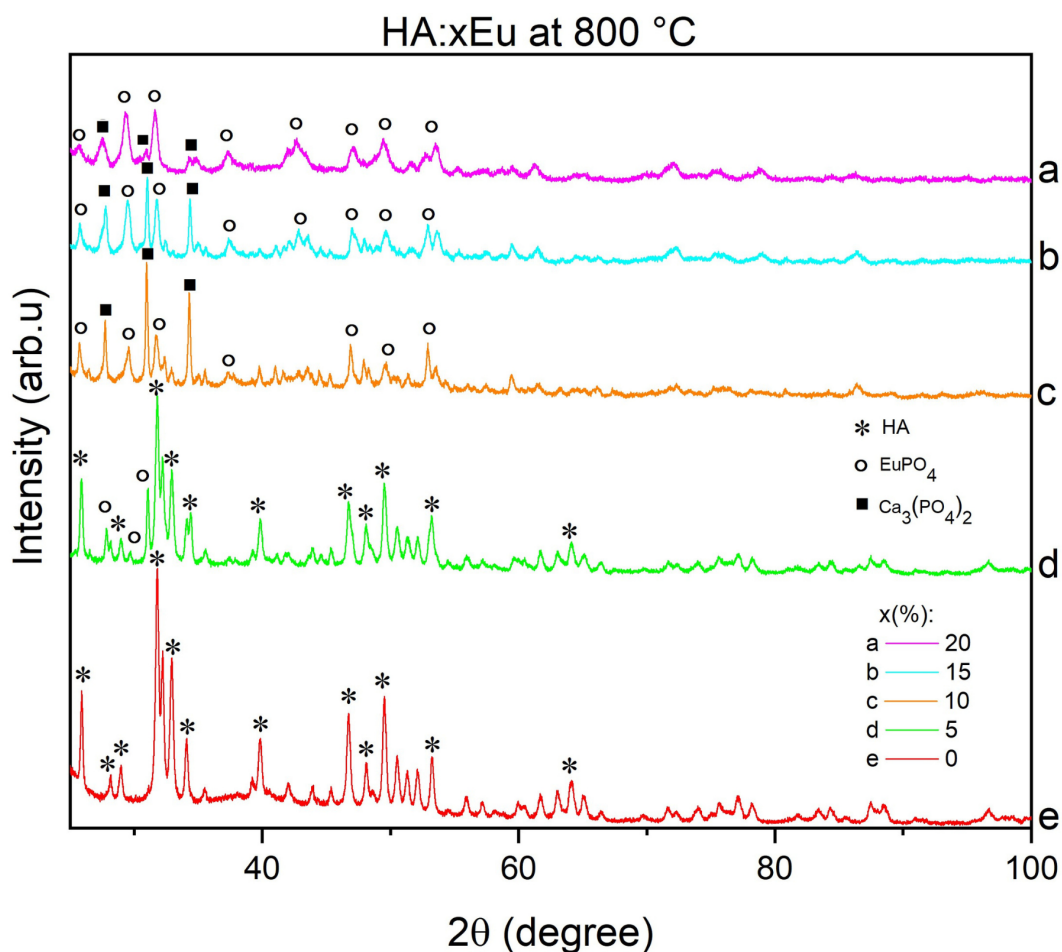


Figure 4.12: XRD Spectrum for Ha:xEu at 800 °C, for  $x = 5\%$ ,  $10\%$ ,  $15\%$  and  $20\%$ .

vibration,  $\nu_4$ , is attributed to the  $595\text{ cm}^{-1}$  band with  $5\%$  europium. The strong bands between  $960\text{ cm}^{-1}$  and  $965\text{ cm}^{-1}$ , for  $x=0\%$ ,  $5\%$ ,  $10\%$ , and  $15\%$ , are due to the symmetric stretching mode of the  $\nu_1(\text{PO}_4)^{3-}$  groups. While the  $1049\text{ cm}^{-1}$  dispersion is attributed to the asymmetric stretching vibration of  $\nu_3(\text{PO}_4)^{3-}$ .

At  $200\text{ }^\circ\text{C}$ , figure (4.14) and table 4.8, the centered bands  $429\text{ cm}^{-1}$ ,  $431\text{ cm}^{-1}$  and  $432\text{ cm}^{-1}$  are assigned to the  $\nu_2$  vibrations for  $x=10\%$ ,  $x=5\%$  and  $x=0\%$ , respectively. In addition, the  $(\text{PO}_4)^{3-}$  bending vibration,  $\nu_4$ , is attributed to the  $593\text{ cm}^{-1}$  band with  $5\%$  europium, and  $591\text{ cm}^{-1}$  band with  $0\%$  europium. The strong bands between  $963\text{ cm}^{-1}$  and  $991\text{ cm}^{-1}$ , for all the concentrations, are due to the symmetric stretching mode of the  $\nu_1(\text{PO}_4)^{3-}$  groups. While the  $1049\text{ cm}^{-1}$  ( $x=10\%$ ),  $1050\text{ cm}^{-1}$  ( $x=5\%$ ), and  $1048\text{ cm}^{-1}$  ( $x=0\%$ ) dispersion are attributed to the asymmetric stretching vibration of  $\nu_3(\text{PO}_4)^{3-}$ .

Ha:xEu	COD Card	Phase	Space Group	Crystal Structure	Cell Parameters
x=0%	9011093	Ca <sub>10</sub> (PO <sub>4</sub> ) <sub>6</sub> (OH) <sub>2</sub>	P 6 <sub>3</sub> /m	Hexagonal	a=9.42400 Å c=6.87900 Å
x=5%	7038854	Ca <sub>10-x</sub> Eu <sub>x</sub> (PO <sub>4</sub> ) <sub>6</sub> (OH) <sub>2</sub>	P 6 <sub>3</sub> /m	Hexagonal	a=9.46060 Å c=6.93560 Å
	9001652	EuPO <sub>4</sub>	P2 <sub>1</sub> /c	Monoclinic	a=6.66130 Å b=6.86180 Å c=6.34910 Å β=103.960 °
x=10%	7038853	Ca <sub>3-x</sub> Eu <sub>x</sub> (PO <sub>4</sub> ) <sub>2</sub>	P 6 <sub>3</sub> /m	Hexagonal	a=9.53251 Å c=7.02062 Å
	9001652	EuPO <sub>4</sub>	P2 <sub>1</sub> /c	Monoclinic	a=6.66130 Å b=6.86180 Å c=6.34910 Å β=103.960 °
x=15%	7038853	Ca <sub>3-x</sub> Eu <sub>x</sub> (PO <sub>4</sub> ) <sub>2</sub>	P 6 <sub>3</sub> /m	Hexagonal	a=9.53251 Å c=7.02062 Å
	9001652	EuPO <sub>4</sub>	P2 <sub>1</sub> /c	Monoclinic	a=6.66130 Å b=6.86180 Å c=6.34910 Å β=103.960 °
x=20%	7038853	Ca <sub>3-x</sub> Eu <sub>x</sub> (PO <sub>4</sub> ) <sub>2</sub>	P 6 <sub>3</sub> /m	Hexagonal	a=9.53251 Å c=7.02062 Å
	9001652	EuPO <sub>4</sub>	P2 <sub>1</sub> /c	Monoclinic	a=6.66130 Å b=6.86180 Å c=6.34910 Å β=103.960 °

Table 4.6: Phase analysis using experimentally obtained powder diffraction data compared to the Open Crystallography Database (COD) for HA:xEu with x=0%, 5%, 10%, 15%, and 20%, for all temperatures.<sup>27, 28, 29, 30, 31, 32, 33, 34</sup>

For 400 °C, figure (4.15) and table 4.9 , it is noted that the centered bands between 427 cm<sup>-1</sup> and 457 cm<sup>-1</sup> are assigned to the ν<sub>2</sub> vibrations for x=20%, 15% and 10%, respectively. In addition, the (PO<sub>4</sub>)<sup>3-</sup> bending vibration, ν<sub>4</sub>, is attributed to the 590 cm<sup>-1</sup> band for x=10% europium. The strong bands between 963 cm<sup>-1</sup> and 988 cm<sup>-1</sup>, for all the concentrations, are due to the symmetric stretching mode of the ν<sub>1</sub>(PO<sub>4</sub>)<sup>3-</sup> groups. While the 1048 cm<sup>-1</sup> dispersion, for x=10%, 5%, and 0%, are attributed to the asymmetric stretching vibration of ν<sub>3</sub>(PO<sub>4</sub>)<sup>3-</sup>.

The figure (4.16) and table 4.10 shows the bands at 600 °C. The centered bands ~431 cm<sup>-1</sup> for all the concentrations are assigned to the ν<sub>2</sub> vibrations, respectively. In addition, the (PO<sub>4</sub>)<sup>3-</sup> bending vibration, ν<sub>4</sub>, is attributed to the 592 cm<sup>-1</sup> band for x=5% and 10%. The strong band ~964 cm<sup>-1</sup>, for all the concentrations, are due to the symmetric stretching mode of the ν<sub>1</sub>(PO<sub>4</sub>)<sup>3-</sup> groups. While the 1049 cm<sup>-1</sup> dispersion, for x=5%, and 0%, are attributed to the

asymmetric stretching vibration of  $\nu_3(\text{PO}_4)^{3-}$ .

At 800 °C the presence of characteristic bands related to the vibrational modes of the  $(\text{PO}_4)^{3-}$ -groups can be observed in figure (4.17) and table (4.11). Analyzing, it is noted that the centered bands between 425  $\text{cm}^{-1}$  and 505  $\text{cm}^{-1}$  for all the concentrations are assigned to the  $\nu_2$  vibrations, respectively. In addition, the  $(\text{PO}_4)^{3-}$  bending vibration,  $\nu_4$ , is attributed to bands between 580  $\text{cm}^{-1}$  and 608  $\text{cm}^{-1}$  for  $x=5\%$  and 0%. The strong band between 962  $\text{cm}^{-1}$  and 989  $\text{cm}^{-1}$ , for all concentrations, is due to the symmetric stretching mode of the  $\nu_1(\text{PO}_4)^{3-}$  groups. While the dispersions between 1048  $\text{cm}^{-1}$  and 1077  $\text{cm}^{-1}$ , for  $x=5\%$ , and 0%, are attributed to the asymmetric stretching vibration of  $\nu_3(\text{PO}_4)^{3-}$ . Finally, for  $x=15\%$ , and 20%, the presence of fluorescence was found between 2000  $\text{cm}^{-1}$  - 3000  $\text{cm}^{-1}$ .

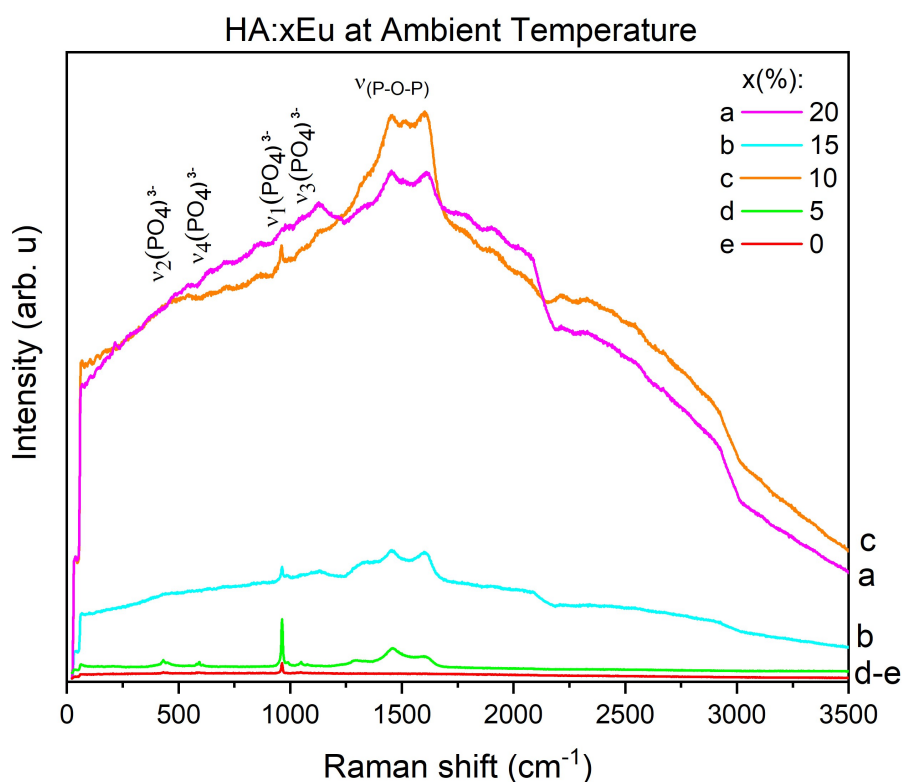


Figure 4.13: Raman spectrum for Ha:xEu at ambient temperature, for  $x=5\%$ , 10%, 15%, and 20%.

#### Analysis and comparison of the Raman results.

For all temperatures, comparing the peaks for  $x=5\%$ , 10%, 15% and 20% assigned to the  $\nu_1(\text{PO}_4)^{3-}$  vibration, as the Eu concentration increases, this peak attenuates. This characteristic is explained as the effect of Eu incorporation in

Assignment	Raman Shift (cm <sup>-1</sup> )					References
	x= 20%	x= 15%	x= 10%	x= 5%	x= 0%	
$\nu_2(\text{PO}_4)^{3-}$	0	0	0	431	434	19, 93, 94, 95
$\nu_4(\text{PO}_4)^{3-}$	0	0	0	595	0	19, 93, 94, 95
$\nu_1(\text{PO}_4)^{3-}$	0	962	960	965	963	19, 93, 94, 95
$\nu_3(\text{PO}_4)^{3-}$	0	0	0	1049	0	19, 93, 94, 95
$\nu_{(P-O-P)}$	1200-1700	1200-1700	1200-1700	1200-1700	0	96

Table 4.7: Assignment of Raman peaks of HA:xEu at Ambient Temperature, for x= 5%, 10%, 15%, and 20%.

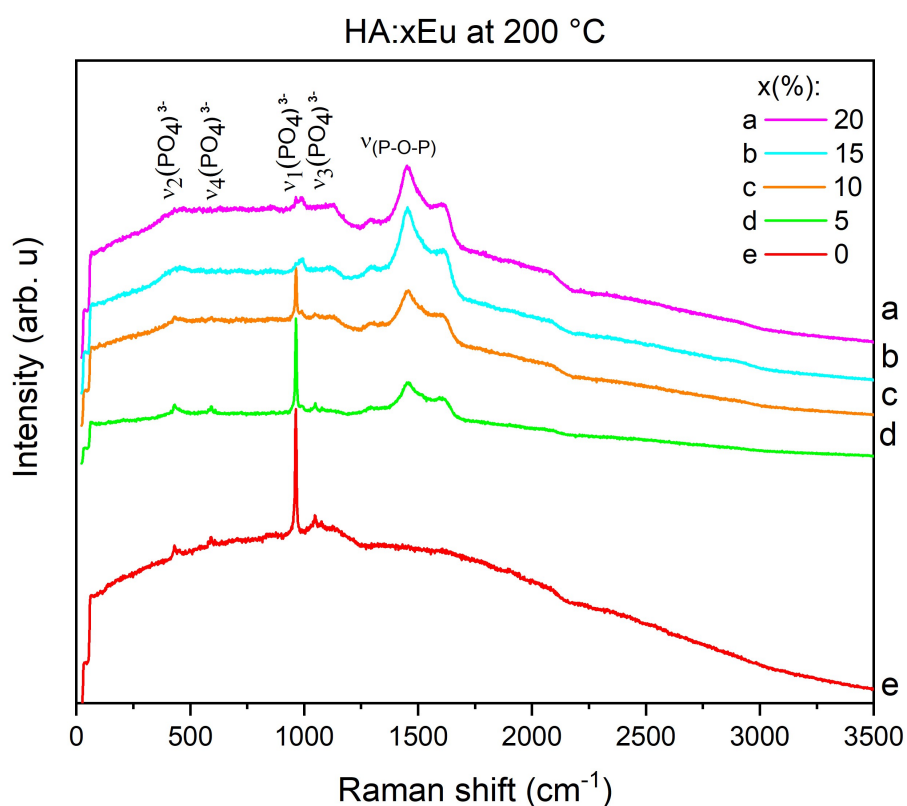


Figure 4.14: Raman spectrum for Ha:xEu at 200 °C, for x= 5%, 10%, 15% and 20%.

the sample and is present in other Raman spectra of Eu-doped hydroxyapatite<sup>95</sup>. Furthermore, it is observed that at room temperature, the intensity of the peaks is relatively low, especially for HA:0%Eu, where only the characteristic peaks  $\nu_1$  and  $\nu_2$  are observed increasing the image; however, these peaks are almost negligible. Nevertheless, these peaks are present and indicate HA formation. In addition, it is observed that at 200 °C, 450 °C, 600 °C and 800

Assignment	Raman Shift ( $\text{cm}^{-1}$ )					References
	x= 20%	x= 15%	x= 10%	x= 5%	x= 0%	
$\nu_2(\text{PO}_4)^{3-}$	0	0	429	431	432	19, 93, 94, 95
$\nu_4(\text{PO}_4)^{3-}$	0	0	0	593	591	19, 93, 94, 95
$\nu_1(\text{PO}_4)^{3-}$	965-988	991	964	963	963	19, 93, 94, 95
$\nu_3(\text{PO}_4)^{3-}$	0	0	1049	1050	1048	19, 93, 94, 95
$\nu_{(P-O-P)}$	1200-1700	1200-1700	1200-1700	1200-1700	0	96

Table 4.8: Assignment of Raman peaks of HA:xEu at 200 °C, for x= 5%, 10%, 15%, and 20%.

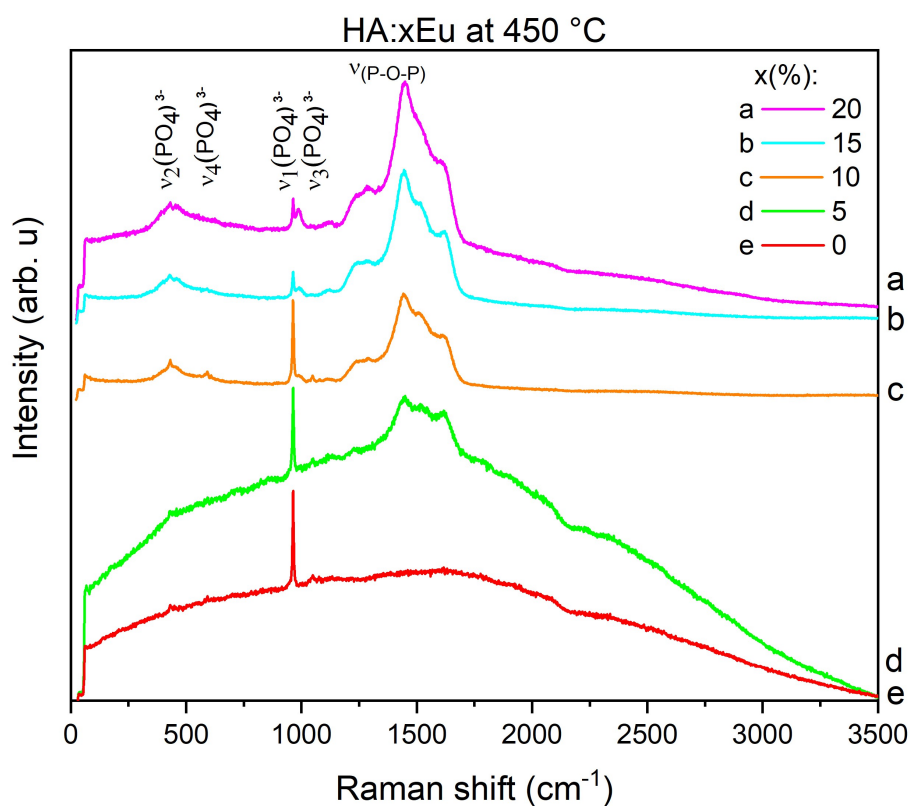


Figure 4.15: Raman spectrum for Ha:xEu at 450 °C, for x= 5%, 10%, 15% and 20%.

°C, the intensity of the peak  $\nu_1$  at  $963\text{cm}^{-1}$  for HA:0%Eu is strong, indicating that hydroxyapatite has formed and crystallized properly.

Finally, the characteristic bands related to the vibrational modes of the  $(\text{PO}_4)^{3-}$  groups are present in the Raman and FTIR spectra for all temperatures, indicating the formation of HA in both techniques. Thus, even the attenuation

Assignment	Raman Shift (cm <sup>-1</sup> )					References
	x= 20%	x= 15%	x= 10%	x= 5%	x= 0%	
$\nu_2(\text{PO}_4)^{3-}$	432-457	427	432	0	0	19, 93, 94, 95
$\nu_4(\text{PO}_4)^{3-}$	0	0	590	0	0	19, 93, 94, 95
$\nu_1(\text{PO}_4)^{3-}$	963-988	963-988	963	963	963	19, 93, 94, 95
$\nu_3(\text{PO}_4)^{3-}$	0	0	1048	1048	1048	19, 93, 94, 95
$\nu_{(P-O-P)}$	1200-1700	1200-1700	1200-1700	1200-1700	0	96

Table 4.9: Assignment of Raman peaks of HA:xEu at 450 °C, for x= 5%, 10%, 15%, and 20%.

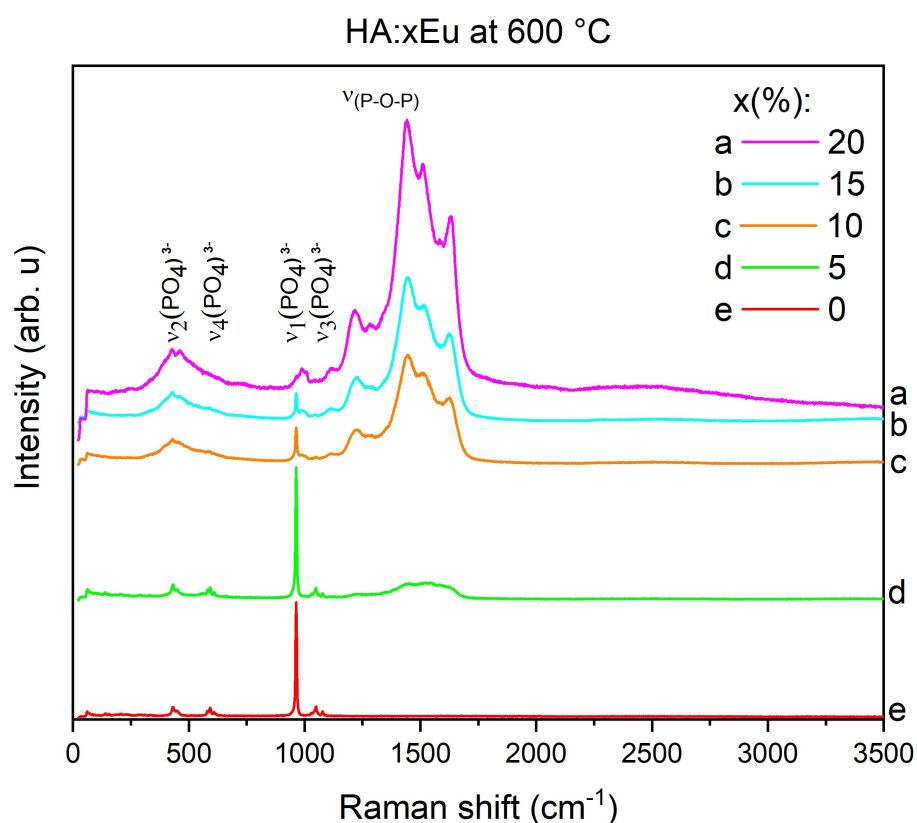


Figure 4.16: Raman spectrum for Ha:xEu at 600 °C, for x= 5%, 10%, 15% and 20%.

of the peaks corresponding to these groups indicates that the doping of HA with  $\text{Eu}^{3+}$  was successfully achieved. It is essential to mention that between the range 1200 cm<sup>-1</sup> and 1700 cm<sup>-1</sup>, some peaks increase in intensity with the concentration of europium. These peaks correspond to stretching vibration modes  $\nu_{(P-O-P)_{sym}}$  and  $\nu_{(P-O-P)_{asym}}$ , characteristic of phosphate groups<sup>96</sup>. Considering that in the results obtained in XRD, the formation of europium

Assignment	Raman Shift (cm <sup>-1</sup> )					References
	x= 20%	x= 15%	x= 10%	x= 5%	x= 0%	
$\nu_2(\text{PO}_4)^{3-}$	431-459	431	431	431	431	19, 93, 94, 95
$\nu_4(\text{PO}_4)^{3-}$	0	0	0	592	592	19, 93, 94, 95
$\nu_1(\text{PO}_4)^{3-}$	965	964	964	964	964	19, 93, 94, 95
$\nu_3(\text{PO}_4)^{3-}$	0	0	0	1049	1049	19, 93, 94, 95
$\nu(\text{P-O-P})$	1200-1700	1200-1700	1200-1700	1200-1700	0	96

Table 4.10: Assignment of Raman peaks of HA:xEu at 600 °C, for x= 5%, 10%, 15%, and 20%.

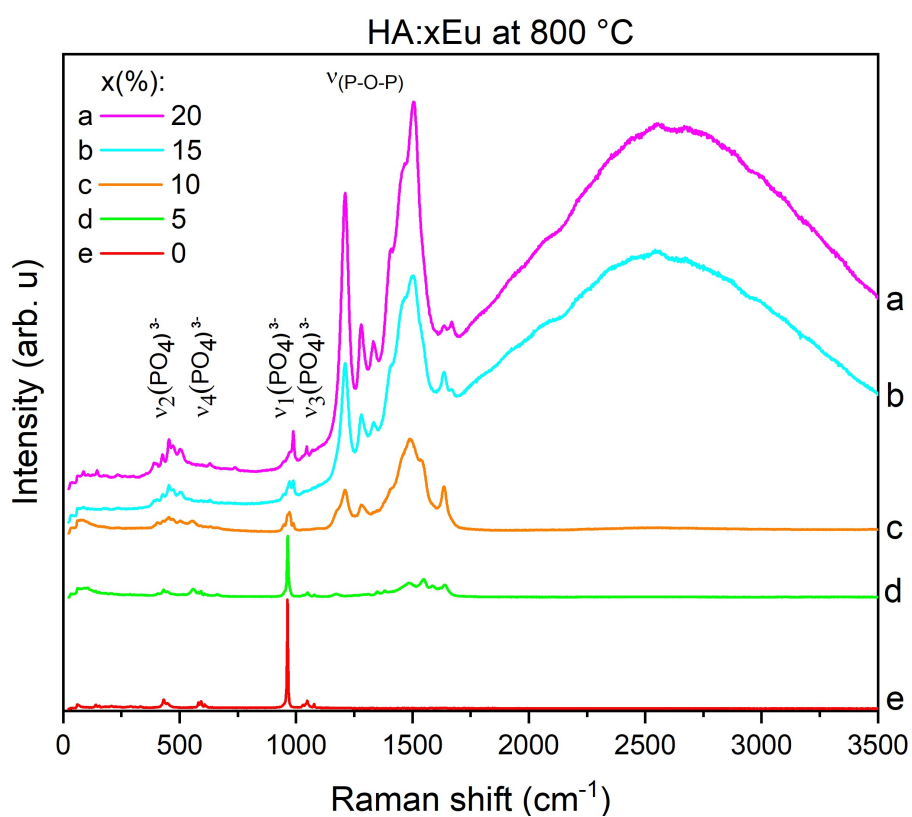


Figure 4.17: Raman spectrum for Ha:xEu at 800 °C, for x= 5%, 10%, 15% and 20%.

phosphate and calcium phosphate doped with europium are appreciated, these peaks between the 1200 cm<sup>-1</sup> and 1700 cm<sup>-1</sup> can be attributed to these phases.

Assignment	Raman Shift (cm <sup>-1</sup> )					References
	x= 20%	x= 15%	x= 10%	x= 5%	x= 0%	
$\nu_2(\text{PO}_4)^{3-}$	425-504	426-505	453	430	432-450	19, 93, 94, 95
$\nu_4(\text{PO}_4)^{3-}$	0	0	0	581-591	580-608	19, 93, 94, 95
$\nu_1(\text{PO}_4)^{3-}$	989	971-988	962-989	963	963	19, 93, 94, 95
$\nu_3(\text{PO}_4)^{3-}$	0	0	0	1050	1048-1077	19, 93, 94, 95
$\nu_{(P-O-P)}$	1200-1700	1200-1700	1200-1700	1200-1700	0	96

Table 4.11: Assignment of Raman peaks of HA:xEu at 800 °C, for x= 5%, 10%, 15%, and 20%.

### 4.1.5 Luminescence Spectroscopy

#### Photoluminescence analysis for HA:xEu at ambient temperature

The photoluminescence of the Eu-doped HA was performed with photoluminescence (PL) spectroscopy. This is a non-destructive technique, which is quite useful for evaluating the efficiency of trapping migration and transfer of charge carriers. In addition, to understand the crystallization behavior of the luminescent materials<sup>24</sup>. The photoluminescence spectrum of HA:xEu at room temperature is shown in figure (4.18). The intensity and position of the electronic transitions are shown in table (4.12). For concentrations, HA:xEu with x= 5%, 10%, 15% and 20% of strong visible emission peaks at 590 nm, 616 nm, 652 nm, 698 nm, attributed to  $5D_0 \rightarrow 7F_1$ ,  $5D_0 \rightarrow 7F_2$ ,  $5D_0 \rightarrow 7F_3$ ,  $5D_0 \rightarrow 7F_4$  transitions within Eu<sup>3+</sup> ion, respectively. In addition, it is observed that for x=5% the  $5D_0 \rightarrow 7F_0$  electronic transition is present at 574 nm, with low intensity. For x=0%, no luminescence is reported in this range.

Comparing the intensities of the peaks of each concentration, it is observed that as the concentration of europium increases, the intensity increases. However, this increase is not entirely linear, since for  $5D_0 \rightarrow 7F_2$  the concentration with the highest luminescence is x=20% with an intensity of 0.518 (arb. u), followed by x=10% with an intensity of 0.437 (arb. u), x=15% with an intensity of 0.349 (arb. u) and finally, x=5% with an intensity of 0.328 (arb. u).

Wavelength (nm)	Electronic Transition	Photoluminescence Intensity of HA:xEu (arb. u)					References
		x= 20%	x= 15%	x= 10%	x= 5%	x= 0%	
574	$5D_0-7F_0$	0	0	0	0.112	0	97
590	$5D_0-7F_1$	0.460	0.293	0.362	0.242	0	24, 97, 98
616	$5D_0-7F_2$	0.518	0.349	0.437	0.328	0	24
652	$5D_0-7F_3$	0.132	0.091	0.120	0.081	0	99
698	$5D_0-7F_4$	0.400	0.268	0.313	0.108	0	99

Table 4.12: Photoluminescence peak intensities for specific wavelengths of HA:xEu at ambient temperature, for x= 5%, 10%, 15%, and 20%.

The difference between the luminescence intensities can be explained by the phases formed for each concentration, shown in Table (4.6) of XRD analysis. First comparing the concentrations with higher (x=20%) and lower

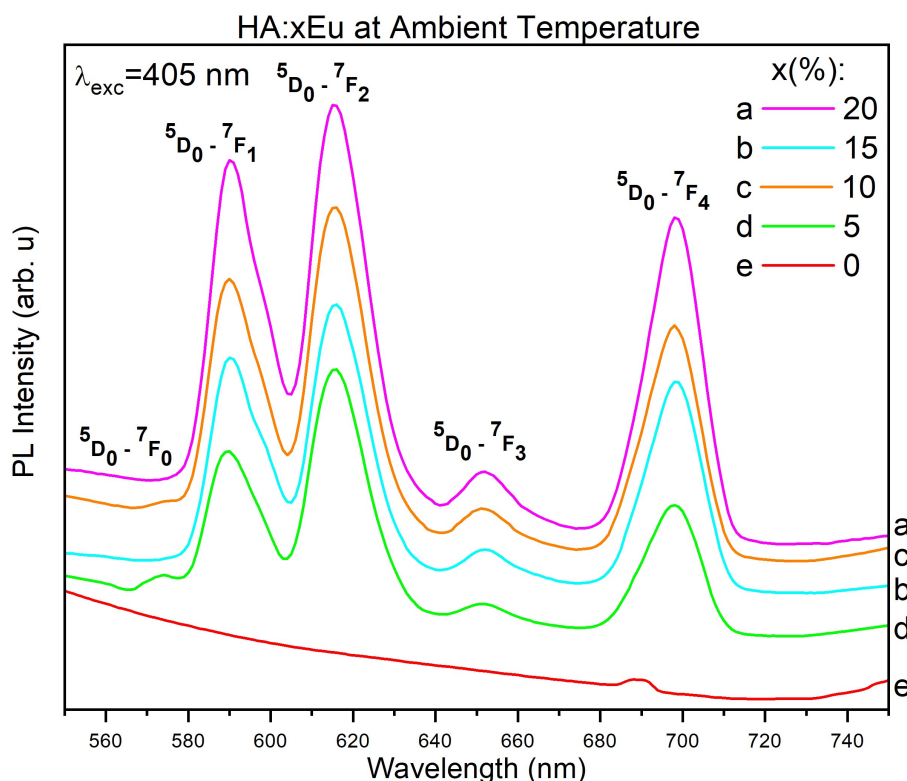


Figure 4.18: Photoluminescence spectra for Ha:xEu at room temperature, for  $x = 5\%$ ,  $10\%$ ,  $15\%$ , and  $20\%$ .

( $x = 5\%$ ) intensity of photoluminescence and the phases of these, it is obtained that although both concentrations have europium phosphate, for  $5\%$  europium doped hydroxyapatite is formed and for  $20\%$  europium doped calcium phosphate is formed. This result suggests that europium-doped calcium phosphate is a more luminescent phase.

Furthermore, it is observed that the cell parameters of calcium phosphate are slightly higher than those of HA. This may be the cause of the difference in intensities since, as mentioned above, in the factors affecting luminescence; external conversions compete with fluorescence to release energy. Therefore, the closer together the molecules are, the greater the probability of collisions between them, and the more energy is released in non-radiative processes. Consequently, as the cell parameters are larger for  $x = 20\%$ , there is less probability of collisions and more probability that energy is released by photon emission.

On the other hand, for  $x = 10\%$ ,  $15\%$ , and  $20\%$  the presence of the same two phases is observed for all concentrations. In this case, the difference in luminescence intensity can be attributed to the amount of europium present in each sample. The sample with the highest photoluminescence intensity is the sample with the highest concentration

of europium. This agrees with the theory since the main element that presents luminescence in this hydrothermal synthesis is  $\text{Eu}^{3+}$ .

### Photoluminescence analysis for HA:xEu at 200 °C

The photoluminescence spectrum of HA:xEu at 200 °C is shown in figure (4.19). The intensity and position of the electronic transitions are shown in table (4.13). For concentrations, HA:xEu with  $x= 5\%$ ,  $10\%$ ,  $15\%$  and  $20\%$  of strong visible emission peaks at 589 nm, 615 nm, 651 nm, and 698nm, attributed to  $5\text{D}_0 \rightarrow 7\text{F}_1$ ,  $5\text{D}_0 \rightarrow 7\text{F}_2$ ,  $5\text{D}_0 \rightarrow 7\text{F}_3$ ,  $5\text{D}_0 \rightarrow 7\text{F}_4$  transitions within  $\text{Eu}^{3+}$  ion, respectively. In addition, it is observed the  $5\text{D}_0 \rightarrow 7\text{F}_0$  electronic transition at 574nm disappears for all the concentrations. For  $x=0\%$ , no luminescence is reported in this range.

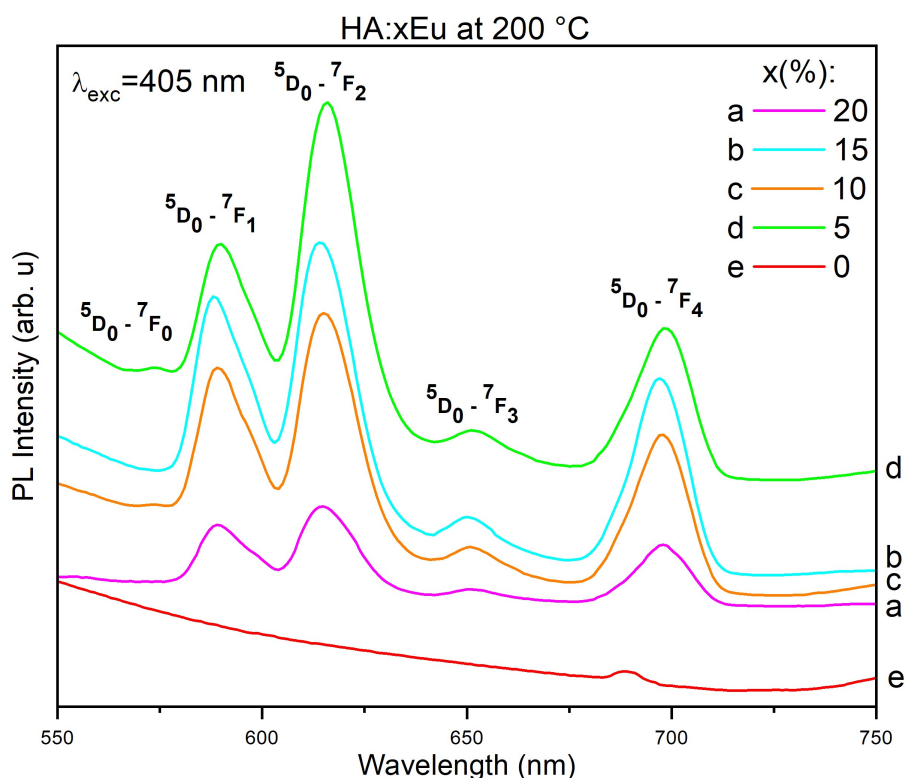


Figure 4.19: Photoluminescence spectrum for Ha:xEu at 200 °C, for  $x= 5\%$ ,  $10\%$ ,  $15\%$ , and  $20\%$ .

Comparing the intensities of the peaks, it can be qualitatively noted that the concentration with the highest luminescence is  $5\%$ , followed by  $15\%$ ,  $10\%$ , and  $20\%$ , successively. Likewise, quantitatively we can appreciate that for the electronic transition  $5\text{D}_0 \rightarrow 7\text{F}_2$ ,  $5\%$  has an intensity of 0.585 (arb. u),  $15\%$  has an intensity of 0.496 (arb.

u), 10% has an intensity of 0.452 (arb. u), and finally 20% with 0.155 (arb. u). These values indicate that the critical concentration value for 200 °C is 5% europium. As mentioned above in the factors influencing luminescence, it is known that after the inhibitory concentration, the optically active ions, instead of increasing the photon release, begin to release energy by non-radioactive processes.

Analyzing the results shown in the table (4.6), it can be seen that for 10%, 15%, and 20% there are the same phases, europium-doped calcium phosphate, and europium phosphate, and for 5% europium phosphate and europium-doped hydroxyapatite are formed. Comparing this with the photoluminescence intensities in the table (4.13), it is found that the PL of 20% is quite weak, but between 10% and 15%, there is no significant difference in intensities. In the same way, comparing these two concentrations (10% and 15%) with 5%, the difference in intensities is still not very large. Consequently, it is concluded that at 200 °C europium-doped hydroxyapatite ( $x=5\%$ ) has a significant role in photoluminescence. However, 5% has a higher intensity at high-energy electronic transitions, while 10% and 15% have a higher intensity at low-energy transitions. Finally, at 200 °C, 20% is not a good doping amount for radioactive processes.

Wavelength (nm)	Electronic Transition	Photoluminescence Intensity of HA:xEu (arb. u)					References
		$x=20\%$	$x=15\%$	$x=10\%$	$x=5\%$	$x=0\%$	
574	$^5D_0 \rightarrow ^7F_0$	0	0	0	0.224	0	97
589	$^5D_0 \rightarrow ^7F_1$	0.130	0.422	0.377	0.390	0	100
615	$^5D_0 \rightarrow ^7F_2$	0.155	0.496	0.452	0.585	0	98, 101
651	$^5D_0 \rightarrow ^7F_3$	0.042	0.122	0.133	0.137	0	99
698	$^5D_0 \rightarrow ^7F_4$	0.103	0.311	0.286	0.277	0	99

Table 4.13: Photoluminescence peak intensities for specific wavelengths of HA:xEu at 200 °C, for  $x=5\%$ , 10%, 15%, and 20%.

#### Photoluminescence analysis for HA:xEu at 450 °C

The photoluminescence spectrum of HA:xEu at 450 °C is shown in figure (4.20). The intensity and position of the electronic transitions are shown in table (4.14). For concentrations, HA:xEu with  $x=5\%$ , 10%, 15%, and 20% of strong visible emission peaks at 589 nm, 615 nm, 651 nm, and 698 nm, attributed to  $5D_0 \rightarrow 7F_1$ ,  $5D_0 \rightarrow 7F_2$ ,  $5D_0 \rightarrow 7F_3$ ,  $5D_0 \rightarrow 7F_4$  transitions within  $\text{Eu}^{3+}$  ion, respectively. In addition, the  $5D_0 \rightarrow 7F_0$ , electronic transition at 574 nm, appears for  $x=5\%$  and 10%. For  $x=0\%$ , no luminescence is reported in this range.

Comparing the intensities of the peaks, it can be qualitatively noted that the concentration with the highest luminescence is 15%, followed by 20%, 10%, and 5% successively. These values indicate that the critical concentration value for 450 °C is 15% europium. As mentioned above in the factors influencing luminescence, it is known that concentration values above the inhibitory concentration lead to a damping of luminescence since the optically active ions, instead of increasing the release of photons, begin to release energy by non-radioactive processes due to the

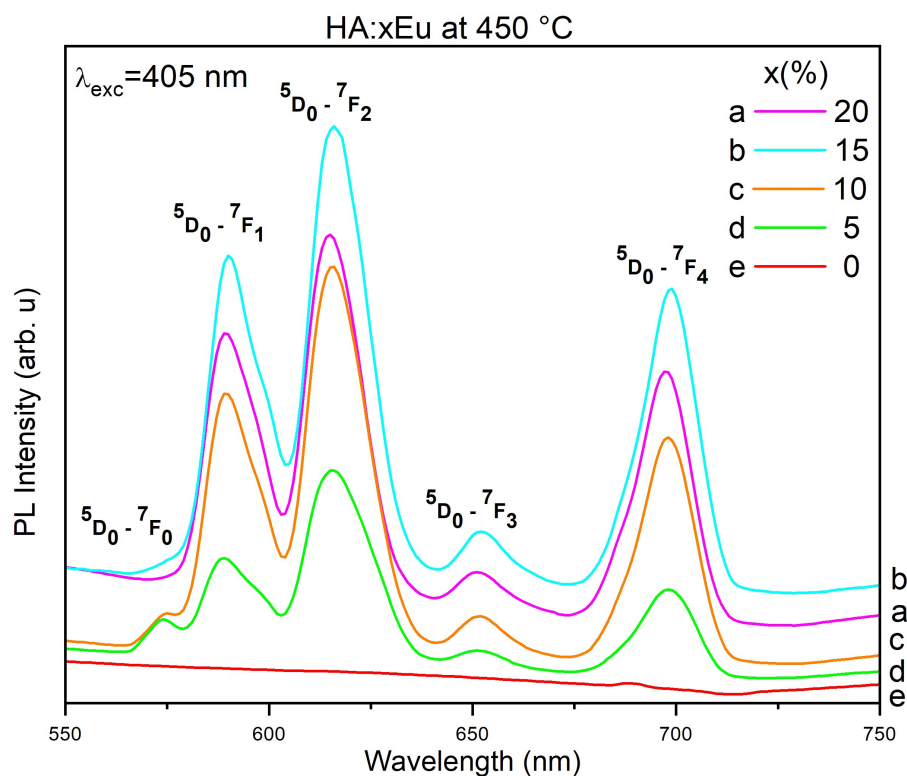


Figure 4.20: Photoluminescence spectrum for Ha:xEu at 450 °C, for  $x=5\%$ ,  $10\%$ ,  $15\%$ , and  $20\%$ .

proximity between them. Likewise, it can be seen that the luminescence intensity increases from 5% to 15% and then decays at 20% (Table 4.14).

Wavelength (nm)	Electronic Transition	Photoluminescence Intensity of HA:xEu (arb.u)					References
		$x=20\%$	$x=15\%$	$x=10\%$	$x=5\%$	$x=0\%$	
574	$^5D_0-^7F_0$	0	0	0.174	0.196	0	97
589	$^5D_0-^7F_1$	0.740	0.840	0.674	0.337	0	100
615	$^5D_0-^7F_2$	0.964	1.132	0.969	0.537	0	98, 101
651	$^5D_0-^7F_3$	0.195	0.209	0.166	0.124	0	99
698	$^5D_0-^7F_4$	0.652	0.762	0.576	0.264	0	99

Table 4.14: Photoluminescence peak intensities for specific wavelengths of HA:xEu at 450 °C, for  $x=5\%$ ,  $10\%$ ,  $15\%$ , and  $20\%$ .

On the other hand, comparing the results obtained in PL with the XRD analysis table (4.6), it is observed that the phases HA doped with europium and europium phosphate present in the sample  $x=5\%$ , do not generate an optimum

PL intensity. On the other hand, the samples of 10%, 15%, and 20% have the same phases, however, clearly in the graph 4.10 it can be noted that the concentration with the highest luminescence is 15%.

#### Photoluminescence analysis for HA:xEu at 600 °C

The photoluminescence spectrum of HA:xEu at 600 °C is shown in figure (4.21). The intensity and position of the electronic transitions are shown in table (4.15). For concentrations, HA:xEu with  $x=5\%$ ,  $10\%$ ,  $15\%$ , and  $20\%$  of strong visible emission peaks at 589 nm, 615 nm, 651 nm, and 698 nm, attributed to  $5D_0 \rightarrow 7F_1$ ,  $5D_0 \rightarrow 7F_2$ ,  $5D_0 \rightarrow 7F_3$ ,  $5D_0 \rightarrow 7F_4$  transitions within  $\text{Eu}^{3+}$  ion, respectively. In addition, the  $5D_0 \rightarrow 7F_0$ , electronic transition at 574 nm, appears for  $x=5\%$  and  $10\%$ . For  $x=0\%$ , no luminescence is reported in this range.

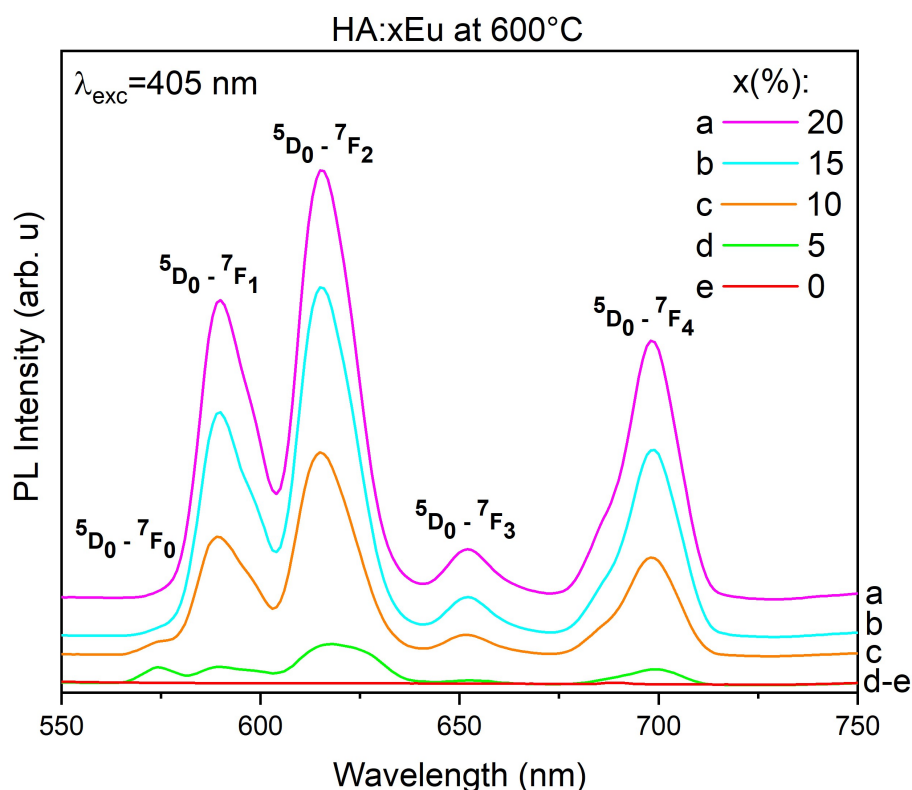


Figure 4.21: Photoluminescence spectrum for Ha:xEu at 600 °C, for  $x=5\%$ ,  $10\%$ ,  $15\%$ , and  $20\%$ .

Comparing the intensities of the peaks, it can be qualitatively noted that as the concentration of europium increases, the luminescence increases linearly, with 20% being the sample with the highest luminescence, followed by 15%, 10%, and 5%, successively. Likewise, quantitatively we can appreciate that for the electronic transition  $5D_0$

→  $7F_2$ , 20% has an intensity of 4.088 (arb. u), 15% has an intensity of 0.268 (arb. u), 10% has an intensity of 0.268 (arb. u), and finally 5% with 0.114 (arb. u). In this spectrum, no critical concentration can be seen.

Wavelength (nm)	Electronic Transition	Photoluminescence Intensity of HA:xEu (arb.u)					References
		x= 20%	x= 15%	x= 10%	x= 5%	x= 0%	
574	$^5D_0 \rightarrow ^7F_0$	0	0	0.211	0.237	0	97
589	$^5D_0 \rightarrow ^7F_1$	2.884	2.179	1.181	0.241	0	100
615	$^5D_0 \rightarrow ^7F_2$	4.088	3.340	1.970	0.453	0	98, 101
651	$^5D_0 \rightarrow ^7F_3$	0.563	0.451	0.268	0.114	0	99
698	$^5D_0 \rightarrow ^7F_4$	2.504	1.816	0.985	0.218	0	99

Table 4.15: Photoluminescence peak intensities for specific wavelengths of HA:xEu at 600 °C, for x= 5%, 10%, 15%, and 20%.

On the other hand, comparing the results obtained in PL with the XRD analysis table (4.6), it is observed that the same phases exist for 10%, 15%, and 20%. Therefore, it cannot be deduced that there is no energy loss due to external conversion. This is also evident in the PL spectrum, as there is no inhibitory concentration. Finally, as expected, higher europium concentration, higher luminescence.

#### Photoluminescence analysis for HA:xEu at 800 °C

The photoluminescence spectrum of HA:xEu at 800 °C is shown in figure (4.21). The intensity and position of the electronic transitions are shown in table (4.15). For concentrations, HA:xEu with x= 5%, 10%, 15%, and 20% of strong visible emission peaks at 593 nm, ~615 nm, 653 nm, and ~700 nm, attributed to  $5D_0 \rightarrow 7F_1$ ,  $5D_0 \rightarrow 7F_2$ ,  $5D_0 \rightarrow 7F_3$ ,  $5D_0 \rightarrow 7F_4$  transitions within  $\text{Eu}^{3+}$  ion, respectively. In addition, the  $5D_0 \rightarrow 7F_0$ , electronic transition at 574 nm, appears for x=5% and 10%. For x=0%, no luminescence is reported in this range.

Comparing the intensities of the peaks, it can be qualitatively noted that the concentration with the highest luminescence is 15%, followed by 20%, 10%, and 5% successively. These values indicate that the critical concentration value for 800 °C is 15% europium. As mentioned above in the factors influencing luminescence, it is known that concentration values above the inhibitory concentration lead to a damping of luminescence since the optically active ions, instead of increasing the release of photons, begin to release energy by non-radioactive processes due to the proximity between them. Likewise, it can be seen that the luminescence intensity increases from 5% to 15% and then decays at 20%.

On the other hand, comparing the results obtained in PL with the XRD table (4.6) analysis, it can be seen that for all the concentrations europium phosphate is present. However, for x=5%, hydroxyapatite doped with europium is formed. From x=10% the same phases with the same COD card, i.e. the same cell parameters, are present, these

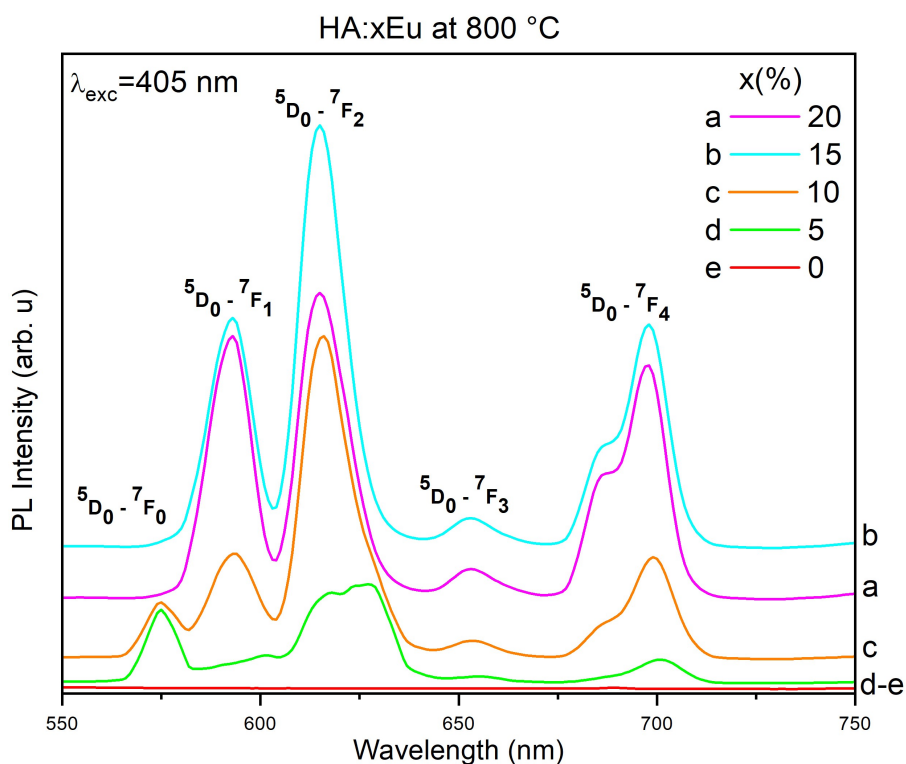


Figure 4.22: Photoluminescence spectrum for Ha:xEu at 800 °C, for  $x=5\%$ ,  $10\%$ ,  $15\%$ , and  $20\%$ .

Wavelength (nm)	Electronic Transition	Photoluminescence Intensity of HA:xEu (arb. u)					References
		$x=20\%$	$x=15\%$	$x=10\%$	$x=5\%$	$x=0\%$	
574	$^5D_0-^7F_0$	0	0	1.060	1.347	0	97
593	$^5D_0-^7F_1$	4.655	4.039	1.905	0	0	99
615	$^5D_0-^7F_2$	5.369	7.357	5.659	0	0	98, 101
618	$^5D_0-^7F_2$	0	0	0	1.634	0	97
624	$^5D_0-^7F_2$	0	0	0	1.763	0	99
653	$^5D_0-^7F_3$	0.647	0.630	0.420	0.199	0	97
685	$^5D_0-^7F_4$	2.260	1.838	0.638	0	0	99
700	$^5D_0-^7F_4$	4.138	3.948	1.833	0.486	0	24, 97, 98, 100

Table 4.16: Photoluminescence peak intensities for specific wavelengths of HA:xEu at 800 °C, for  $x=5\%$ ,  $10\%$ ,  $15\%$ , and  $20\%$ .

are europium-doped calcium phosphate and europium phosphate (Monazite).

Taking this into account, the maximum concentration of these phases for optimum luminescence is  $15\%$ . For

5% and 10%, there is not enough concentration of optically active europium ions to obtain a high luminescence intensity, also it is understood that for this temperature calcium phosphate is more luminescent than HA. For  $x=20\%$ , the concentration of optically active ions is too high, which causes the ions to be closer together and release energy through non-radiative processes. Additionally, comparing the intensity of the peaks for all temperatures, it was obtained that the temperature with the highest luminescence intensity was 800 °C, and the optimum concentration at this temperature was HA:15%Eu.

Finally, comparing the luminescence color of each HA:xEu pellet at 800 °C under a UV lamp (Figure 3.2), it can be observed that as the concentration of europium increases, the luminescence changes from a blue-violet color (wavelengths of approximately 400 nm) to reddish-yellow colors (wavelengths between 600-700 nm). According to theory, pure hydroxyapatite, due to  $\text{CO}_2^-$  defects, tends to have a blue light emission of 428 nm<sup>(69)</sup>. However, the luminescence of europium is usually red. This visually indicates that the hydroxyapatite was successfully doped with europium.

## Chapter 5

# Conclusions & Outlook

The hydrothermal method used to synthesize hydroxyapatite doped with europium was successful. This was confirmed by the different characterization techniques performed. Using Fourier transform infrared (FTIR) spectroscopy, the characteristic bands of hydroxyapatite were observed for  $\nu_1(\text{PO}_4)^{3-}$ ,  $\nu_2(\text{PO}_4)^{3-}$ ,  $\nu_3(\text{PO}_4)^{3-}$ , and  $\nu_4(\text{PO}_4)^{3-}$ . The wavenumber of these groups varied depending on the temperature and concentration. However, there was no significant difference. On the other hand, it was observed that the characteristic peaks of HA  $\nu_1(\text{PO}_4)^{3-}$ ,  $\nu_2(\text{PO}_4)^{3-}$ ,  $\nu_3(\text{PO}_4)^{3-}$ , and  $\nu_s(\text{OH})^-$ , was disappearing and/or varying with increasing europium concentration and temperature. This indicates that the hydroxyapatite was possibly transformed into a calcium phosphate.

The presence of europium in the samples was confirmed by Scanning Electron Microscopy and EDX microanalysis on the HA:xEu samples at 800°C for x=5% and 20%. Small bright lines attributed to  $\text{Eu}^{3+}$  were observed in the BSE imaging of HA:5%Eu since this element has the highest atomic number of all the reagents used during the synthesis. On the other hand, the BSE imaging of HA:20%Eu shows a homogeneous and opaque surface. It is considered that the difference between these images lies in the fact that for HA:5%Eu, the europium is not fully integrated into the HA structure but is found superficially, unlike HA:20%Eu where it is presumed that the Eu atoms substituted better for the Ca atoms and were better integrated into the host material. On the other hand, it is appreciated that the hydrothermal synthesis generated microparticles with regular morphology (50 $\mu\text{m}$ -350 $\mu\text{m}$ ).

The diffractograms obtained with XRD analysis showed the same phases for all temperatures. For x=0% hydroxyapatite was formed. For x=5% hydroxyapatite doped with europium and europium phosphate was found. For x=10%, 15%, and 20%, europium phosphate was maintained, and europium-doped hydroxyapatite was transformed into europium-doped calcium phosphate.

The XRD results agree with the FTIR results. In FTIR, it was obtained that from 10% europium concentration, a phase change from hydroxyapatite to calcium phosphate occurs. This phase change is verified by obtaining calcium phosphate doped with europium from 10% in XRD results for all the temperatures.

The presence of vibrational modes of the  $(\text{PO}_4)^{3-}$  group  $\nu_1(\text{PO}_4)^{3-}$ ,  $\nu_2(\text{PO}_4)^{3-}$ ,  $\nu_3(\text{PO}_4)^{3-}$ , and  $\nu_4(\text{PO}_4)^{3-}$ , was confirmed by Raman spectroscopy. In addition, it was observed that as the concentration of europium increases, the characteristic bands of HA are attenuated. This attenuation of the peaks indicates that the doping of hydroxyapatite with europium was successfully achieved, being an expected result. On the other hand, it is essential to mention that from  $x=5\%$  for all temperatures in the range of  $1200\text{ cm}^{-1}$  and  $1700\text{ cm}^{-1}$ , some peaks increase their intensity with increasing europium concentration. These peaks correspond to stretching vibration modes  $\nu_{(P-O-P)_{sym}}$  and  $\nu_{(P-O-P)_{asym}}$ , characteristic of phosphate groups. Considering that in the results obtained in XRD from  $x=5\%$  for all temperatures, the formation of europium phosphate and calcium phosphate doped with europium are appreciated, it is deduced that these peaks can be attributed to these phases.

Using photoluminescence spectroscopy, the corresponding electronic transitions of europium were obtained. These are found in the strong visible emission peaks at 574 nm, 590 nm, 616 nm, 652 nm, and 698 nm, attributed to  $5D_0 \rightarrow 7F_0$ ,  $5D_0 \rightarrow 7F_1$ ,  $5D_0 \rightarrow 7F_2$ ,  $5D_0 \rightarrow 7F_3$ ,  $5D_0 \rightarrow 7F_4$ . The PL intensity of these electronic transitions varies with concentration and temperature. Likewise, it was obtained that depending on the temperature; there are optimum concentrations of europium that showed the highest luminescence. This optimum concentration, known as "inhibitory concentration", is the maximum concentration of optically active ions ( $\text{Eu}^{3+}$ ) that a host material (HA) can have before these ions start to release energy by external conversions, and not by radioactive processes (photons). Since there start to be many collisions between them. Comparing the results obtained in PL with the XRD results, it is concluded that,

At ambient temperature, comparing the concentrations with higher ( $x=20\%$ ) and lower ( $x=5\%$ ) intensity of photoluminescence, and the phases of these, it is obtained that although both concentrations have europium phosphate, for 5% europium doped hydroxyapatite is formed and for 20% europium doped calcium phosphate is formed. This result suggests that europium-doped calcium phosphate is a more luminescent phase. Furthermore, it is observed that the cell parameters of calcium phosphate are slightly higher than those of HA. This may be the cause of the difference in intensities since to  $x=20\%$  there are more radiative processes.

At 200 °C, the sample  $x=5\%$  was found to exhibit the highest luminescence. Considering the XRD results, this sample is composed of hydroxyapatite doped with europium and europium phosphate. However, there is no huge difference in the luminescence intensity between 5%, 10%, and 15%. At 450 °C, the concentration with the highest luminescence is 15%.

At 600 °C, the luminescence increases linearly, with 20% being the sample with the highest luminescence, followed by 15%, 10%, and 5%, successively. As expected, the higher the europium concentration, the higher the luminescence. Furthermore, it is observed that as the europium concentration increases, the peaks corresponding to calcium phosphate disappear and the intensity of the europium phosphate peaks increases, however, both phases still exist. This result reveals that the presence of both phases plays an important role in increasing the luminescence intensity.

At 800 °C,  $x=15\%$  is the concentration with the highest luminescence. However, although  $x=20\%$  has a very similar luminescence intensity to  $x=10\%$  and  $15\%$ , the presence of europium-doped calcium phosphate is an important factor in increasing photoluminescence. This result agrees with that obtained at 600 °C, where the presence of the biphasic plays an important role in PL. Furthermore, comparing the intensity of the peaks for all temperatures, it was obtained that the temperature with the highest luminescence intensity was 800 °C, and the optimum concentration at this temperature was HA:15%Eu.

It was observed that when HA:xEu tablets were placed at 800 °C under a UV lamp, as the concentration of europium increased, the luminescence changed from a blue-violet color (wavelengths of approximately 400nm) to yellow-reddish colors (wavelengths between 600-700 nm). According to theory, due to  $\text{CO}_2^-$  defects, pure hydroxyapatite tends to have a blue light emission of 428 nm. However, the luminescence of europium is usually red. This visually indicates that the hydroxyapatite was successfully doped with europium.

With the hydrothermal synthesis, it was possible to optimally substitute the calcium atoms with europium, generating two multifunctional materials, europium-doped hydroxyapatite, and europium-doped calcium phosphate. Both materials with excellent properties, the most important being biocompatibility and luminescence. Since these properties are of great utility and interest in medicine, having a wide variety of applications, such as biocompatible fluorescent labeling material, drug release and targeting, disease therapy, antimicrobial activity testing, bioimaging, magnetic resonance imaging, bimodal imaging, cellular imaging and many more.

Finally, in this degree project, it was studied five temperatures for five different concentrations of how heat treatment affects the luminescence of hydroxyapatite doped with europium, which provides a wide range of data for future research. Permitting found the optimal temperature and concentration that allows the highest photoluminescence intensity of europium-doped hydroxyapatite and europium-doped calcium phosphate. All this was achieved thanks to the characterization techniques that allow us to understand what happens in our samples at the nano and micro scale.



# Bibliography

- [1] White, A. A.; Best, S. M.; Kinloch, I. A. Hydroxyapatite-carbon nanotube composites for biomedical applications: A review. *International Journal of Applied Ceramic Technology* **2007**, *4*, 1–13.
- [2] Chen, Z.; Dinh, H. N.; Miller, E. Photoelectrochemical water splitting: standards, experimental methods, and protocols. 2013, 126.
- [3] Dunnill, C. W.; Parkin, I. P. Nitrogen-doped TiO<sub>2</sub> thin films: Photocatalytic applications for healthcare environments. 2011.
- [4] Lu, X.; Zhang, H.; Guo, Y.; Wang, Y.; Ge, X.; Leng, Y.; Watari, F. Hexagonal hydroxyapatite formation on TiO<sub>2</sub> nanotubes under urea modulation. *CrystEngComm* **2011**, *13*, 3741–3749.
- [5] Santos, M. Bioluminescent plankton. *PawelG Photo/Shutterstock* **2017**,
- [6] Urdiales, J. Coco de Luz. *Cadena SER* **2021**,
- [7] Géry, P. Fluorine, galena : Rogerley Mine, Rogeley Quarry, Frosterley, Weardale, North Pennines, Durham Co., England, UK. *Own work* **2011**,
- [8] Technischen, D.; Eck, M. Dissertation zur Erlangung des Doktorgrades Performance enhancement of hybrid nanocrystal/polymer bulk heterojunction solar cells: aspects of device efficiency, reproducibility, and stability. 2014.
- [9] Fayyaz, A. Performance and robustness characterisation of SiC power MOSFETs Dynamic Characterisation of SiC Power MOSFETs View project. [http://eprints.nottingham.ac.uk/end\\_user\\_agreement.pdf](http://eprints.nottingham.ac.uk/end_user_agreement.pdf).
- [10] Centro, C.; Energ, I.; The, J. G.-g.; Museum, N.; Sciences, N. Técnicas luminiscentes. **2016**,
- [11] Murthy, K. V.; Virk, H. S. Luminescence phenomena: An introduction. *Defect and Diffusion Forum* **2014**, *347*, 1–34.
- [12] Schweizer, T.; Kubach, H.; Koch, T. Investigations to characterize the interactions of light radiation, engine operating media and fluorescence tracers for the use of qualitative light-induced fluorescence in engine systems. *Automotive and Engine Technology* **2021**, *6*, 275–287.

- [13] Cookson, M. D.; Stirk, P. M. *Luminescence Spectroscopy of Minerals and Materials*; 2019.
- [14] Mckeever, S. W.; Chen, R. Luminescence models. *Radiation Measurements* **1997**, *27*, 625–661.
- [15] Iv, G. *Springer Series in Materials Science*; 2005; Vol. 21; pp 401–437.
- [16] Gaft, M.; Reisfeld, R.; Panczer, G. *Luminescence Spectroscopy of Minerals and Materials*. 2005.
- [17] Stanjek, H. *Basics of X-ray Diffraction*. **2004**, 107–119.
- [18] Bunaciu, A. A.; gabriela Udriștioiu, E.; Aboul-Enein, H. Y. X-Ray Diffraction: Instrumentation and Applications. *Critical Reviews in Analytical Chemistry* **2015**, *45*, 289–299.
- [19] Ciobanu, C. S.; Iconaru, S. L.; Massuyeau, F.; Constantin, L. V.; Costescu, A.; Predoi, D. Synthesis, structure, and luminescent properties of europium-doped hydroxyapatite nanocrystalline powders. *Journal of Nanomaterials* **2012**, *2012*.
- [20] Micheli, D.; Pastore, R.; Vricella, A.; Delfini, A.; Marchetti, M.; Santoni, F. *Spectroscopic methods for nanomaterials characterization*; Elsevier, 2017; pp 195–236.
- [21] Zhang, R.; Ulery, B. D. Synthetic vaccine characterization and design. *Journal of Bionanoscience* **2018**, *12*, 1–11.
- [22] Ali, A. S. Application of nanomaterials in environmental improvement. *Nanotechnology and the Environment* **2020**,
- [23] Ismail, K.; Ismail, K. Fabrication and characterisation of SERS substrates through photo-deposition of Gold Nanoparticles. *no. November* **2015**, 0–36.
- [24] Xuan, T. C.; Trung, N. N.; Pham, V. H. Comparative characterization of microstructure and luminescence of europium doped hydroxyapatite nanoparticles via coprecipitation and hydrothermal method. *Optik* **2015**, *126*, 5019–5021.
- [25] Murugan, R.; Ramakrishna, S. Crystallographic study of hydroxyapatite bioceramics derived from various sources. *Crystal Growth and Design* **2005**, *5*, 111–112.
- [26] Báez-Rodríguez, A.; Zamora-Peredo, L.; García-González, L.; Hernández-Torres, J.; García-Hipólito, M.; Guzmán-Mendoza, J.; Falcony, C. Luminescent Materials: Natural and Synthetic Materiales Luminiscentes: Naturales Y Sintéticos. *Ciencia y Nanociencia* | **2019**, *2*, 21–30.
- [27] Vaitkus, A.; Merkys, A.; Gražulis, S. Validation of the Crystallography Open Database using the Crystallographic Information Framework. *Journal of Applied Crystallography* **2021**, *54*, 661–672.
- [28] Quirós, M.; Gražulis, S.; Girdzijauskaitė, S.; Merkys, A.; Vaitkus, A. Using SMILES strings for the description of chemical connectivity in the Crystallography Open Database. *Journal of Cheminformatics* **2018**, *10*.

- [29] Merkys, A.; Vaitkus, A.; Butkus, J.; Okulič-Kazarinas, M.; Kairys, V.; Gražulis, S. *COD::CIF::Parser*: an error-correcting CIF parser for the Perl language. *Journal of Applied Crystallography* **2016**, *49*.
- [30] Gražulis, S.; Merkys, A.; Vaitkus, A.; Okulič-Kazarinas, M. Computing stoichiometric molecular composition from crystal structures. *Journal of Applied Crystallography* **2015**, *48*, 85–91.
- [31] Gražulis, S.; Daškevič, A.; Merkys, A.; Chateigner, D.; Lutterotti, L.; Quirós, M.; Serebryanaya, N. R.; Moeck, P.; Downs, R. T.; Le Bail, A. Crystallography Open Database (COD): an open-access collection of crystal structures and platform for world-wide collaboration. *Nucleic Acids Research* **2012**, *40*, D420–D427.
- [32] Gražulis, S.; Chateigner, D.; Downs, R. T.; Yokochi, A. F. T.; Quirós, M.; Lutterotti, L.; Manakova, E.; Butkus, J.; Moeck, P.; Le Bail, A. Crystallography Open Database – an open-access collection of crystal structures. *Journal of Applied Crystallography* **2009**, *42*, 726–729.
- [33] Downs, R. T.; Hall-Wallace, M. The American Mineralogist Crystal Structure Database. *American Mineralogist* **2003**, *88*, 247–250.
- [34] Le Bail, A. Inorganic structure prediction with *GRINSP*. *Journal of Applied Crystallography* **2005**, *38*, 389–395.
- [35] Kantharia, N.; Naik, S.; Apte, S.; Kheur, M.; Kheur, S.; Kale, B. Nano-hydroxyapatite and its contemporary applications. *Journal of Dental Research and Scientific Development* **2014**, *1*, 15.
- [36] Prakasam, M.; Locs, J.; Salma-Ancane, K.; Loca, D.; Largeteau, A.; Berzina-Cimdina, L. Fabrication, Properties and Applications of Dense Hydroxyapatite: A Review. *Journal of Functional Biomaterials* **2015**, *6*, 1099–1140.
- [37] Giraldo-Betancur, A. L.; Espinosa-Arbelaez, D. G.; Del Real-López, A.; Millan-Malo, B. M.; Rivera-Muñoz, E. M.; Gutierrez-Cortez, E.; Pineda-Gomez, P.; Jimenez-Sandoval, S.; Rodriguez-García, M. E. Comparison of physicochemical properties of bio and commercial hydroxyapatite. *Current Applied Physics* **2013**, *13*, 1383–1390.
- [38] Syamchand, S. S.; Sony, G. Multifunctional hydroxyapatite nanoparticles for drug delivery and multimodal molecular imaging. *Microchimica Acta* **2015**, *182*, 1567–1589.
- [39] Escudero, A.; Calvo, M. E.; Rivera-Fernández, S.; De La Fuente, J. M.; Ocaña, M. Microwave-assisted synthesis of biocompatible europium-doped calcium hydroxyapatite and fluoroapatite luminescent nanospindles functionalized with poly(acrylic acid). *Langmuir* **2013**, *29*, 1985–1994.
- [40] Popa, C. L.; Ciobanu, C. S.; Iconaru, S. L.; Stan, M.; Dinischiotu, A.; Negrila, C. C.; Motelica-Heino, M.; Guegan, R.; Predoi, D. Systematic investigation and in vitro biocompatibility studies on mesoporous europium doped hydroxyapatite. *Central European Journal of Chemistry* **2014**, *12*, 1032–1046.

- [41] Iconaru, S. L.; Motelica-Heino, M.; Predoi, D. Study on europium-doped hydroxyapatite nanoparticles by fourier transform infrared spectroscopy and their antimicrobial properties. *Journal of Spectroscopy* **2013**, *1*.
- [42] Han, Y.; Wang, X.; Li, S. Biocompatible Europium Doped Hydroxyapatite Nanoparticles as a Biological Fluorescent Probe. *Current Nanoscience* **2010**, *6*, 178–183.
- [43] Yang, P.; Quan, Z.; Li, C.; Kang, X.; Lian, H.; Lin, J. Bioactive, luminescent and mesoporous europium-doped hydroxyapatite as a drug carrier. *Biomaterials* **2008**, *29*, 4341–4347.
- [44] Kim, B.; Rutka, J.; Chan, W. Nanomedicine. *The New England Journal of Medicine* **2010**,
- [45] Zhang, C.; Yan, L.; Wang, X.; Zhu, S.; Chen, C.; Gu, Z.; Zhao, Y. Progress, challenges, and future of nanomedicine. 2020.
- [46] Son, J.; Yi, G.; Yoo, J.; Park, C.; Koo, H.; Choi, H. Light-Responsive Nanomedicine for Biophotonic Imaging and Targeted Therapy. *Adv Drug Deliv Rev.* 2019 January 01; *138*: 133-147. doi:10.1016/j.addr.2018.10.002.
- [47] Chetty, A.; Wepener, I.; Marei, M. K.; Kamary, Y. E.; Moussa, R. M. H Hydroxyapatite : S Ynthesis ,. *Polymers and Composites, Materials Science and Manufacturing* **2018**, 1–57.
- [48] Hing, K. A.; Best, S. M.; Bonfield, W. Characterization of porous hydroxyapatite. *Journal of Materials Science: Materials in Medicine* **1999**, *10*, 135–145.
- [49] Aubouy, L.; Paz, A. Investigación Química Europio : Naturaleza , luminiscencia y aplicaciones. *Investigación Química* **2006**, *102*, 40–45.
- [50] Vicentini, G.; Zinner, L. B.; Zukerman-Schpector, J.; Zinner, K. Luminescence and structure of europium compounds. *Coordination Chemistry Reviews* **2000**, *196*, 353–382.
- [51] Bünzli, J. C. Europium in the limelight. 2010.
- [52] Sharma, G.; Kumar, A.; Sharma, S.; Naushad, M.; Dwivedi, R. P.; ALothman, Z. A.; Mola, G. T. Novel development of nanoparticles to bimetallic nanoparticles and their composites: A review. 2019.
- [53] Villora, J. M.; Callejas, P.; Barba, M. F. Métodos de síntesis y comportamiento térmico del Hidroxiapatito. *Boletín de la Sociedad Española de Cerámica y Vidrio* **2002**, *41*, 443–450.
- [54] Drioli, E.; Giorno, L. *Comprehensive membrane science and engineering*; Newnes, 2010; Vol. 1.
- [55] Cargnello, M.; Johnston-Peck, A. C.; Diroll, B. T.; Wong, E.; Datta, B.; Damodhar, D.; Doan-Nguyen, V. V.; Herzing, A. A.; Kagan, C. R.; Murray, C. B. Substitutional doping in nanocrystal superlattices. *Nature* **2015**, *524*, 450–453.
- [56] Carolina, D.; Coy, L. OBTENCIÓN Y CARACTERIZACIÓN DE Obtaining and Characterization of Hydroxyapatite doped with. **2016**,

- [57] García, F.; Olivares, A.; Fuentes, I. Instituto Nacional de Astrofísica Óptica y Electrónica REPORTE TÉCNICO “ Conceptos y bibliografía sobre la fotoluminiscencia y procesos similares ” Realizado por :. *Scielo* **2004**, 2, 10–17.
- [58] Haddock, S. H. D.; Moline, M. A.; Case, J. F. Bioluminescence in the Sea. 2009; <http://www.annualreviews.org>.
- [59] Sánchez, M. T. M.; Sánchez, M. M. " Luz fría": trabajos experimentales sencillos. *Anales de Química de la RSEQ* **2001**, 37–42.
- [60] Valeur, B.; Berberan-Santos, M. N. A brief history of fluorescence and phosphorescence before the emergence of quantum theory. *Journal of Chemical Education* **2011**, 88, 731–738.
- [61] Hagemann, H.-R.; Afshani, J. *Handbook on the Physics and Chemistry of Rare Earths*; Elsevier, 2021; Vol. 60; pp 163–225.
- [62] Gu, L.; Shi, H.; Gu, M.; Ling, K.; Ma, H.; Cai, S.; Song, L.; Ma, C.; Li, H.; Xing, G. Dynamic ultralong organic phosphorescence by photoactivation. *Angewandte Chemie International Edition* **2018**, 57, 8425–8431.
- [63] Fuster López, L.; Stols-Witlox, M.; Picollo, M. *UV-Vis Luminescence imaging techniques/Técnicas de imagen de luminiscencia UV-Vis*; Editorial Universitat Politècnica de València, 2020; Vol. 1.
- [64] Kara, H.; Anlar, O.; Ağargün, M. *Paper Knowledge . Toward a Media History of Documents*; 2014; Vol. 7; pp 107–15.
- [65] Giovanni, Q. Propiedades luminiscentes de nanofósforos preparados por métodos hidrotermales. Ph.D. thesis, 2013.
- [66] Villabona, E. Propiedades Luminiscentes de Nanofósforos preparados por Métodos Hidrotermales. *Tesis para obtener el grado de Maestría en Ciencias Aplicadas, Universidad Autónoma de San Luis Potosí* **2013**,
- [67] Gonzalez, G.; Costa-Vera, C.; Borrero, L. J.; Soto, D.; Lozada, L.; Chango, J. I.; Diaz, J. C.; Lascano, L. Effect of carbonates on hydroxyapatite self-activated photoluminescence response. *Journal of Luminescence* **2018**, 195, 385–395.
- [68] Machado, T. R.; Sczancoski, J. C.; Beltrán-Mir, H.; Li, M. S.; Andrés, J.; Cordoncillo, E.; Leite, E.; Longo, E. Structural properties and self-activated photoluminescence emissions in hydroxyapatite with distinct particle shapes. *Ceramics International* **2018**, 44, 236–245.
- [69] Zhang, C.; Yang, J.; Quan, Z.; Yang, P.; Li, C.; Hou, Z.; Lin, J. Hydroxyapatite nano- and microcrystals with multiform morphologies: Controllable synthesis and luminescence properties. *Crystal Growth and Design* **2009**, 9, 2725–2733.

- [70] Bystrova, A. V.; Dekhtyar, Y. D.; Popov, A. I.; Coutinho, J.; Bystrov, V. S. Modified hydroxyapatite structure and properties: Modeling and synchrotron data analysis of modified hydroxyapatite structure. *Ferroelectrics* **2015**, *475*, 135–147.
- [71] Skoog, D. A.; Holler, F. J.; Nieman, T. A. *Principios de análisis instrumental*. **2008**,
- [72] Andronescu, E.; Predoi, D.; Neacsu, I. A.; Padurar, A. V.; Musuc, A. M.; Trusca, R.; Oprea, O.; Tanasa, E.; Vasile, O. R.; Nicoara, A. I.; Surdu, A. V.; Iordache, F.; Birca, A. C.; Iconaru, S. L.; Vasile, B. S. Photoluminescent hydroxyapatite: Eu<sup>3+</sup> doping effect on biological behaviour. *Nanomaterials* **2019**, *9*.
- [73] Gómez, M. A.; Padilla, G. P. Caracterización térmica de la fluorescencia del material EuTTA. 2005.
- [74] García, A. Determinación de rendimientos cuánticos de fluorescencia por métodos indirectos. 2015.
- [75] Perez, A. O.; Tapia, I. F. Conceptos y bibliografía sobre la fotoluminiscencia y procesos similares. **2004**,
- [76] Constantin, L. V.; Iconaru, S.; Ciobanu, C. S. Europium doped hydroxyapatite for applications in environmental field. *Romanian Reports in Physics* **2012**, *64*, 788–794.
- [77] Ramachandran, V.S.; Beaudoin, J. J. *Handbook of Analytical Techniques in Concrete Science and Technology*; 2001.
- [78] Faix, O. Fourier transform infrared spectroscopy. *Methods in lignin chemistry* **1992**, 83–109.
- [79] Dutta, A. *Spectroscopic Methods for Nanomaterials Characterization*; Elsevier Inc., 2017; Vol. 2; pp 73–93.
- [80] Jaggi, N.; Vij, D. R. Chapter 9 Fourier Transform Infrared. *Handbook of Applied Solid State Spectroscopy* **2006**, 411–450.
- [81] Umbría, A. Microscopía electrónica de barrido (M.E.B) Espectroscopía de difracción de rayos X (E.D.X). 1999.
- [82] Zhou, W.; Apkarian, R.; Wang, Z. L.; Joy, D. Fundamentals of scanning electron microscopy (SEM). *Scanning Microscopy for Nanotechnology: Techniques and Applications* **2007**, 1–40.
- [83] Ipohorski, M.; Bozzano, P. Microscopía electrónica de barrido en la caracterización de materiales. *Ciencia e investigación* **2013**, *63*, 43–53.
- [84] Nakamoto, K.; Brown, C. W. *Introductory Raman Spectroscopy*; 1994; pp 406–421.
- [85] Smith, E.; Dent, G. *Modern Raman Spectroscopy: A Practical Approach*; 2019; pp 1–241.
- [86] Iconaru, S. L.; Predoi, D.; Frumosu, F. Europium concentration effect of europium doped hydroxyapatite on proliferation of osteoblast cells. 2011; <https://www.researchgate.net/publication/231589933>.

- [87] Paterlini, V.; Bettinelli, M.; Rizzi, R.; Khouri, A. E.; Rossi, M.; Ventura, G. D.; Capitelli, F. Characterization and luminescence of Eu<sup>3+</sup>- and Gd<sup>3+</sup>-doped hydroxyapatite Ca<sub>10</sub>(PO<sub>4</sub>)<sub>6</sub>(OH)<sub>2</sub>. *Crystals* **2020**, *10*, 1–16.
- [88] Gómez-Morales, J.; Verdugo-Escamilla, C.; Fernández-Penas, R.; Parra-Milla, C. M.; Drouet, C.; Maube-Bosc, F.; Oltolina, F.; Prat, M.; Fernández-Sánchez, J. F. Luminescent biomimetic citrate-coated europium-doped carbonated apatite nanoparticles for use in bioimaging: Physico-chemistry and cytocompatibility. *RSC Advances* **2018**, *8*, 2385–2397.
- [89] Villani, A.; Millán, A.; González, G. Physico-Chemical and ceramic characterization of hydroxyapatite obtained by different synthesis methods (Part I). 2012.
- [90] Elisa, M.; Sava, B. A.; Vasiliu, I. C.; Monteiro, R. C.; Veiga, J. P.; Ghervase, L.; Feraru, I.; Iordanescu, R. Optical and structural characterization of samarium and europium-doped phosphate glasses. *Journal of Non-Crystalline Solids* **2013**, *369*, 55–60.
- [91] Martins, M.; García, R.; Derenzo, S.; Giulietti, M.; Rodríguez, C. Técnicas de obtención de Hidroxiapatita y otros fosfatos de calcio. 2008.
- [92] Markovic, M.; Fowler, B.; Tung, M. Preparation and characterization of a comprehensive hydroxyapatite reference standard. *J Res Natl Inst Stand Technol* **2004**, *109*, 553–568.
- [93] Ishimaru, Y.; Oshima, Y.; Imai, Y.; Iimura, T.; Takanezawa, S.; Hino, K.; Miura, H. Raman spectroscopic analysis to detect reduced bone quality after sciatic neurectomy in mice. *Molecules* **2018**, *23*.
- [94] Thang, C. X.; Pham, V. H. Luminescence variations in europium-doped silicon-substituted hydroxyapatite nanobiophosphor via three different methods. *Materials Science and Engineering B: Solid-State Materials for Advanced Technology* **2015**, *197*, 18–24.
- [95] Raii, M. Formulation, characterization and implementation of Permeable Reactive Barrier (PRB) made of calcium phosphate. <https://tel.archives-ouvertes.fr/tel-00842771>.
- [96] Elisa, M.; Iordache, S.-M.; Iordache, A.-M.; Vasiliu, I.; Grigorescu, C.; Sava, B.; Boroica, L.; Filip, A.; Dinca, M.; Bartha, C. Peculiarities of the structural and optical properties of rare-earth-doped phosphate glasses for temperature sensing applications. *Journal of Non-Crystalline Solids* **2021**, *556*, 120569.
- [97] Wicaksana, A. Pengertian Use Case Diagram. *Fungsi, Manfaat Dari Use Case Diagram*. URL: [https://medium.com/\[Tanggal Akses 27 Juni 2019\]](https://medium.com/[Tanggal Akses 27 Juni 2019]) **2016**,
- [98] Van, H. N.; Tam, P. D.; Kien, N. D. T.; Huy, P. T.; Pham, V. H. Enhancing the luminescence of Eu<sup>3+</sup>/Eu<sup>2+</sup> ion-doped hydroxyapatite by fluoridation and thermal annealing. *Luminescence* **2017**, *32*, 817–823.
- [99] Binnemans, K. Interpretation of europium ( III ) spectra. **2015**, *45*, 1–45.

- [100] Krishnapriya, T. K.; Deepti, A.; Chakrapani, P. S.; Asha, A. S.; Jayaraj, M. K. Eggshell Derived Europium Doped Hydroxyapatite Nanoparticles for Cell Imaging Application. *Journal of Fluorescence* **2021**, *31*, 1927–1936.
- [101] Yang, C.; Yang, P.; Wang, W.; Gai, S.; Wang, J.; Zhang, M.; Lin, J. Synthesis and characterization of Eu-doped hydroxyapatite through a microwave assisted microemulsion process. *Solid State Sciences* **2009**, *11*, 1923–1928.